

Universidade Federal do Rio Grande – FURG

Instituto de Oceanografia

Programa de Pós-Graduação em Oceanologia.

**ACIDIFICAÇÃO OCEÂNICA E VARIAÇÃO
INTERANUAL DE CO₂ ANTROPOGÊNICO
NO ESTREITO DE BRANSFIELD,
ANTÁRTICA**

JUAN CAMILO TORRES LASSO

Dissertação de Mestrado
apresentada como requisito
parcial para obtenção do Título
de Mestre.

Orientador: *Prof. Dr. Rodrigo Kerr Duarte Pereira*

Universidade Federal do Rio Grande (FURG), Brasil.

Rio Grande, RS, Brasil

Outubro de 2019

ACIDIFICAÇÃO OCEÂNICA E VARIAÇÃO INTERANUAL DE CO₂ ANTROPOGÊNICO NO ESTREITO DE BRANSFIELD, ANTÁRTICA

Dissertação apresentada ao Programa de Pós-Graduação em
Oceanologia como parte dos requisitos para a obtenção do Título de
Mestre

JUAN CAMILO TORRES LASSO

Rio Grande, RS, Brasil

Outubro de 2019

© A cópia parcial e a citação de trechos desta tese são permitidas sobre a condição de que qualquer pessoa que a consulte reconheça os direitos autorais do autor. Nenhuma informação derivada direta ou indiretamente desta obra deve ser publicada sem o consentimento prévio e por escrito do autor.

Torres Lasso, Juan Camilo
Acidificação oceânica e variação interanual de CO₂
antropogênico no estreito de Bransfield, Antártica. /Juan Camilo
Torres Lasso, Rio Grande: FURG, 2019.
Número de páginas p. 105
Dissertação (Mestrado) – Universidade Federal do Rio Grande.
Mestrado em Oceanologia. Área de concentração: Oceanografia
Química.
1. CO₂ antropogênico. 2. Acidificação oceânica. 3. Estreito
de Bransfield. I. Acidificação oceânica e variação
interanual de CO₂ antropogênico no estreito de Bransfield,
Antártica.

*I with my hammer pounding evermore
the rocky coast, smite Andes into dust,
strewing my bed, and, in another age,
rebuild a continent of better men.*

Ralph Waldo Emerson

Agradecimentos

Agradeço aos meus pais e irmãos pela paciência e ajuda durante este tempo que estive longe.

Agradeço a todos os integrantes do Laboratório de Estudos dos Oceanos e Clima (LEOC), especialmente aos professores Rodrigo Kerr e Mauricio Mata, pela ajuda e disposição desde o início. E, também, pela oportunidade de continuar meu crescimento de conhecimento acadêmico-científico ao possibilitar com que executasse pesquisa na Antártica. Assim, tanto pessoal como academicamente, merecem minha eterna gratidão.

Este estudo foi financiado parcialmente pela Coordenação de Aperfeiçoamento de Pessoal de Nível Superior - Brasil (CAPES), com a bolsa de estudo nº 88882.158644/2017-01 via o projeto Ciências do Mar II - nº 43/2013; sendo desenvolvido no marco do Programa Antártico Brasileiro (PROANTAR) com ajuda logística da Marinha do Brasil.

Agradecimentos especiais para meus professores de cultura brasileira, Brendon Damini e Lucas Almeida.

Índice

Agradecimentos	vi
Lista de Figuras.....	ix
Lista de Tabelas	xii
Lista de Abreviações.....	xiii
Resumo.....	xiv
Abstract.....	xv
Capítulo I: Introdução	16
Capítulo II: Objetivos.....	22
Capítulo III: Área de Estudo.....	23
3.1 Características Geológicas.....	23
3.2 Características Oceanográficas.....	24
Capítulo IV: Material e Métodos	29
4.1 Amostragem	29
4.2 Oxigênio dissolvido.....	30
4.3 Nutrientes inorgânicos dissolvidos.....	32
4.4 Análise dos Parâmetros do Sistema do Carbonato	32
4.5 Carbono Antropogênico	34
4.6 Tratamento dos dados	35
Capítulo V: Artigo Científico.....	36
5.1 Introduction.....	39
5.2 Tectonic and oceanographic features of the Bransfield Strait	42
5.3 Data and methods	46
5.3.1 Sampling strategy	46
5.3.2 Dissolved oxygen measurements	47
5.3.3 Dissolved macronutrient measurements	48
5.3.4 Carbonate system measurements.....	49
5.3.5 Anthropogenic carbon (C_{ant}) estimation.....	51
5.4 Results	52
5.4.1 Interannual variability of the water mass properties in the Bransfield Strait	53
5.4.2 Interannual changes in the seawater acidification state in the Bransfield Strait...	58
5.4.2.1 Interannual variability in the C_{ant} distribution	59
5.4.2.2 Interannual variability in pH and saturation state distribution	63
5.5 Discussion.....	67

5.5.1	Controls of the acidification state in the surface layer.....	68
5.5.2	Controls on acidification state in the intermediate and deep layers	69
5.5.3	C_{ant} in the Southern Ocean	70
5.5.4	Acidification state in the Southern Ocean.....	71
5.6	Summary and conclusions.....	72
Capítulo VI: Síntese da Discussão e Conclusões		90
Capítulo VII: Referências Bibliográficas		95

Lista de Figuras

Figura 1: Variações do CO ₂ atmosférico (linha rosa) e pH oceânico (pontos azuis) nos últimos 800.000 anos. Extraído de Pelejero et al. [2010]	17
Figura 2: Contribuições antrópicas (setas vermelhas) do CO ₂ nos diversos compartimentos da Terra, com fluxos em Gt C ano ⁻¹ . Extraído de Le Quéré et al. [2017]	18
Figura 3: Diagrama da circulação do oceano Austral e da distribuição dos fluxos associados ao carbono antropogênico (C _{ant} ; à esquerda) e CO ₂ natural (à direita). Os círculos vermelhos indicam a direção da circulação da Corrente Circumpolar Antártica e as setas indicam o comportamento do oceano como fonte ou sumidouro. Extraído de Gruber et al. [2019]	21
Figura 4: Características tectônicas do estreito de Bransfield. Extraído de Galindo-Zaldívar et al. [2004]	24
Figura 5: Rotas de advecção para o estreito de Bransfield: Água Circumpolar Profunda (linhas vermelhas); águas transicionais associadas ao mar de Bellingshausen (linhas pretas) e águas associadas ao mar de Weddell (linhas roxas). No laranja se indica o sistema da corrente de Bransfield. SACCF: frente sul da Corrente Circumpolar Antártica. SB: limite sul da Corrente Circumpolar Antártica. Extraído de Ruiz Barlett et al. [2018]	25
Figura 6: Características hidrográficas no estreito de Bransfield. As flechas indicam as direções nas quais as massas de água entram ao estreito. TBW: águas transacionais associadas ao mar de Bellingshausen; TWW: águas associadas ao mar de Weddell. Extraído de Sangrà et al. [2011]	26
Figure 7: Efeitos do SAM na região da Península Antártica. as rotas de advecção e forças das correntes durante o SAM positivo (na esquerda) e negativo (na direita) são apresentadas. Extraído de Dotto et al. [2016]	27
Figura 8: Mapa do estreito de Bransfield indicando a localização das estações por ano. Quadrados azuis: 2015; triângulos amarelos: 2016; triângulos invertidos roxas: 2017 e pontos pretos: 2018. PT: Península Trindade; JV: ilha Joinville; RG: ilha Rei George; EL: ilha Elefante.....	30
Figura 9: Dados de oxigênio dissolvido obtidos pelo CTD (esquerda) e recalculados pela equação 1 (direita).....	31
Figure 10: Map of the Bransfield Strait showing the geographical settings and the oceanographic stations that were sampled in the longitudinal (L), northern (N) and southern (S) sections between 2015 and 2018. Blue squares, yellow triangles, magenta inverted triangles and black dots show the positions of the CTD oceanographic stations during the NAUTILUS cruises for the years 2015, 2016, 2017 and 2018, respectively. The South Shetland Islands are composed of Deception Is. (DE), Livingston Is. (LIV), Greenwich Is. (GR), Robert Is. (RO), Nelson Is. (NE), King George Is. (KG), Bridgeman Is. (BI), Gibbs Is. (GI), Elephant Is. (EL) and Clarence Is. (CL), while in the tip of the Antarctic Peninsula is composed of D'Urville Is. (D'Ur), Joinville Is. (JV), Dundee Is. (DUN) and the Trinity Peninsula (TP). The bathymetry is represented by the color scale bar to the right, with the 1000 m and 2000 m isobaths highlighted by the thin gray lines. The inset map shows the location of the Bransfield Strait in the northern Antarctic Peninsula, Southern Ocean.....	47
Figure 11: θ-S depth-averaged diagrams for the CTD stations of the central (a) and eastern (b) basins of the Bransfield Strait during the NAUTILUS cruises between 2015 and 2018. The colored lines represent each specific year of sampling: blue-2015, yellow-2016, magenta-2017, and black-2018. The definitions of High Salinity Shelf Water (HSSW) and modified Circumpolar Deep Water (mCDW) followed the definitions proposed by Carmack [1974] and Robertson et al. [2002] . The gray lines mark the potential density (kg m^{-3}) isolines in reference to the density at the surface, and the dashed red lines mark the potential density selected as limits between the water layers (i.e., < 27.75 kg m^{-3} for the surface layer, between 27.75 kg m^{-3} and 27.81 kg m^{-3} for the intermediate layer, and > 27.81 kg m^{-3} for the deep layer).....	55

- Figure 12:** Vertical profiles of the potential density anomaly (in kg m^{-3}) in the Bransfield Strait across the L section in 2015 (a), 2016 (b), 2017 (c) and 2018 (d). The central basin of the Bransfield Strait is located between Deception Island (DI) and the Bridgeman Guyot (BG), while the eastern basin is located northeast of the BG (right side of the images). The black contours are the pycnoclines marked as the limits between layers (< 27.75 kg m^{-3} is considered the surface layer; between 27.75 kg m^{-3} and 27.81 kg m^{-3} is considered the intermediate layer, and > 27.81 kg m^{-3} is considered the deep layer).....55
- Figure 13:** The same as Figure 12 but for dissolved oxygen. The black contours are the concentration isolines in $\mu\text{mol kg}^{-1}$ 56
- Figure 14:** Vertical concentrations (in $\mu\text{mol kg}^{-1}$) of A_T (left) and C_T (right) in the Bransfield Strait. The symbols depict each year in which the samples were taken (squares, triangles, inverted triangles and dots for the years 2015, 2016, 2017 and 2018, respectively), while the symbols indicate the data per basin (solid symbols for the central basin and open for the eastern basin). The lines indicate the averaged concentration of all years with the standard deviations (green lines for the central basin and red lines for the eastern basin).....58
- Figure 15:** A_T - C_T salinity normalized (NA_T-NC_T) diagram, considering an averaged salinity of 34.469 for the region. Blue (red) dots denote samples above (below) 250 m.....58
- Figure 16:** Vertical profiles of C_{ant} in the Bransfield Strait across the L section in the years of 2015 (a), 2016 (b), 2017 (c) and 2018 (d). The central basin of the Bransfield Strait is located between stations L1 (north of Deception Island) and L8 (over the Bridgeman Guyot). The eastern basin of the Bransfield Strait is located between stations L8 and L11 (near Elephant Island). The white dots depict the discrete sampling depths for biogeochemical analyses. The black contours are isolines of concentration in $\mu\text{mol kg}^{-1}$61
- Figure 17:** θ -S- C_{ant} diagram for the central (a) and eastern (b) basins of the Bransfield Strait. High Salinity Shelf Water (HSSW) and modified Circumpolar Deep Water (mCDW) indices followed the definitions proposed by Carmack [1974] and Robertson *et al.* [2002]. The gray lines mark the potential density (kg m^{-3}) isolines in relation to the surface.....62
- Figure 18:** Vertical concentration (in $\mu\text{mol kg}^{-1}$) of C_{ant} in the Bransfield Strait. The symbols depict each year in which the samples were collected (squares, triangles, inverted triangles and dots for the years 2015, 2016, 2017 and 2018, respectively), while the symbols indicate the data per basin (solid symbols for the central basin and open for the eastern basin). The lines indicate the averaged concentration of all years with standard deviations (green lines for the central basin and red lines for the eastern basin).....63
- Figure 19:** Vertical profiles of pH_{total} in the Bransfield Strait across the L section in the years of 2015 (a), 2016 (b), 2017 (c) and 2018 (d) over the surface and intermediate layers (up to 750 m). The left sides of the images are oriented near Deception Island, and the right sides coincide with Elephant Island. The thin black contours represent the pH_{total} isolines; the dashed black contours represent the limits of the layers, with the surface (SL) and intermediate (IL) layers separated by the 27.75 kg m^{-3} isopycnal and intermediate and deep (DL) layers separated by the 27.81 kg m^{-3} isopycnal. The white lines indicate the saturation horizon for aragonite ($\Omega_{\text{Aragonite}} = 1$).....65
- Figure 20:** Vertical profiles of pH_{total} across the L section in the Bransfield Strait in the years of 2015 (a), 2016 (b), 2017 (c) and 2018 (d) over the deep layer (from 750 m to bottom). The central basin of the Bransfield Strait is located between Deception Island (DI) and the Bridgeman Guyot (BG), while the eastern basin is located northeast of the BG (right side of the images). The thin black contours are the pH_{total} isolines; the thick black contours are the isolines of $C_{\text{ant}} = 60 \mu\text{mol kg}^{-1}$, and the white lines are the isolines of $\Omega_{\text{Calcite}} = 1.2$65
- Figure 21:** Vertical distribution of pH_{total} in the Bransfield Strait. The symbols depict each year in which the samples were taken (squares, triangles, inverted triangles and dots for the years 2015, 2016, 2017 and 2018, respectively), while the symbols indicate the data per basin (solid symbols for the central basin and open for the eastern basin). The lines indicate the averaged concentration of all years with standard deviations (green lines for the central basin and red lines for the eastern basin).....67
- Figure 22:** Vertical distribution of Ω_{Calcite} (a) and $\Omega_{\text{Aragonite}}$ (b) in the Bransfield Strait. The symbols depict each year in which the samples were taken (squares, triangles, inverted triangles and dots

for the years 2015, 2016, 2017 and 2018, respectively), while the symbols indicate the data per basin (solid symbols for the central basin and open for the eastern basin). The lines indicate the averaged concentration of all years with standard deviations (green lines for the central basin and red lines for the eastern basin). The black lines indicate the calcium carbonate saturation horizon for each mineral phase ($\Omega = 1$).....67

Figure S1: Profiles of hydrographical properties in 2015 across the L, N and S sections in left, center and right panels, respectively. The white dots are the places where the biogeochemical data were collected. T: temperature in °C; Salinity; DO: dissolved oxygen in $\mu\text{mol kg}^{-1}$ and σ_0 : potential density anomaly in kg m^{-3} 77

Figure S2: Profiles of carbonate system properties in 2015 across the L, N and S sections in the left, center and right panels, respectively. The white dots are the places where the biogeochemical data were collected. A_T : total alkalinity in $\mu\text{mol kg}^{-1}$; C_T : total carbon in $\mu\text{mol kg}^{-1}$ C_{ant} : anthropogenic carbon in $\mu\text{mol kg}^{-1}$ 78

Figure S3: Profiles of carbonate system properties in 2015 across the L, N and S sections in the left, center and right panels, respectively. The white dots are the places where the biogeochemical data were collected. $\Omega_{\text{Aragonite}}$ and Ω_{Calcite} : calcite and aragonite saturation states (dimensionless); pH: in total scale.....79

Figure S4: Profiles of hydrographical properties in 2016 across the L, N and S sections in the left, center and right panels, respectively. The white dots are the places where the biogeochemical data were collected. T: temperature in °C; Salinity; DO: dissolved oxygen in $\mu\text{mol kg}^{-1}$ and σ_0 : potential density anomaly in kg m^{-3} 80

Figure S5: Profiles of carbonate system properties in 2016 across the L, N and S sections in the left, center and right panels, respectively. The white dots are the places where the biogeochemical data were collected. A_T : total alkalinity in $\mu\text{mol kg}^{-1}$; C_T : total carbon in $\mu\text{mol kg}^{-1}$ C_{ant} : anthropogenic carbon in $\mu\text{mol kg}^{-1}$ 81

Figure S6: Profiles of carbonate system properties in 2016 across the L, N and S sections in the left, center and right panels, respectively. The white dots are the places where the biogeochemical data were collected. $\Omega_{\text{Aragonite}}$ and Ω_{Calcite} : calcite and aragonite saturation states (dimensionless); pH: in total scale.....82

Figure S7: Profiles of hydrographical properties in 2017 across the L, N and S sections in the left, center and right panels, respectively. The white dots are the places where the biogeochemical data were collected. T: temperature in °C; Salinity; DO: dissolved oxygen in $\mu\text{mol kg}^{-1}$ and σ_0 : potential density anomaly in kg m^{-3} 83

Figure S8: Profiles of carbonate system properties in 2017 across the L, N and S sections in the left, center and right panels, respectively. The white dots are the places where the biogeochemical data were collected. A_T : total alkalinity in $\mu\text{mol kg}^{-1}$; C_T : total carbon in $\mu\text{mol kg}^{-1}$ C_{ant} : anthropogenic carbon in $\mu\text{mol kg}^{-1}$ 84

Figure S9: Profiles of carbonate system properties in 2017 across the L, N and S sections in the left, center and right panels, respectively. The white dots are the places where the biogeochemical data were collected. $\Omega_{\text{Aragonite}}$ and Ω_{Calcite} : calcite and aragonite saturation states (dimensionless); pH: in total scale.....85

Figure S10: Profiles of hydrographical properties in 2018 across the L, N and S sections in the left, center and right panels, respectively. The white dots are the places where the biogeochemical data were collected. T: temperature in °C; Salinity; DO: dissolved oxygen in $\mu\text{mol kg}^{-1}$ and σ_0 : potential density anomaly in kg m^{-3} 86

Figure S11: Profiles of carbonate system properties in 2018 across the L, N and S sections in the left, center and right panels, respectively. The white dots are the places where the biogeochemical data were collected. A_T : total alkalinity in $\mu\text{mol kg}^{-1}$; C_T : total carbon in $\mu\text{mol kg}^{-1}$ C_{ant} : anthropogenic carbon in $\mu\text{mol kg}^{-1}$ 87

Figure S12: Profiles of carbonate system properties in 2018 across the L, N and S sections in the left, center and right panels, respectively. The white dots are the places where the biogeochemical data were collected. $\Omega_{\text{Aragonite}}$ and Ω_{Calcite} : calcite and aragonite saturation states (dimensionless); pH: in total scale.....88

Lista de Tabelas

Table S1: Averages of the hydrographical properties in the Bransfield Strait separated by basins (central and eastern) and layers (surface between 0 and 250 m; intermediate between 250 and 750 m and deep above 750 m). The number of oceanographic stations occupied and discrete samples analyzed in this work were 20, 16, 26, and 19 stations and 93, 112, 114, 111 discrete samples for the years 2015, 2016, 2017 and 2018, respectively. T: temperature in °C; Salinity; DO: dissolved oxygen in $\mu\text{mol kg}^{-1}$ and σ_θ : potential density anomaly in kg m^{-3} **89**

Table S2: Averages of the carbonate system properties in the Bransfield Strait separated by basins (central and eastern) and layers (surface between 0-250 m; intermediate between 250 and 750 m and deep above 750 m). A_T : total alkalinity in $\mu\text{mol kg}^{-1}$; C_T : total carbon in $\mu\text{mol kg}^{-1}$; pH: in total scale; Ω_{Calcite} and $\Omega_{\text{Aragonite}}$: calcite and aragonite saturation states (dimensionless); C_{ant} : anthropogenic carbon in $\mu\text{mol kg}^{-1}$ **90**

Listas de Abreviações

A

A_T - Alcalinidade total (*Total alkalinity*).

C

C_{ant} - Carbono antropogênico (*Anthropogenic carbon*).

C_T - Carbono total (*Total carbon*).

CTD – Sistema Condutividade Temperatura Profundidade (*Conductivity Temperature Depth*).

E

ENSO - El Niño Oscilação do Sul (*El Niño Southern Oscillation*).

S

SAM - Modo Anular do Sul (*Southern Annular mode*).

T

TrOCA - Traçador combinando de oxigênio, carbono inorgânico e alcalinidade total (*Tracer combining Oxygen, inorganic Carbon, and total Alkalinity*).

#

Ω - Estado de saturação (*Saturation state*).

Resumo

As propriedades hidrográficas e químicas das massas de água foram analisadas no estreito de Bransfield, uma bacia semi-isolada localizada ao norte da Península Antártica, no Oceano Austral. Os dados foram obtidos pelo Grupo de Oceanografia de Altas Latitudes (GOAL) nos cruzeiros consecutivos dos verões de 2015 até 2018, como parte das atividades executadas pelo projeto NAUTILUS. Nossos objetivos foram (i) quantificar o dióxido de carbono (CO_2), associado a atividades antropogênicas (C_{ant}), nas massas de água das bacias central e leste do estreito de Bransfield, e (ii) determinar o estado de acidificação das águas da área de estudo. Baseados no método TrOCA (*Tracer combining Oxygen, inorganic Carbon, and total Alkalinity*), estimamos uma concentração média de C_{ant} de $51 \mu\text{mol kg}^{-1}$ nas duas bacias, sendo ligeiramente maior na bacia central ($53 \mu\text{mol kg}^{-1}$) que na bacia leste ($49 \mu\text{mol kg}^{-1}$). Os resultados indicaram que a ventilação recente das bacias profundas do estreito insere quantidades consideráveis de C_{ant} na região, principalmente através da advecção da Água de Plataforma de Alta Salinidade oriunda do mar de Weddell. Além disso, a profundidade média do horizonte de saturação da aragonita é ~ 200 m mais raso na bacia central que na leste. A intrusão de C_{ant} no estreito de Bransfield pode mudar rapidamente o estado de acidificação do oceano devido aos intensos processos de mistura de massas de água.

Abstract

We analyzed the hydrographic and chemical properties of the water masses in the Bransfield Strait, a semi-enclosed basin located in the Northern Antarctic Peninsula, Southern Ocean. The dataset analyzed was sampled by the Brazilian High Latitude Oceanography Group (GOAL) between four consecutive summer cruises from 2015 to 2018, as part of the activities executed by the NAUTILUS project. Our aims were (i): to quantify the carbon dioxide (CO_2) associated with anthropogenic activities (C_{ant}) in the water masses of the central and eastern basins, and (ii) to determine the ocean acidification state on the study region. Based on the *Tracer combining Oxygen, inorganic Carbon, and total Alkalinity* (TrOCA) approach, we estimated an averaged C_{ant} concentration of 51 $\mu\text{mol kg}^{-1}$ in the Bransfield Strait, which is slightly higher in the central basin (53 $\mu\text{mol kg}^{-1}$) than the eastern basin (49 $\mu\text{mol kg}^{-1}$). The results indicated that recent ventilation of the Bransfield Strait deep basins brings considerable amounts of C_{ant} , mainly through the advection of High Salinity Shelf Water coming from the Weddell Sea continental shelf. In addition, the averaged depth of aragonite saturation horizon is \sim 200 m shallower in the central than the eastern basin of the Bransfield Strait. Thus, the C_{ant} intrusion in the Bransfield Strait can rapidly change the ocean acidification state due intense water masses mixing process.

Capítulo I: Introdução

O oceano global absorve cerca de 30% das emissões antropogênicas de dióxido de carbono (CO_2) para a atmosfera e, desde que se tem registro, os níveis de emissões aumentarem de $1.7 \pm 0.1 \text{ Gt C ano}^{-1}$ na década de 1960 até $4.7 \pm 0.11 \text{ Gt C ano}^{-1}$ no período 2007-2016. Assim, foi gerado um incremento no conteúdo de CO_2 no oceano de $1.0 \pm 0.5 \text{ Gt C ano}^{-1}$ até $2.4 \pm 0.55 \text{ Gt C ano}^{-1}$ no mesmo período de tempo [[Le Quéré et al. 2017](#)]. Devido ao fato que o oceano é quimicamente sensível a entrada de CO_2 , os câmbios no conteúdo dissolvido alteram a disponibilidade do carbonato de cálcio (CaCO_3) [[Millero 2013](#)], modificando as condições ambientais e afetando o ecossistema e os organismos marinhos. O CO_2 reage com a água do mar quando absorvido, sendo dissolvido numa sequência de reações químicas que formam o ácido carbônico, os íons bicarbonato e carbonato em diferentes proporções e concentrações, que são dependentes do pH da água do mar [[Millero 2007](#),

Fassbender *et al.* 2017]. Assim, as variações no CO₂ absorvido podem diminuir (aumentar) o pH do oceano enquanto diminui (aumenta) as concentrações do íon carbonato (bicarbonato) em proporções que dependem da variação do pH (Fig. 1). Além disso, a diminuição do pH faz com que as estruturas de CaCO₃ conservadas pelo oceano, através do tempo, sejam dissolvidas e aumentem o íon bicarbonato no oceano [Pelejero *et al.* 2010, Hönisch *et al.* 2012].

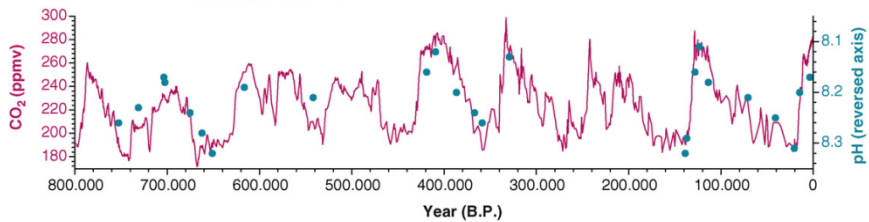


Figura 1: Variações do CO₂ atmosférico (linha rosa) e pH oceânico (pontos azuis) nos últimos 800.000 anos. Extraído de Pelejero *et al.* [2010].

No ciclo natural do carbono, a interação oceano-atmosfera tende a equilibrar as concentrações dos gases [Lee *et al.* 2003], agindo em grandes períodos de tempo e permitindo aos organismos se adaptarem às mudanças no ambiente [Pelejero *et al.* 2010]. Porém, desde a revolução industrial, o nível do CO₂ na atmosfera aumentou drasticamente devido às atividades humanas (Fig. 2), principalmente pelo consumo de carvão e petróleo, o que alterou o comportamento do ciclo do carbono num curto tempo [Le Quéré *et al.* 2018], passando de valores entre 180-260 ppmv nos últimos 800.000 anos [Pelejero *et al.* 2010, Hönisch *et al.* 2012] até ~ 414 ppmv no presente [Scripps Institution of Oceanography, 2019]. Esse excesso de CO₂ na atmosfera, que é posteriormente armazenado nas camadas dos oceanos, é chamado de carbono antropogênico (C_{ant}). O C_{ant} é definido como a diferença nas concentrações de CO₂ entre o período pré-industrial e o atual [Friis 2006], ou o máximo aumento no carbono

inorgânico dissolvido total devido à industrialização, sendo estas quantidades dependentes da pressão parcial do CO₂ e da temperatura do ambiente [Sarmiento & Gruber 2002]. Além disso, à medida que o oceano se torna mais eficiente na captura do CO₂ devido ao incremento no gradiente, este se torna mais vulnerável ao aumento de C_{ant} [Doney *et al.* 2009, Cooley *et al.* 2013].

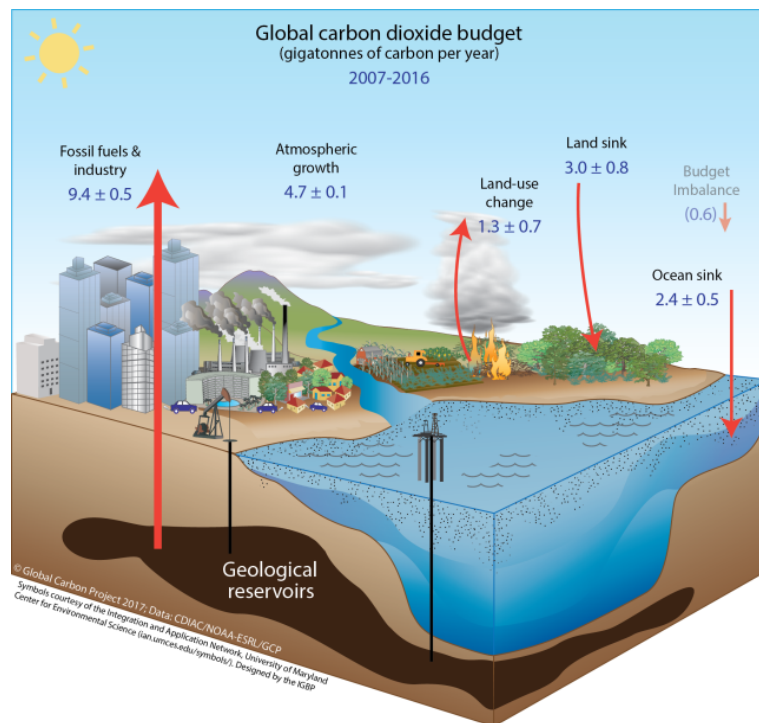


Figura 2: Contribuições antrópicas (setas vermelhas) do CO₂ nos diversos compartimentos da Terra, com fluxos em Gt C ano⁻¹. Extraído de Le Quéré *et al.* [2017].

A absorção do C_{ant} ocorre na interface atmosfera-oceano, embora o sequestro implique em processos biológicos e físicos (circulação e difusão) para as camadas profundas [Vázquez-Rodríguez *et al.* 2008, Iudicone *et al.* 2016]. A capacidade do oceano para absorver o C_{ant} depende dos parâmetros hidrográficos e biogeoquímicos regionais como temperatura do oceano, salinidade, alcalinidade total (A_T) e pressão parcial do CO₂ nas massas de águas

superficiais, pelo qual, há regiões mais propensas para absorvê-lo [Shadwick et al. 2013, Waugh 2014, Guallart et al. 2015, Lovenduski et al. 2018].

Porém, nem todo o C_{ant} absorvido pelos oceanos é capturado, devido a fugacidade do gás nas massas de água em superfície. Para a efetiva captura de C_{ant} pelos oceanos, as massas de água de superfície precisam afundar por aumento na sua densidade, quando os processos de advecção, mistura e biogeoquímicos distribuem e mantêm o C_{ant} fora do sistema climático [McNeil et al. 2001, Shadwick et al. 2013, Legge et al. 2017, Humphreys et al. 2018]. Esses processos são de grande importância nas altas latitudes, devido às condições hidrográficas quase homogêneas, e o fato das camadas superficiais e profundas terem uma alta conectividade entre elas [van Heuven et al. 2014]. A quantidade e a velocidade com que o C_{ant} está sendo absorvido nos oceanos em altas latitudes faz com que o equilíbrio no sistema carbonato mude abruptamente, dificultando aos organismos terem o tempo de adaptação necessário para as novas condições [Fabry et al. 2009].

Em regiões onde massas de água densas e frias são ventiladas (por exemplo, mares de Ross e de Weddell no hemisfério sul, e mares do Groenlândia e de Labrador no hemisfério norte), processos de convecção profunda permitem que os oceanos armazenem o C_{ant} em níveis profundos por longos períodos de tempo antes que essas massas de água retornem à superfície e interajam novamente com o volume de CO₂ atmosférico [Matear & Lenton 2008, Jones et al. 2014]. Neste processo de absorção de C_{ant}, o oceano Austral tem um papel importante devido as suas características hidrográficas, amortecendo as emissões antropogênicas para uma absorção de cerca de 1,4 Gt C ano⁻¹ desde a atmosfera e ajudando a manter uma concentração nesta de ~ 414 ppmv [Le

Quéré *et al.* 2018, 2017]. Entretanto, isto causa uma rápida mudança nos parâmetros biogeoquímicos do ambiente em que vivem os organismos marinhos calcários [Orr *et al.* 2005, Fabry *et al.* 2009]. Na plataforma continental do Mar de Weddell, estas condições ocorrem e estão associadas aos processos de formação da Água de Fundo Antártico [McNeil *et al.* 2001, van Heuven *et al.* 2014], onde pelas suas baixas temperaturas, quantidades relevantes de CO₂ são absorvidas da atmosfera [Ito & Follows 2013, Pardo *et al.* 2014, Tanhua *et al.* 2017]. Estas águas de plataforma, que contribuem com a ventilação do oceano profundo, são transportadas pelo giro ciclônico de Weddell para o leste da Península Antártica [Hellmer *et al.* 2017], sendo advectadas pela Corrente Costeira Antártica em direção norte até chegar à abertura entre a península e a ilha Joinville, entrando para o estreito de Bransfield com um tempo de residência que varia entre meses a anos [Gonçalves-Araujo *et al.* 2015, Dotto *et al.* 2016, Sangrà *et al.* 2017]. A permanência destas águas no estreito é controlada pelas características tectônicas presentes, que permite um ambiente relativamente isolado [García *et al.* 2009] que atua por limitar a mistura das águas advectadas desde o mar de Weddell com as águas da bacia oeste do estreito e/ou com águas oriundas do fluxo da Corrente Circumpolar Antártica.

Para contribuir ao conhecimento do sistema carbonato marinho nas altas latitudes e predizer os efeitos que o incremento do CO₂ ocasionará no sistema, é necessário (i) conhecer a distribuição do C_{ant} no interior do oceano (Fig. 3), (ii) compreender os processos de captura e distribuição na superfície do oceano, (iii) entender o impacto do incremento do CO₂, ou seja, como ocorrerá a troca e interação entre os processos físicos e biogeoquímicos e sua variação em cada região oceânica [Touratier & Goyet 2004a]. Com isso, é importante caracterizar

a variabilidade na química do carbonato nos oceanos polares e determinar as condições ambientais nas quais os organismos habitam [Tynan *et al.* 2016]. O estreito de Bransfield é um lugar de extrema importância para a compreensão dos efeitos gerados pelo aumento do CO₂ atmosférico e sua posterior absorção no oceano, pois se trata de um ambiente com características hidrográficas preservadas dos processos que ocorrem na plataforma oeste do mar de Weddell [Dotto *et al.* 2016, Sangrà *et al.* 2017, van Caspel *et al.* 2018]. Além disso, o tempo de advecção das águas é suficiente para atingir o equilíbrio do CO₂ entre o oceano e a atmosfera [van Heuven *et al.* 2014], permitindo estimar a quantidade de C_{ant} que está sendo absorvida anualmente e como este incremento está mudando o estado de acidificação do mar de Weddell.

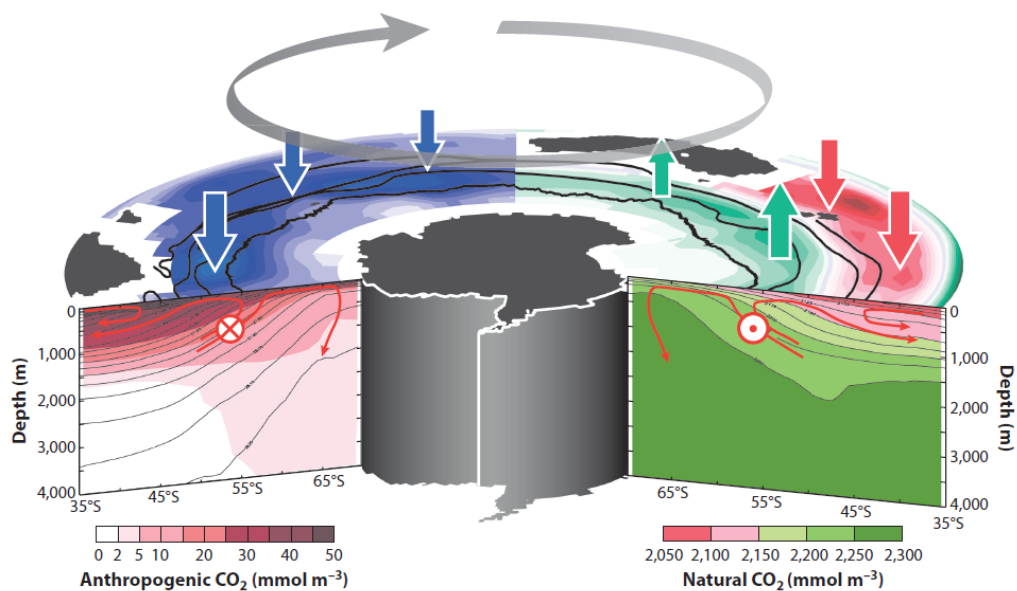


Figura 3: Diagrama da circulação do oceano Austral e da distribuição dos fluxos associados ao carbono antropogênico (C_{ant}; à esquerda) e CO₂ natural (à direita). Os círculos vermelhos indicam a direção da circulação da Corrente Circumpolar Antártica e as setas indicam o comportamento do oceano como fonte ou sumidouro. Extraído de Gruber *et al.* [2019].

Capítulo II: Objetivos

O objetivo geral deste estudo foi quantificar o C_{ant} nas águas das bacias central e leste do estreito de Bransfield e associar com as variações interanuais no seu estado de acidificação. Dois objetivos específicos foram delineados: (i) investigar o estado de acidificação das águas do estreito de Bransfield, através da verificação do estado de saturação do CaCO₃ ($\Omega_{\text{Calcita}} < 1$) e da distribuição do pH (< 7) das águas e (ii) determinar as variações interanuais da concentração de C_{ant}, de pH e dos estados de saturação do CaCO₃.

Capítulo III: Área de Estudo

3.1 Características Geológicas

O estreito de Bransfield corresponde a um conjunto de sub-bacias oceânicas de retroarco geradas por processos de extensão da crosta oceânica associada à subducção da placa Phoenix sobre a placa Antártica [Grad *et al.* 1997, Fretzdorff 2004, Funaki *et al.* 2014]. Isto gerou a separação das ilhas Shetland do Sul da Península Antártica (Fig. 4). As ilhas Shetland do Sul são formadas por onze ilhas maiores, que correspondem a parte sul do arco vulcânico de Escócia e foram geradas em pelo menos três eventos tectônicos associados à expansão do fundo oceânico e evidenciados na formação das ilhas e dos rifts submarinhos [García *et al.* 2009]. Estas ilhas são compostas por rochas vulcânicas e sedimentares associadas num intervalo de idades entre o Mesozóico e o Quaternário, com máxima atividade de formação no Terciário, junto com rochas metamórficas mais antigas desprendidas desde a placa Antártica [Anderson and Wellner, 2011, López-Martínez *et al.* 2016]. Ao mesmo

tempo que o vulcanismo diminuía, diversos processos tectônicos deformaram e alargaram o conjunto de ilhas, gerando três sub-bacias (i.e., bacias oeste, central e leste) limitadas longitudinalmente pelas ilhas Decepção e Bridgeman [Dziak *et al.* 2010], tendo na sub-bacia central uma extensão máxima e na sub-bacia leste a profundidade máxima [Galindo-Zaldívar *et al.* 2004].

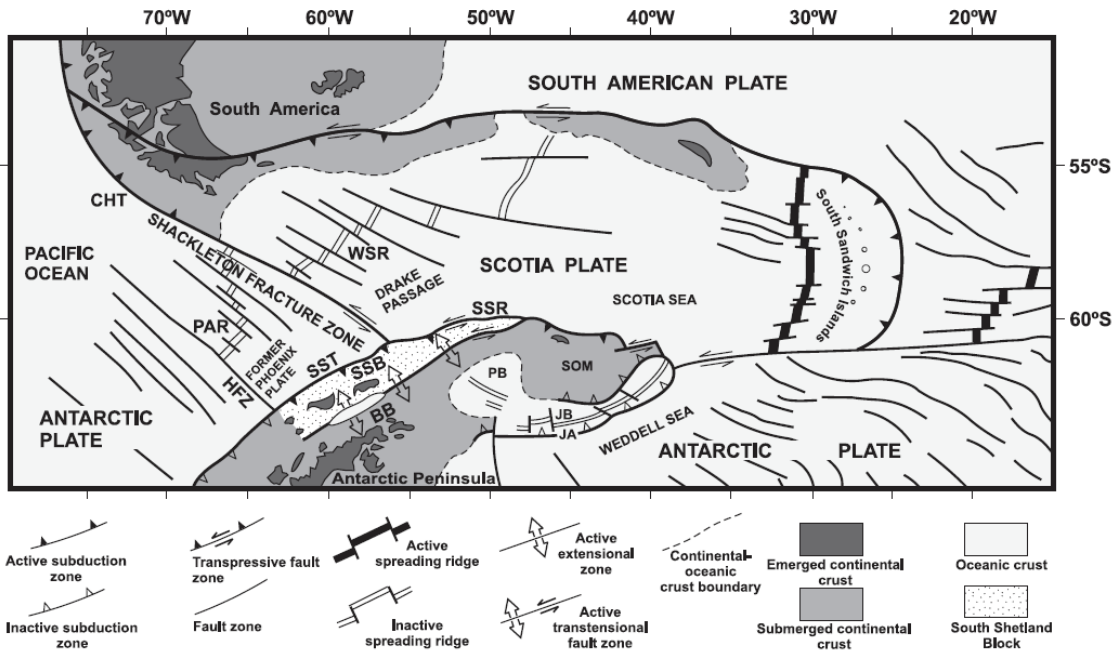


Figura 4: Características tectônicas do estreito de Bransfield. Extraído de Galindo-Zaldívar *et al.* [2004].

3.2 Características Oceanográficas

As configurações geográfica no estreito de Bransfield permitem um local quase isolado, que limita a mistura entre a Água Circumpolar Profunda Modificada, proveniente do mar de Bellingshausen, e a Água de Plataforma de Alta Salinidade, mais fria e oxigenada, proveniente do mar de Weddell [Wilson *et al.* 1999, Dotto *et al.* 2016]. Além disso, os processos dinâmicos que agem na região (Fig. 5) e as diferenças hidrográficas das massas de água que são advectadas para o estreito de Bransfield, fazem com que a camada superficial

nas bacias central e leste seja mais influenciadas pelas massas de água advectadas do mar de Bellinghaussen [Gonçalves-Araujo *et al.* 2015, Dotto *et al.* 2016]. No mar de Bellinghaussen, as fases negativas (positivas) do ENSO estão associadas a águas menos (mais) densas, devido às mudanças na quantidade da Água Circumpolar Profunda se misturando com as águas do mar de Bellinghaussen antes de entrar na bacia leste do estreito de Bransfield [Ruiz Barlett *et al.* 2018].

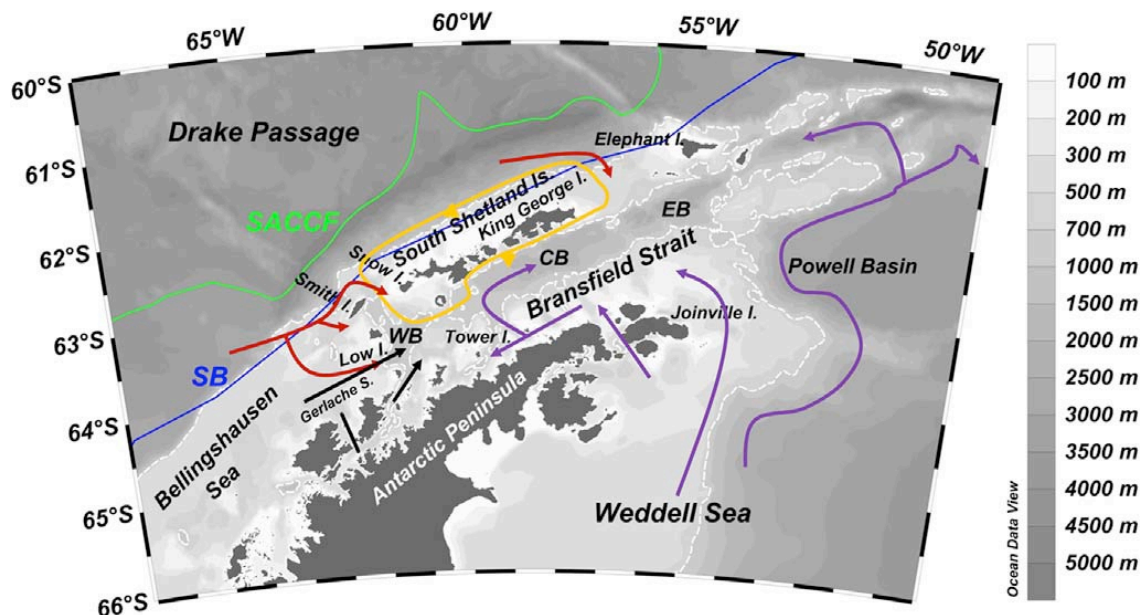


Figura 5: Rotas de advecção para o estreito de Bransfield: Água Circumpolar Profunda (linhas vermelhas); águas transicionais associadas ao mar de Bellingshausen (linhas pretas) e águas associadas ao mar de Weddell (linhas roxas). No laranja se indica o sistema da corrente de Bransfield. SACCF: frente sul da Corrente Circumpolar Antártica. SB: limite sul da Corrente Circumpolar Antártica. Extraído de Ruiz Barlett *et al.* [2018]

Esta água menos densa cruza para as bacias central e leste do estreito de Bransfield, principalmente pela plataforma das ilhas Shetland do Sul (Fig. 6), sendo limitada pela densidade nas camadas superiores [Sangrà *et al.* 2011, van Caspel *et al.* 2018], variando suas propriedades físicas e químicas facilmente pela interação com a atmosfera.

Enquanto a camada superficial das bacias central e leste do estreito de Bransfield é associada às águas do mar de Bellinghaussen, a camada profunda

é associada com as massas de água mais frias, com temperatura próxima ao ponto de congelamento da água, das plataformas continentais do Mar de Weddell. No processo de advecção das massas de água sobre a plataforma continental do mar de Weddell, estas são influenciadas por rejeição de salmoura nas plataformas de gelo [Frölicher *et al.* 2015], aumentando sua salinidade e diminuindo a temperatura pelo contato basal com gelo marinho, gerando uma água de plataforma de alta densidade [Hellmer *et al.* 2017], que é advectada desde o leste do mar de Weddell até a ponta da Península Antártica [Fahrbach *et al.* 1992, Gordon 1998, Thompson *et al.* 2009].

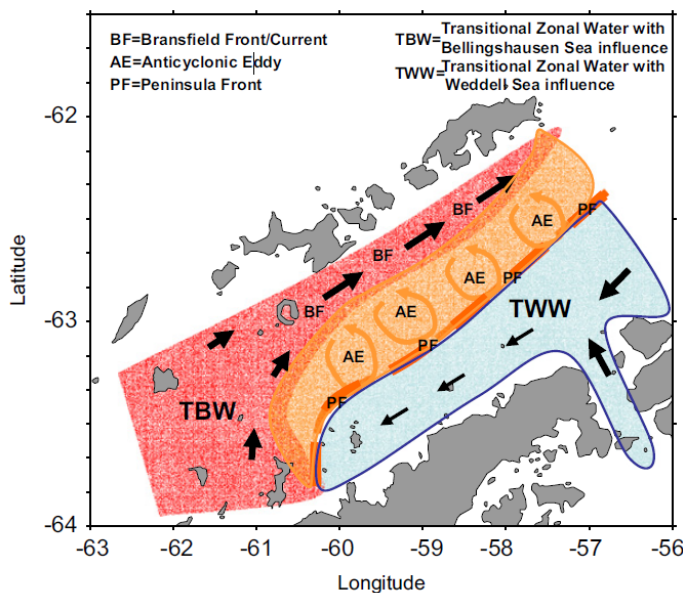


Figura 6: Características hidrográficas no estreito de Bransfield. As flechas indicam as direções nas quais as massas de água entram ao estreito. TBW: águas transicionais associadas ao mar de Bellingshausen; TWW: águas associadas ao mar de Weddell. Extraído de Sangrà *et al.* [2011].

O ingresso das massas de água provenientes do mar de Weddell para o estreito de Bransfield (Fig. 7) varia segundo o SAM [Dotto *et al.* 2016, van Caspel *et al.* 2018], influenciando as proporções de mistura e modificando a rota de adveção para as bacias central e leste [Caspel *et al.* 2018]. Para o preenchimento do fundo da bacia central, as massas de água de plataforma entram através do canal Antártico entre a Península Antártica e a ilha Joinville

[Gordon *et al.* 2000, Renner *et al.* 2009, Thompson *et al.* 2009], sendo influenciada pela água da plataforma da plataforma de gelo Larsen; enquanto a bacia leste está associada com a plataforma de gelo Filchner-Ronne [van Caspel *et al.* 2018], ingressando ao estreito pelo lado norte da ilha Joinville em sentido anti-horário até o estreito.

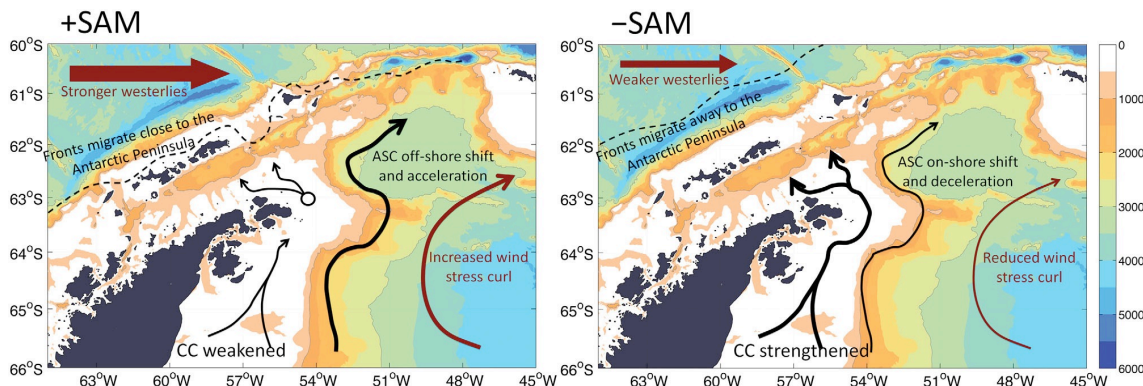


Figure 7: Efeitos do SAM na região da Península Antártica. as rotas de advecção e forças das correntes durante o SAM positivo (na esquerda) e negativo (na direita) são apresentadas. Extraído de Dotto *et al.* [2016].

As variações nas massas de água pelos modos climáticos (ENSO influenciando a camada superficial, o SAM a camada profunda e a camada intermediária altamente variável pelo modo dominante), podem variar sazonalmente segundo as condições climáticas intra-anuais e processos de mistura diferenciados que acontecem na região [Gordon *et al.* 2000, Sangrà *et al.* 2011, Ruiz Barlett *et al.* 2018]. A interação entre a fase dos modos climáticos e as variações hidrográficas causadas pelo clima irá influenciar as massas de água que são advectadas para cada bacia do estreito de Bransfield, preenchendo a bacia central com as águas recentemente ventiladas na plataforma de gelo Larsen e conservando as características hidrográficas adquiridas na plataforma do mar de Weddell; enquanto a bacia leste é influenciada pelas águas associadas à plataforma de gelo Filchner-Ronne [van

[Caspel et al. 2018](#)], se misturando com as águas mais densas da bacia central, transbordando para a bacia leste [[Gordon et al. 2000](#), [Ruiz Barlett et al. 2018](#)].

A influência do ENSO nas águas superficiais do estreito de Bransfield controla o estado de acidificação devido ao incremento na mistura da Água Circumpolar Profunda que é advectada desde a bacia oeste, que diminui a densidade pelo incremento na temperatura, modificando a solubilidade do CO₂ e incrementando sua pressão parcial [[Conrad & Lovenduski 2015](#)]. Nas camadas intermediaria e profunda, o estado de acidificação depende das propriedades adquiridas pelas massas de água durante a ventilação e da mistura com massas de água externas durante a advecção. As variações do SAM sobre o mar de Weddell modificam a turbidez na camada superficial, o qual incrementa a sua capacidade de absorção do CO₂ (C_{ant}) da atmosfera, modifica o tempo de ventilação das massas de água e modifica as rotas de advecção para a camada profunda do estreito [[Dotto et al. 2016](#)].

Capítulo IV: Material e Métodos

Esta pesquisa foi desenvolvida pelo Grupo de Oceanografia de Altas Latitudes (GOAL) no âmbito do projeto NAUTILUS como parte do Programa Antártico Brasileiro (PROANTAR), baseados nos dados hidrográficos e biogeoquímicos obtidos no Navio Polar Almirante Maximiano durante quatro verões consecutivos entre 2015 e 2018.

4.1 Amostragem

Os dados hidrográficos foram obtidos com o sistema CTD 911/Carrossel Sea-Bird de 24 garrafas Niskin de 5 L ou 12 L. Em cada ponto de amostragem (Fig. 8) foram registrados os dados hidrográficos com o CTD, o qual conta com dois sensores de temperatura, condutividade e oxigênio dissolvido, permitindo uma precisão para a temperatura de $\pm 0,002^{\circ}\text{C}$, e de $\pm 0,003$ para a salinidade. Além dos dados hidrográficos, foram tomadas, em média, quatro amostras de água do mar por estação para as medições de oxigênio dissolvido, alcalinidade

total (A_T), carbono inorgânico dissolvido total (C_T), nutrientes inorgânicos dissolvidos e pH, variando seu número conforme a profundidade. No total, para este trabalho foram analisadas: 20, 16, 26 e 19 estações; e 93, 112, 114, 111 amostras de água do mar, respectivamente para os anos de 2015, 2016, 2017 e 2018.

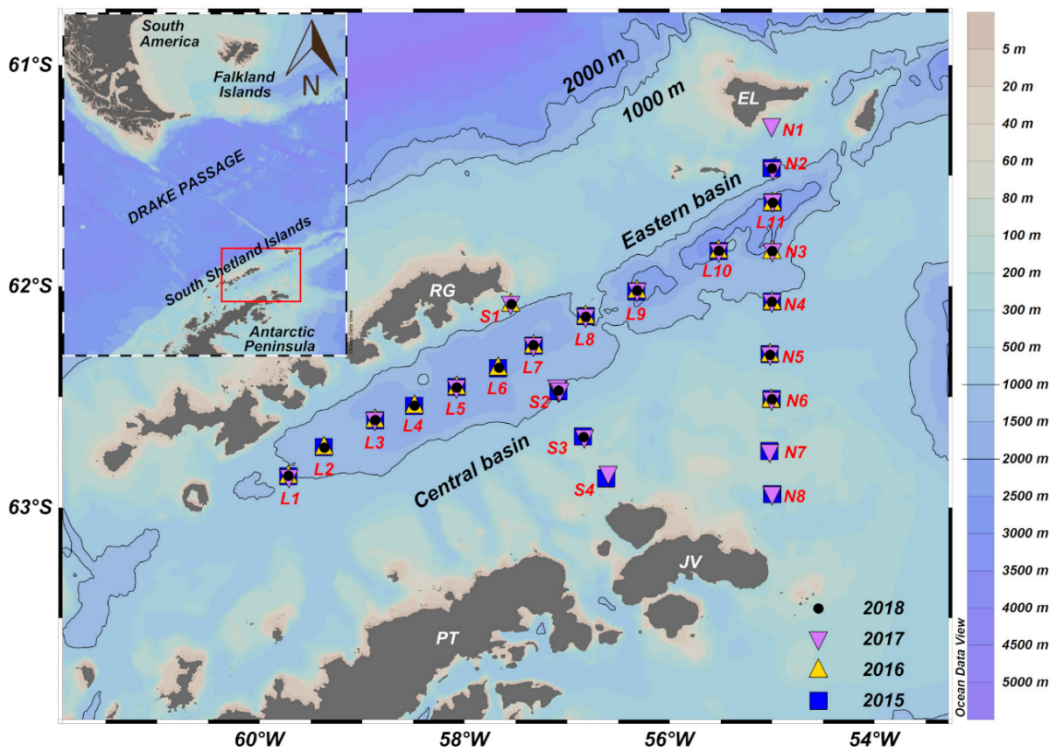


Figura 8: Mapa do estreito de Bransfield indicando a localização das estações por ano. Quadrados azuis: 2015; triângulos amarelos: 2016; triângulos invertidos roxos: 2017 e pontos pretos: 2018. PT: Península Trindade; JV: ilha Joinville; RG: ilha Rei George; EL: ilha Elefante.

4.2 Oxigênio dissolvido

As primeiras amostras tomadas ao retornar para o navio o Carrossel foram as de oxigênio dissolvido, que foram analisadas através do método químico de Winkler para calibrar os sensores do CTD, apresentando boas correlações nos anos 2015 ($0,7315 * \text{oxigênio (CTD)} + 0,2142$, com o coeficiente de determinação $r^2 = 0,99$) e 2016 ($0,9608 * \text{oxigênio (CTD)} - 0,7295$, com $r^2 = 0,94$). Para os anos de 2017 e 2018, tanto o congelamento dos sensores quanto

valores incoerentes dos dados químicos obtidos pela análise de Winkler impediram a calibração dos sensores. Para obter dados de oxigênio dissolvido nestes anos, foi desenvolvida uma equação polinomial baseada nos dados calibrados pelo método Winkler. Para isso foi estimado o valor médio da curva Winkler obtida na estação L5 em 2015-2016 e com este valor como fator dependente, e com a temperatura e a salinidade média da mesma estação como fatores independentes, foi desenvolvida a equação 1 para determinar os valores de oxigênio nos quatro anos. O erro padrão da equação 1 é de $\pm 0,07 \text{ mL L}^{-1}$ ou $\pm 3,0 \mu\text{mol kg}^{-1}$.

$$\text{OD} = 226,0885 + (T^* - 1,18919) + (S^* - 6,40931) + 0,073454 \quad (1)$$

Devido a alta variância nos dados de oxigênio dissolvido, temperatura e salinidade da camada superficial, não foi possível inserir estes dados no cálculo da equação 1, considerando somente os valores abaixo de 250 m. Como o método de estimação do carbono antropogênico não permite a determinação da concentração em superfície, as variações no oxigênio dissolvido nesta camada não afetam nossos resultados (Fig. 9).

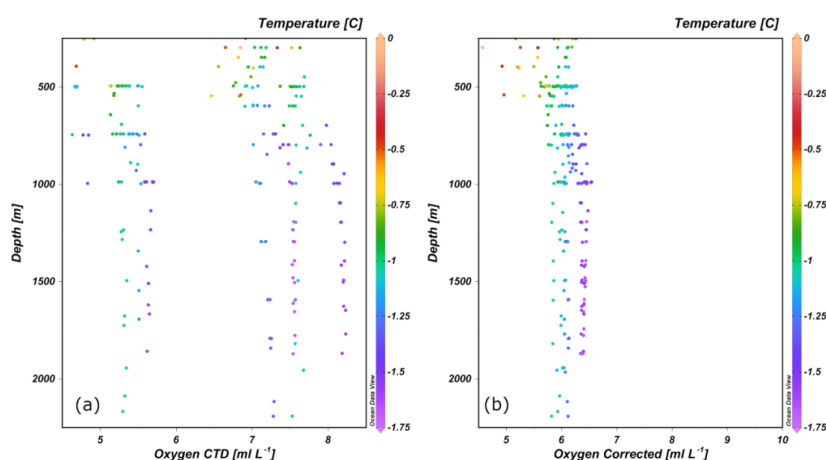


Figura 9: Dados de oxigênio dissolvido obtidos pelo CTD (esquerda) e recalculados pela equação 1 (direita) sob os 250 m.

4.3 Nutrientes inorgânicos dissolvidos

A análise dos nutrientes inorgânicos dissolvidos (amônia, nitrato, nitrito, fosfato e silicato) tem o objetivo de melhorar a precisão no cálculo dos parâmetros do sistema carbonato no software CO2Sys v1.1 [[Lewis & Wallace 1998](#)], e estimar a razão de Redfield na região [[Redfield et al. 1963](#)]. As amostras foram coletadas em frascos plásticos de 60 mL e imediatamente congeladas até serem analisadas num Fluorímetro Trilogy para amônia, e com um Módulo Analisador FIAstar™ 5000 pelo método de colorimetria por injeção em fluxo para nitrato, nitrito, fosfato e silicato na Unidade Multiusuários de Análise Ambiental (UMAA) da Universidade Federal do Rio de Janeiro (UFRJ), no Rio de Janeiro, Brasil. Os limites de detecção (quantificação) foram 0,05 (0,15), 0,11 (0,33), 0,02 (0,06), 0,10 (0,30) e 0,50 (1,50) µM para amônia, nitrato, nitrito, fosfato e silicato, respectivamente.

4.4 Análise dos Parâmetros do Sistema do Carbonato

Após a coleta para análise de oxigênio dissolvido, foram tomadas as amostras de pH e analisadas a bordo com um pHmetro potenciométrico Metrohm® 827 antes de duas horas de amostragem. Soluções-padrão Fluka® Sigma-Aldrich® com valores de pH iguais a 4.008 (hidrogenoftalato de potássio + cloreto de fenilmercúrio) e 7.413 (hidrogenofosfato dissódico + di-hidrogenofosfato de potássio) foram utilizados para calibrar o eletrodo de pH, corrigindo também os valores para a temperatura *in situ* segundo [Gieskes \[1969\]](#), tendo uma incerteza no pH de 0,05 unidades de pH na escala NBS (National Bureau Standards). No navio prioriza-se as coletas para análises de oxigênio dissolvido e pH, devido a rápida mudança nesses parâmetros, sendo posteriormente executada a coleta de água para medição de A_T e C_T.

As amostras para medições de A_T e C_T foram coletadas em frascos pré-lavados de 250 mL ou 500 mL e dependendo do intervalo de tempo desde a coleta da amostra até sua análise, estas podem ter sido fixadas com uma solução supersaturada de cloreto de mercúrio ($HgCl_2$), para limitar a atividade biológica que pode mudar as propriedades da água analisada. Para o análise, foi aplicado o procedimento descrito no [DOE \[1994\]](#), que é baseado na titulação potenciométrica em célula fechada, sob condições de temperatura controlada de $25 \pm 0,1$ °C por um banho termostático Tamson® TLC 15. Para a análise foi usado um titulador automatizado Methrom® Titrando 808 (5 mL) com um eletrodo de vidro combinado (Methrom® 6.0262.100) para os anos de 2015 e 2017 e um ABU901 Autoburette (5 mL) da Radiometer Analytical® conectado com um medidor de pH ProLab 3000 da Schott Instruments® acoplado a um eletrodo de vidro BlueLine 18 pH da SI Analytics® para os anos 2016 e 2018. Durante as medições foram feitas análises de controle de qualidade com material de referência certificado dos lotes 96 (2015), 149 (2016 e 2017) e 162 (2018), de acordo com [Dickson et al. \[2003\]](#). Os protocolos seguidos nas análises permitiram determinar uma acurácia de $\pm 3,0$; $\pm 3,4$; $\pm 2,8$; e $\pm 5,7$ $\mu\text{mol kg}^{-1}$ para A_T nos anos de 2015, 2016, 2017 e 2018, respectivamente.

Baseado nas propriedades do sistema carbonato, os dados de pH_{NBS} foram recalculados no software CO2Sys v1.1 [[Lewis & Wallace 1998](#)] usando as constantes do ácido carbônico de [Goyet & Poisson \[1989\]](#), sulfato de [Dickson \[1990\]](#) e borato de [Uppström \[1974\]](#) para pH_{total} , tendo como dados de entrada A_T , pH_{NBS} , e as concentrações dos nutrientes inorgânicos dissolvidos fosfato e silicato. Com isto o erro provável estimado foi reduzido para ± 0.03 unidades de pH_{total} . Além disso, devido a alguns valores superestimados nos dados de C_T ,

esses foram também recalculados com as mesmas constantes e os dados de entrada de A_T , pH_{total} e as concentrações de fosfato e silicato, obtendo erros prováveis estimados de ± 5.0 ; ± 4.4 ; ± 2.9 ; e $\pm 3.4 \mu\text{mol kg}^{-1}$ para os anos 2015, 2016, 2017 e 2018, respectivamente [e.g., [Carvalho-Borges et al. 2018](#)]. Com os dados de entrada de A_T e C_T foram calculados no CO2Sys os estados de saturação (Ω) de calcita e aragonita, com erros prováveis estimados de $\pm 0,06$, $\pm 0,08$, $\pm 0,06$ e $\pm 0,08$ para Ω_{Calcita} e de $\pm 0,04$, $\pm 0,05$, $\pm 0,04$ e $\pm 0,05$ para $\Omega_{\text{Aragonita}}$ nos anos de 2015, 2016, 2017 e 2018 respectivamente.

4.5 Carbono Antropogênico

Como o CO_2 antropogênico não pode ser medido diretamente, o TrOCA (*Tracer combining Oxygen, inorganic Carbon, and total Alkalinity*) [[Touratier & Goyet 2004b](#), [Touratier et al. 2007](#)] foi o método de determinação do teor de CO_2 antropogênico (C_{ant}) aplicado neste estudo [e.g., [Touratier et al. 2007](#), [Goyet et al. 2009](#), [Kerr et al. 2017a](#), [Orselli et al. 2018](#)]. A concentração de C_{ant} foi determinada através da equação 2, a partir dos dados hidrográficos, A_T e C_T :

$$C_{\text{ant}} = \frac{D0 + 1.279(C_T - 0.5A_T) - e^{[7.511 - (1.087 \times 10^{-2})\theta - \left(\frac{7.81 \times 10^5}{A_T^2}\right)]}}{1.279} \quad (2)$$

porém, o método precisa assumir condições de estado estacionário nas características hidrográficas e biogeoquímicas na região a ser investigada [[van Heuven et al. 2014](#)], por isso este não pode ser aplicado na camada de mistura superficial, onde as trocas de gases na interface atmosfera-oceano e os processos biológicos envolvidos mudam rapidamente as propriedades [[Goyet et al. 2000](#)]. Além disso, precisa-se considerar que as razões de Redfield sejam avaliadas ($\text{C:N:P:O}_2 = 106:16:1:-138$), ou seja, que a composição química dos organismos e o equilíbrio dinâmico entre os processos físicos e biológicos não

interfiram nos valores obtidos [Redfield *et al.* 1963]. Ao estimar a razão de Redfield na região a partir de todas as amostras de nutrientes, temos uma razão N:P de $17,1 \pm 5,4$ ($n = 244$ com razões mínimas e máximas entre 11,0 e 24,4, que é ligeiramente superior ao esperado de 16 [Redfield *et al.* 1963]). A incerteza para o C_{ant} foi calculada pela técnica de propagação do erro proposta pelo autor do método [i.e. Touratier *et al.* 2007]. Considerando as incertezas das variáveis medidas, o erro propagado foi de $\pm 6 \mu\text{mol kg}^{-1}$. Por outro lado, considerando todos os parâmetros envolvidos no método de determinação do C_{ant}, o erro determinado foi de $\pm 13 \mu\text{mol kg}^{-1}$.

4.6 Tratamento dos dados

Após medidos e calculados os dados químicos, foi compilado o banco de dados no software Microsoft Excel, facilitando a plotagem no Ocean Data View. Devido ao fato que interanualmente tanto as estações quanto as profundidades de amostragem podem mudar levemente na sua localização, foram feitas as interpolações necessárias no software Matlab para analisar as variações interanuais no estado de acidificação.

Capítulo V: Artigo Científico

Para a obtenção do título de Mestre pelo Programa de Pós-Graduação em Oceanologia, é requerido que o discente realize a submissão de pelo menos um artigo científico como primeiro autor em periódico com corpo indexado. Desse modo, os resultados da pesquisa desenvolvida durante o período de mestrado e a discussão dos resultados serão apresentados em forma de artigo neste Capítulo. O manuscrito intitulado “INTERANNUAL VARIABILITY OF THE OCEAN ACIDIFICATION STATE AND ANTHROPOGENIC CO₂ IN THE BRANSFIELD STRAIT, NORTHERN ANTARCTICA PENINSULA foi submetido para publicação na revista *Journal of Marine Systems*.

INTERANNUAL VARIABILITY OF THE OCEAN ACIDIFICATION STATE
AND ANTHROPOGENIC CO₂ IN THE BRANSFIELD STRAIT, NORTHERN
ANTARCTICA PENINSULA

Juan Camilo Torres-Lasso^{1,2,*}, Rodrigo Kerr^{1,2,*}, Jannine Marquez Lencina-Avila^{1,2}, Iole Beatriz Marques Orselli^{1,2,3,4}, Mariah de Carvalho-Borges^{1,2}, Catherine Goyet^{3,4}, Mauricio M. Mata¹

¹ Laboratório de Estudos dos Oceanos e Clima, Instituto de Oceanografia, Universidade Federal do Rio Grande (FURG), Av. Itália km 8, s/n, Rio Grande, 96203-900, RS, Brazil.

² Brazilian Ocean Acidification Network (BrOA), Av. Itália km 8, Rio Grande, 96203-900, RS, Brazil.

³ IMAGES_ESPACE-DEV, Université de Perpignan Via Domitia (UPVD), 52 ave. Paul Alduy, 66860, Perpignan, France.

⁴ ESPACE-DEV UMR UG UA UM IRD, Maison de la télédétection, 500 rue Jean-François Breton, 34093, Montpellier Cedex 5, France.

* Corresponding author:

Address: Centro de Estudos dos Oceanos e Clima (CEOCEAN), Instituto de Oceanografia – FURG, Avenida Itália km 8, s/n, Campus Carreiros, Rio Grande, RS, Brazil, 96203–900

E-mail: jucatola@gmail.com; rodrigokerr@furg.br

Phone number: +55 53 3233-6858

Highlights

C_{ant} was measured in the Bransfield Strait between 2015 and 2018.

An averaged C_{ant} of 51 ± 13 µmol kg⁻¹ was estimated in the region.

Ω_{Aragonite} is undersaturated below 60 m in the central basin of the Bransfield Strait.

Abstract

We analyzed the hydrographic and chemical properties of the water masses in the Bransfield Strait, a semienclosed basin near the northern Antarctic Peninsula, Southern Ocean. The analyzed dataset was sampled by the Brazilian High Latitude Oceanography Group during four consecutive summer cruises from 2015 to 2018 as part of the activities executed by the NAUTILUS project. Our aims were to (i) quantify the carbon dioxide (CO_2) associated with anthropogenic activities (C_{ant}) in the water masses and (ii) determine the ocean acidification state in the study region. Based on the *Tracer combining Oxygen, inorganic Carbon, and total Alkalinity* (TrOCA) approach, we estimated an averaged C_{ant} concentration of $51 \mu\text{mol kg}^{-1}$ in the Bransfield Strait, which is slightly higher in the central basin ($53 \mu\text{mol kg}^{-1}$) than in the eastern basin ($49 \mu\text{mol kg}^{-1}$). The results indicated that recent ventilation of the Bransfield Strait deep basins resulted in considerable amounts of C_{ant} , mainly through the advection of High Salinity Shelf Water from the Weddell Sea continental shelf. In addition, the averaged depth of the aragonite saturation horizon is ~ 200 m shallower in the central than the eastern basin of the Bransfield Strait. Thus, the C_{ant} intrusion in the Bransfield Strait can rapidly change the ocean acidification state due to the intense mixing of water masses.

Keywords: Human-induced effects, Carbon dioxide, Climatic change, Acidification, Saturation depth, Northern Antarctic Peninsula.

5.1 Introduction

The carbon dioxide (CO_2) concentration in the atmosphere has changed over time depending on the exchanges between reservoirs and is one of the most important factors that control climatic behavior and life conditions on Earth [Pelejero *et al.* 2010]. This concentration has changed over geological time, presenting maximum values greater than 2000 ppmv before plants settled on emerged land and thereafter decreasing with the sequestration of CO_2 by the land [Nelsen *et al.* 2016]. The ocean contributes to the variation in atmospheric CO_2 due to the dependence between gas solubility and temperature (i.e., the solubility is higher at lower temperatures). This process is related to the fact that changes to the CO_2 partial pressure ($p\text{CO}_2$) in seawater imply modifications to the capacity of the ocean to absorb CO_2 , as the interaction between atmosphere and ocean tends to equilibrate the gas concentration through changes in the strength of the gradient between those reservoirs [Lee *et al.* 2003], with large amount of atmospheric CO_2 implying increased and rapid oceanic uptake.

However, the capacity of the ocean to absorb CO_2 not only depends on the gradient but also is controlled by ocean regional hydrodynamics, biogeochemical replenishment, geographical settings, and CO_2 seasonal variations that may change the ocean from a carbon sink to a source [e.g., McNeil *et al.* 2001; Takahashi *et al.* 2002; Sabine 2004; Gregor *et al.* 2018; Murata *et al.* 2019]. CO_2 reacts with seawater when it is absorbed and dissolved over a sequence of chemical reactions, forming carbonic acid, bicarbonate and carbonate ions in different proportions and concentrations depending on the seawater pH [Millero 2007; Fassbender *et al.* 2017]. Thus, the variations in absorbed CO_2 can decrease (increase) ocean pH while decreasing (increasing)

carbonate (bicarbonate) ion concentrations. Once dissolved, the effect of temperature on solubility and biologic absorption in summertime decreases the CO₂ amount and slightly increases the pH, while the equilibrium of the carbonate system tends to produce more carbonate ions [Pelejero *et al.* 2010; Shadwick *et al.* 2013; Conrad & Lovenduski 2015]. However, as more CO₂ is absorbed in winter, decreases in pH and calcium carbonate saturation states (Ω) are accompanied by a weakening in the gradient, decreasing the ocean's ability to absorb CO₂ from the atmosphere.

In the natural carbon cycle, changes in carbonate system parameters have occurred throughout geological periods, which have allowed organisms to adapt to changes in the marine environment. Thus, the planet has buffered the atmospheric CO₂ and reached values between ~180 and 260 ppmv in the last 800,000 years [Ridgwell & Zeebe 2005; Pelejero *et al.* 2010]. However, since the beginning of the industrial revolution (~1750 AD), the marine carbonate system has been affected by the new and rapid input of CO₂ to the atmosphere coming from human-associated activities, mainly from land use, coal, petroleum and gas consumption [Le Quéré *et al.* 2018]. This excess of CO₂ in the atmosphere, which is further stored in the layers of the oceans, is called anthropogenic carbon (C_{ant}). For the ocean to effectively capture C_{ant}, the surface water masses need to sink via increases in density, while the mixture, advection and biogeochemical process will distribute and maintain the C_{ant} outside the system [McNeil *et al.* 2001; Shadwick *et al.* 2013; Legge *et al.* 2017; Humphreys *et al.* 2018]. As the capacity of the ocean to uptake C_{ant} depends on regional hydrographic and biogeochemical parameters, such as ocean temperature, ocean salinity, total alkalinity (A_T) and pCO₂ in surface water masses, some regions are more

susceptible to C_{ant} absorption, such as the polar regions [Shadwick *et al.* 2013; Waugh 2014; Guallart *et al.* 2015; Lovenduski *et al.* 2018]. In Antarctica, where dense and cold water masses ventilate the abyss, considerable amounts of CO₂ flow from the atmosphere to the water masses at the ocean surface due to the increased solubility [Ito & Follows 2013; Pardo *et al.* 2014; Tanhua *et al.* 2017]. The deep convection process allows the oceans to store CO₂ in deep layers for long periods before those water masses return to the surface and interact again with the atmospheric CO₂ [Matear & Lenton 2008; Jones *et al.* 2014]. Thus, as the oceans become more efficient in capturing CO₂, they become more vulnerable to the increase in C_{ant} [Doney *et al.* 2009; Cooley *et al.* 2013].

The formation of the coldest shelf water masses with temperatures near the seawater freezing point over the Weddell Sea continental shelf are associated with the formation of Antarctic Bottom Water [McNeil *et al.* 2001; van Heuven *et al.* 2014], helping to soften the increase in the atmospheric CO₂ concentration to ~414 ppmv due to a C_{ant} uptake of ~1.4 Gt C year⁻¹ [Le Quéré *et al.* 2017, 2018]. This phenomenon causes a rapid change in the marine carbonate system parameters and affects the environmental conditions in which the carbonate-associated marine organisms live [Orr *et al.* 2005; Fabry *et al.* 2009]. As the Bransfield Strait is known to preserve the hydrographic characteristics of the water masses in the deep layers over the Weddell Sea continental shelf [Gordon & Nowlin 1978; Wilson *et al.* 1999; Dotto *et al.* 2016], the aim of this study is to (i) determine the concentration of C_{ant} stored in the deep basins of the Bransfield Strait and (ii) determine the seawater acidification state in the region. The latter objective will be achieved through the investigation of the interannual variations

in pH and calcium carbonate saturation states in this particular area of the Southern Ocean.

5.2 Tectonic and oceanographic features of the Bransfield Strait

The Bransfield Strait (Figure 10) is a roll-back basin that was formed by the subduction of the Phoenix plate under the Antarctic plate in the tertiary period, which separated the tip of the Trinity Peninsula and moved this area to the north as a group of islands called the South Shetland Islands [Galindo-Zaldívar *et al.* 2004; García *et al.* 2009; Anderson & Wellner 2011; López-Martínez *et al.* 2016]. These tectonic processes generated a SW-NE elongated depression conformed by three sub-basins (i.e., western, central and eastern) that are longitudinally limited by the sills associated with the formation of the Deception caldera collapse between the western and central basins and the guyot near Bridgeman Island between the central and eastern basins [Grad *et al.* 1997; Fretzdorff 2004; Dziak *et al.* 2010; Funaki *et al.* 2014]. These geographical settings create a quasi-isolated place, which limits the mixture of water masses between the relatively old, salty and less oxygenated Circumpolar Deep Water (CDW) advected from the Bellingshausen Sea and the external Drake Passage, with relatively recent, cold and highly oxygenated Weddell Sea Shelf Waters (HSSW and LSSW) [Wilson *et al.* 1999; Dotto *et al.* 2016].

The Weddell Sea Shelf Waters can be sourced from both the western and southern continental shelves of the Weddell Sea [Gordon *et al.* 2001; Nicholls *et al.* 2009; Brown *et al.* 2015; van Caspel *et al.* 2018], and the trajectories of the transport are controlled by the westward flow of the Antarctic Coastal Current [Deacon 1937], which advects the water over the shelf from the east Weddell Sea to the tip of the Antarctic Peninsula [Fahrbach *et al.* 1992; Gordon 1998;

Thompson *et al.* 2009]. As the water masses are advected over the Weddell Sea continental shelf, they are influenced by brine rejection [Frölicher *et al.* 2015]. This process increases the salinity and decreases the temperature due to the basal contact with sea ice, thereby generating high-density shelf water [Hellmer *et al.* 2017] that is prone to absorbing CO₂ from the atmosphere. As the shelf water arrives at the tip of the peninsula, it passes through the Antarctic Sound or follows the current that flows in a counterclockwise direction past the northern side of Joinville Island into the Bransfield Strait [Gordon *et al.* 2000; Renner *et al.* 2009; Thompson *et al.* 2009]. Thus, the dense shelf water masses in the Weddell Sea are prone to filling the deep water columns of the central and eastern basins of the Bransfield Strait after they cascade down into the abyss of the basins [Gordon *et al.* 2000], allowing the deep zones of the Bransfield Strait to preserve the signature of the hydrographic characteristics of the Weddell Sea shelf [Gordon & Nowlin 1978; Wilson *et al.* 1999]. Model results have indicated that the central basin of the Bransfield Strait is highly influenced by the shelf water masses from near the Larsen Ice Shelf, whereas the eastern basin is strongly influenced by the Filchner-Ronne Ice Shelf [van Caspel *et al.* 2018]. In addition, it is expected that the shelf waters over the Weddell Sea continental shelves will have enough time to become completely or nearly balanced with the atmospheric CO₂ concentration before entering the strait [van Heuven *et al.* 2014], as the residence time of the water over the continental shelf of the Weddell Sea is approximately 5-6 years [Schlosser *et al.* 1991; Mensch *et al.* 1998].

The influences of the El Niño Southern Oscillation (ENSO) and the Southern Annular Mode (SAM) modify the properties of the water masses that are advected into the Bransfield Strait [Dotto *et al.* 2016; van Caspel *et al.* 2018],

indicating the strength of the contributions of each climatic mode in each basin. Negative (positive) phases of ENSO are associated with more (less) saline and dense water due to changes in the percentage of modified CDW (mCDW) in the western basin of the Bransfield Strait [[Ruiz Barlett et al. 2018](#)].

Positive (negative) phases of SAM and changes in the strength of the westerlies limit (allow) the input of Weddell Sea Shelf Waters to the Bransfield Strait [[Dotto et al. 2016](#)]. When a negative ENSO phase acts together with a positive SAM, less water arrives from the Weddell Sea to the Bransfield Strait. As older CDW has a higher C_T concentration, the ENSO enhances the mixture between this water mass and the surface layer, altering the C_T concentration. In addition, the variations in the westerly winds associated with a positive SAM modify the C_T concentration due to an increase in the input of mCDW, surface turbidity, changes in ventilation time and restriction of the water advected to the northern Antarctic Peninsula [[Conrad & Lovenduski 2015](#)]. In addition, the properties of the shelf water masses in the deep layers of the Bransfield basins can vary seasonally, reflecting the periodicity of the advection of Weddell Sea Shelf Water in the Bransfield Strait and the intense mesoscale activity that occurs in the region [[Gordon et al. 2000](#); [Sangrà et al. 2011](#); [Ruiz Barlett et al. 2018](#)].

In the western basin of the Bransfield Strait (which is relatively shallow compared to the other basins), a mixture of less dense water that is advected from the Bellingshausen Sea and Drake Passage is formed [[van Caspel et al. 2018](#)]. This less dense water with a high mCDW concentration crosses into the central and eastern basins at intermediate levels [[Ruiz Barlett et al. 2018](#)], mainly entering the region over the southern slope of the South Shetland Islands and is limited to the upper layers by density [[Sangrà et al. 2017](#); [van Caspel et al. 2018](#)].

Thus, this water mass controls the hydrography in the surface and intermediate layers, and the physical and chemical properties of these layers are easily varied due to the interaction with the atmosphere. While the surface and intermediate layers of the central and eastern basins of the Bransfield Strait are influenced by the water masses from the Bellingshausen Sea that are advected through the western basin, the deep layer is associated with the coldest shelf water masses from the Weddell Sea continental shelves with temperatures near the seawater freezing point.

After these water masses advect over the Weddell Sea continental shelves and reach the tip of the peninsula, they pass through the Antarctic Sound or follow the current in a counterclockwise direction past the northern side of Joinville Island and into the central or eastern basins of the Bransfield Strait, respectively [Gordon *et al.* 2001; Renner *et al.* 2009; Thompson *et al.* 2009; Sangrà *et al.* 2011; Kerr *et al.* 2018]. In the deep layer of the central basin of the Bransfield Strait, the properties of the water masses indicate that during advection over the continental shelves, 80% of the Weddell Sea Shelf Water (HSSW and LSSW, with a predominance of HSSW) is mixed with ~20% of mCDW [Dotto *et al.* 2016]. The proportions in the resultant mixture are controlled by the strength of the dominant climate mode [van Caspel *et al.* 2015; Dotto *et al.* 2016]. When the amount of dense water in the central basin of the Bransfield Strait exceeds the bathymetrical limit (near the Bridgeman Guyot), the water overflows to the deep layer of the eastern basin [Wilson *et al.* 1999; Gordon *et al.* 2000]. The eastern basin of the Bransfield Strait is filled with water composed of ~65% of Weddell Sea Shelf Waters (HSSW and LSSW, with predominance of LSSW) that are advected to the north of Joinville Island and mixed with ~35% of mCDW [Dotto *et*

al. 2016], which is associated with the Antarctic Circumpolar Current before entering the strait [Hofmann *et al.* 1996; Gordon *et al.* 2000].

5.3 Data and methods

This research was developed by the Brazilian High Latitude Oceanography Group [GOAL; Mata *et al.* 2018] within the scope of the NAUTILUS project and under the umbrella of the Brazilian Antarctic Program (PROANTAR). Here, we analyzed the hydrographic and chemical data obtained onboard the Brazilian Navy RV Almirante Maximiano, which sailed around the northern Antarctic Peninsula during four consecutive summer periods between 2015 and 2018 [e.g., Kerr *et al.* 2017a].

5.3.1 Sampling strategy

The hydrographic data in the Bransfield Strait (Figure 10) were measured with a Sea-Bird conductivity, temperature, and depth (CTD) 911+ coupled in a carousel system with 24 Niskin bottles (5 or 12 L) and duplicate sensors for each temperature, conductivity and dissolved oxygen. The difference between the temperature sensors was approximately ± 0.002 °C, while the difference in salinity was estimated to be ± 0.003 . At each station, the depths at which the bottles were closed to collect discrete seawater samples for chemical analyses were chosen through one-time observations of the respective hydrographic profiles. Once the CTD-carousel system was in the vessel, discrete samples were taken in the following order for measurements of dissolved oxygen (DO), pH, total alkalinity (A_T), total dissolved inorganic carbon (C_T), and dissolved macronutrients. The numbers of discrete samples analyzed in this work were 93,

112, 114 and 111 samples at 20, 16, 26, and 19 stations in 2015, 2016, 2017 and 2018, respectively.

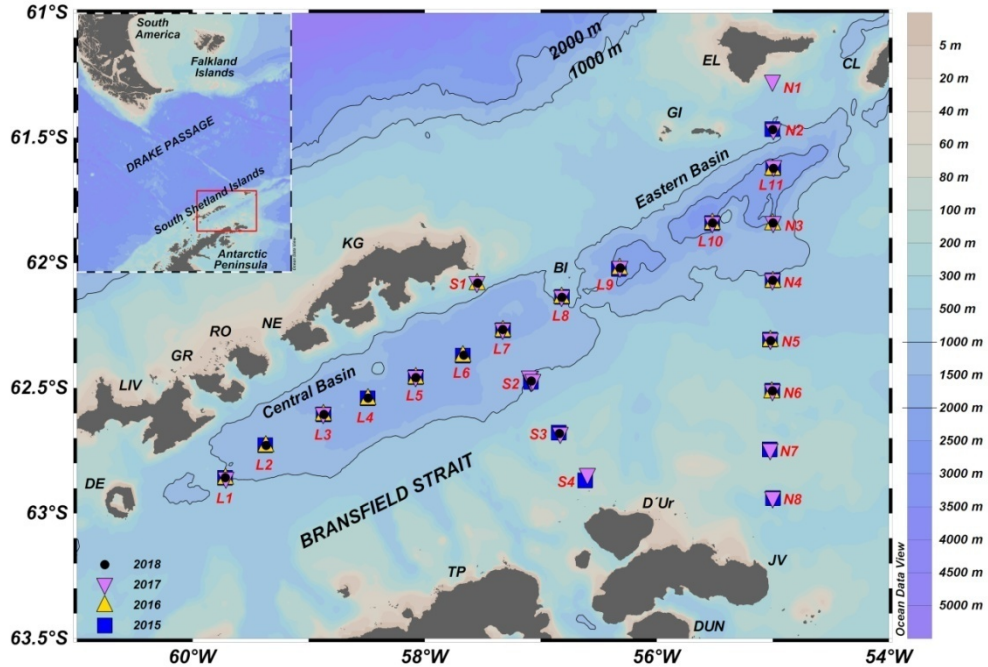


Figure 10: Map of the Bransfield Strait showing the geographical settings and the oceanographic stations that were sampled in the longitudinal (L), northern (N) and southern (S) sections between 2015 and 2018. Blue squares, yellow triangles, magenta inverted triangles and black dots show the positions of the CTD oceanographic stations during the NAUTILUS cruises for the years 2015, 2016, 2017 and 2018, respectively. The South Shetland Islands are composed of Deception Is. (DE), Livingston Is. (LIV), Greenwich Is. (GR), Robert Is. (RO), Nelson Is. (NE), King George Is. (KG), Bridgeman Is. (BI), Gibbs Is. (GI), Elephant Is. (EL) and Clarence Is. (CL), while in the tip of the Antarctic Peninsula is composed of D'Urville Is. (D'Ur), Joinville Is. (JV), Dundee Is. (DUN) and the Trinity Peninsula (TP). The bathymetry is represented by the color scale bar to the right, with the 1000 m and 2000 m isobaths highlighted by the thin gray lines. The inset map shows the location of the Bransfield Strait in the northern Antarctic Peninsula, Southern Ocean.

5.3.2 Dissolved oxygen measurements

The DO was analyzed onboard using a modified Winkler method to calibrate the CTD sensors. The measurements taken in 2015 and 2016 were well correlated with those obtained by the sensors, allowing for their calibration. The DO correction equations were $0.7315 * \text{DO}_{\text{(CTD)}} + 0.2142$, with a determination coefficient (r^2) of 0.99 for 2015 and $0.9608 * \text{DO}_{\text{(CTD)}} - 0.7295$, with r^2 of 0.94 for 2016. However, we had problems with DO acquisition in both 2017 and 2018

because of freezing of the sensors and/or chemical analytical issues, which prevented the correction of the DO values obtained by the sensors during those years. Thus, based on the DO values from the first two years of the NAUTILUS cruises and assuming that the oxygen distribution over a large scale within the ocean is not significantly affected by human activities [Touratier *et al.* 2007], a polynomial equation was developed using the multiple linear regression method to estimate the DO values in the years of 2017 and 2018. We considered the temperature and salinity data ($n = 1799$) obtained from the station over the deepest part of the central basin of the Bransfield Strait (L5 station, Figure 10) as independent variables and the dissolved oxygen Winkler-averaged values from 2015 – 2016 as the dependent variable. Thus, the following equation (Eq. 1) was used to determine the consistent DO values for the four years, considering the seawater DO concentrations in mL L^{-1} , seawater temperature (T) in $^{\circ}\text{C}$ and seawater salinity (S) in practical salinity units. The estimated uncertainty of the DO values based on Eq. 1 was $\pm 0.07 \text{ mL L}^{-1}$ or $\pm 3.0 \mu\text{mol kg}^{-1}$.

$$\text{DO} = 226.0885 + (\text{T}^* - 1.18919) + (\text{S}^* - 6.40931) + 0.073454 \quad \text{Equation 1.}$$

5.3.3 Dissolved macronutrient measurements

The dissolved inorganic nutrients (i.e., ammonia, phosphate, nitrate, nitrite and silicate) were used as ancillary data to improve the accuracy of the calculated pH at the total scale and the C_T values. Additionally, these data were used to estimate the Redfield ratio between all dissolved nitrogen species (ammonia, nitrate, nitrite) and phosphate. The samples were collected in 60 mL amber plastic bottles and immediately frozen until they were analyzed with a FIAstar™ 5000 Analyzer Module in the Multi-User Unit for Environmental Analysis (UMAA)

at the Federal University of Rio de Janeiro (UFRJ), Rio de Janeiro, Brazil. The ammonia, phosphate, nitrate, nitrite and silicate detection (quantification) limits in μM are 0.05 (0.15), 0.10 (0.30), 0.11 (0.33), 0.02 (0.06) and 0.50 (1.50), respectively.

5.3.4 Carbonate system measurements

The pH samples were collected in 125 mL amber borosilicate bottles and analyzed onboard with a potentiometric Metrohm® 827 pH meter within two hours of sampling. Two samples were taken from the deepest depth sampled during each CTD cast to control for the temperature during pH analysis because the difference between the calibration temperature and the sample temperature needs to be in a range of 3 °C. Fluka® Sigma-Aldrich® buffer solutions with pH values equal to 4.008 (potassium hydrogen phthalate + phenylmercury chloride) and 7.413 (disodium hydrogen phosphate + potassium dihydrogen phosphate) were used to standardize the pH electrode. We applied the equation developed by [Gieskes \[1969\]](#) to correct the pH measurements according to the *in situ* temperature. The pH uncertainty was ≤ 0.05 pH units in NBS scale. We used the values recast to the total scale (pH_{total}) and the *in situ* temperatures to better reveal the correlation between the chemical variables. The pH_{total} was determined through CO2Sys v1.1 software [[Lewis & Wallace 1998](#)] using the input parameters pH_{NBS} , A_T , temperature, salinity, phosphate and silicate with the sulfate and borate constants from [Dickson \[1990\]](#) and [Uppström \[1974\]](#), respectively, and the equilibrium constants for the dissociation of carbonic acid from [Goyet and Poisson \[1989\]](#). The pH_{total} uncertainty was estimated to be ± 0.03 pH units.

The water samples for A_T and C_T measurements were taken in 250 mL and 500 mL prewashed borosilicate bottles and immediately poisoned with 50 μL and 100 μL , respectively, of a supersaturated mercury chloride (HgCl_2) solution if the samples were not analyzed onboard. The samples were conserved at 4 °C until analysis in the laboratory. The analyses were conducted in the LEOC laboratory in 2015 and 2017 and onboard in 2016 and 2018. We followed the procedures from [DOE \[1994\]](#) based on potentiometric titration in a closed cell under temperature-controlled conditions of 25 ± 0.1 °C, which were sustained by a Tamson® TLC 15 thermostatic bath. The ionic strengths of the hydrochloric acid (HCl, 0.1 N) solutions were adjusted to the mean seawater salinity of each cruise by the addition of sodium chloride (NaCl). We used a Methrom® Titrando 808 (5 mL) automated titrator together with a combined glass electrode (Methrom®6.0262.100) for the years 2015 and 2017 [[e.g., Kerr et al. 2017b](#)] and an ABU901 Autoburette (5 mL) from Radiometer Analytical® connected to a ProLab 3000 pH meter by Schott Instruments® coupled with a BlueLine 18 pH glass electrode from SI Analytics® for the years 2016 and 2018. We used certified reference material batch numbers 96 (2015), 149 (2016 and 2017), and 162 (2018) across all measurements to ensure quality control of the analysis [[Dickson et al. 2003](#)]. The A_T precision was determined to be ± 3.0 , ± 3.4 , ± 2.8 and ± 5.7 $\mu\text{mol kg}^{-1}$ for the years 2015, 2016, 2017 and 2018, respectively.

Although the C_T estimations exhibited good precision (± 5.0 , ± 4.4 , ± 2.9 and ± 3.4 $\mu\text{mol kg}^{-1}$ for the years 2015, 2016, 2017 and 2018, respectively), for some particular oceanographic stations and years, the obtained C_T values were considered overestimated during the quality control verification of the carbonate system parameters. Thus, for consistency of the analyses, we opted to determine

the C_T and calcium carbonate saturation (Ω) used in this study through the application of CO2Sys v1.1 software [Lewis & Wallace 1998] with the same constants described for the determination of pH and using the temperature, salinity, A_T , pH_{total} , phosphate and silicate as input parameters. Millero [2007] determined an estimated C_T uncertainty of $3.8 \mu\text{mol kg}^{-1}$ when the parameter was calculated by using the A_T -pH pair. Here, through the propagation error technique [e.g., Carvalho-Borges *et al.* 2018], the uncertainties were determined to be ± 5.9 , ± 5.9 , ± 6.3 and $\pm 4.9 \mu\text{mol kg}^{-1}$ for C_T ; ± 0.06 , ± 0.08 , ± 0.06 and ± 0.08 for Ω_{Calcite} ; and ± 0.04 , ± 0.05 , ± 0.04 and ± 0.05 for $\Omega_{\text{Aragonite}}$ in the years 2015, 2016, 2017 and 2018, respectively.

5.3.5 Anthropogenic carbon (C_{ant}) estimation

We apply the *Tracer combining Oxygen, inorganic Carbon, and total Alkalinity* (TrOCA) approach proposed by Touratier and Goyet [2004a] and actualized in Touratier *et al.* [2007] to determine the C_{ant} concentration. This method is widely accepted by the international community and has been used worldwide in the Pacific Ocean [e.g., Goyet *et al.* 2009; Wagener *et al.* 2018], the Atlantic Ocean [e.g., Touratier and Goyet, 2004b; Touratier *et al.* 2005, 2016; Carvalho-Borges *et al.* 2018; Orselli *et al.* 2018], the Mediterranean Sea [e.g., Krasakopoulou *et al.* 2011; Touratier and Goyet, 2011; Hassoun *et al.* 2015; Ingrosso *et al.* 2017] and the Southern Ocean [e.g., Lo Monaco, 2005; Sandrini *et al.* 2007; Kerr *et al.* 2017a; Pardo *et al.* 2017; Lencina-Avila *et al.* 2018]. In addition, the TrOCA approach has exhibited a good response compared with the more complex estimation methods [e.g., Touratier *et al.* 2007]. We applied equation 2 to derive the C_{ant} concentration, which depends on DO ($\mu\text{mol kg}^{-1}$), A_T ($\mu\text{mol kg}^{-1}$), C_T ($\mu\text{mol kg}^{-1}$), and potential temperature (θ , $^{\circ}\text{C}$).

$$C_{\text{ant}} = \frac{\text{DO} + 1.279(C_T - 0.5A_T) - e^{\left[7.511 - (1.087 \times 10^{-2})\theta_0 - \left(\frac{7.81 \times 10^5}{A_T^2}\right)\right]}}{1.279} \quad \text{Equation 2.}$$

As the method is based on the Redfield ratio, we need to consider that the dynamic balance between the biological consumption of dissolved inorganic nutrients and its supply is enough to allow for biological processes without modifying their concentrations in the water column. Taking the data obtained across the four years at all depths, the obtained N:P ratio was 17.1 ± 5.4 ($n = 244$ with minimum and maximum ratios of 11.0 and 24.4, respectively), which is close to the Redfield ratio of 16:1 [Redfield *et al.* 1963]. Additionally, the premises of the approach assume that the dissolved content in the surface mixed layer was not in equilibrium with the atmosphere; thus, the C_{ant} results are those determined below the depth of 250 m (i.e., excluding the surface layer). The C_{ant} uncertainty was calculated by the propagation error technique [Touratier *et al.* 2007], and considering the uncertainties of only the input variables, the error was $\pm 6 \mu\text{mol kg}^{-1}$. However, when considering all the parameters involved in the C_{ant} determination method, the error was determined to be $13 \mu\text{mol kg}^{-1}$. The C_{ant} uncertainty found here is within the range expected for the approach used and comparable to those found using other methodologies.

5.4 Results

Due to the large number of hydrographic profiles that were analyzed in this study, we show only the relevant profiles related to the determination of the ocean acidification state from the longitudinal (L) section along the central and eastern basins of the Bransfield Strait (Figure 10). Therefore, we present the results according to the water layers determined by the potential density, i.e., the surface ($\leq 27.75 \text{ kg m}^{-3}$), intermediate ($27.75 \text{ kg m}^{-3} < \theta_0 < 27.81 \text{ kg m}^{-3}$) and deep (\geq

27.81 kg m^{-3}) layers. The surface layer depth was estimated by considering the observations of Sangrà *et al.* [2011] and the influence of mesoscale activity in the region, and this layer spanned from the surface to 250 m, while the deep layer was determined as the averaged density in which the density variations between the basins were considerable. As the eastern basin of the Bransfield Strait is less dense than the other basins, the 27.81 kg m^{-3} pycnocline (which is consistently near 750 m in the central basin) can reach the bottom in the eastern basin, making the separation of layers inefficient. Thus, for the statistical analysis and comparison of the carbonate system parameters between basins, the different layers were determined to be from the surface to 250 m for the surface layer, between 250 m and 750 m for the intermediary layer, and below 750 m for the deep layer. The reader is referred to the Supplementary Material for the distributions of the properties in all other hydrographic sections that were analyzed (i.e., N and S sections, Figure 10).

5.4.1 Interannual variability of the water mass properties in the Bransfield Strait

The presence of HSSW in the deep layer of the central basin of the Bransfield Strait is noted, while mCDW occurs in the intermediate layers (Figure 11). Clear interannual variations in the hydrographic properties of the HSSW (based on density limits) are observed in the deep layer of the central basin (Figures 11a, 12). Thus, in comparison, the densest HSSW is observed during 2016 (-1.68°C and 34.6) and 2017 (-1.67°C and 34.6), while this water mass is

less dense during 2015 (-1.59°C and 34.59) and 2018 (-1.6°C and 34.59), reinforcing the finding that the densest characteristics are observed during 2016 and 2017 (Figures 11a, 12). This HSSW is trapped in the central basin of the Bransfield Strait, maintaining high-density characteristics and preventing the mixture of water masses (Figures 12, S1, S4, S7 and S10).

The hydrography of the eastern basin of the Bransfield Strait is highly influenced by the input of the LSSW mixed with the external mCDW, presenting a more homogenized water column over the full depth profile (Figure 11b). Despite being deeper than the central basin, the deep layers in the eastern basin are much less dense than those in the central basin due to the high temperature associated with the mixture with mCDW (Figure 11b). In addition, the bottom waters in the central basin are densest during 2016 and 2017 (Figure 11b). A decrease in density at the intermediate level is observed from 2015 to 2017, and the density in this layer slightly increases in 2018 (Figure 11b).

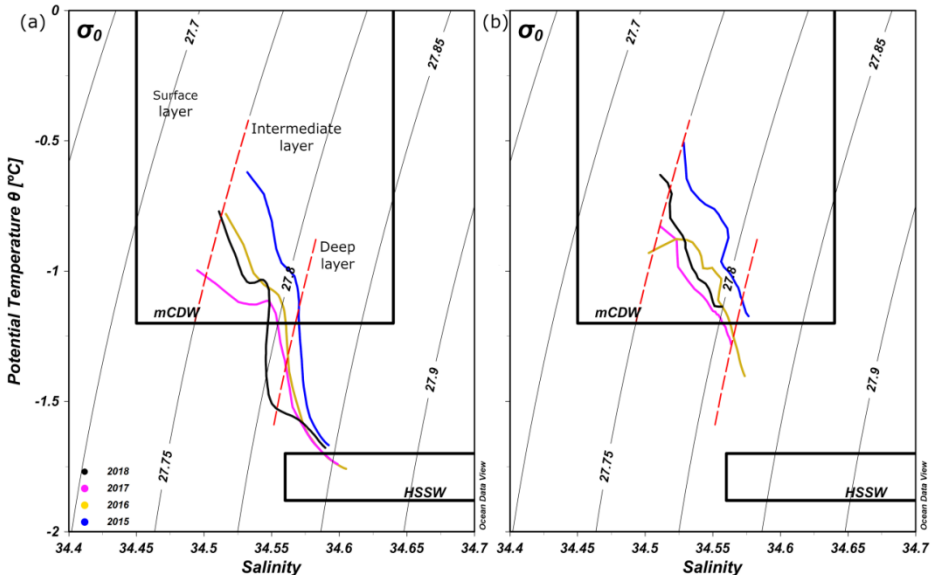


Figure 11: θ -S depth-averaged diagrams for the CTD stations of the central (a) and eastern (b) basins of the Bransfield Strait during the NAUTILUS cruises between 2015 and 2018. The colored lines represent each specific year of sampling: blue-2015, yellow-2016, magenta-2017, and black-2018. The definitions of High Salinity Shelf Water (HSSW) and modified Circumpolar Deep Water (mCDW) followed the definitions proposed by Carmack [1974] and Robertson *et al.* [2002].

The gray lines mark the potential density (kg m^{-3}) isolines in reference to the density at the surface, and the dashed red lines mark the potential density selected as limits between the water layers (i.e., $< 27.75 \text{ kg m}^{-3}$ for the surface layer, between 27.75 kg m^{-3} and 27.81 kg m^{-3} for the intermediate layer, and $> 27.81 \text{ kg m}^{-3}$ for the deep layer).

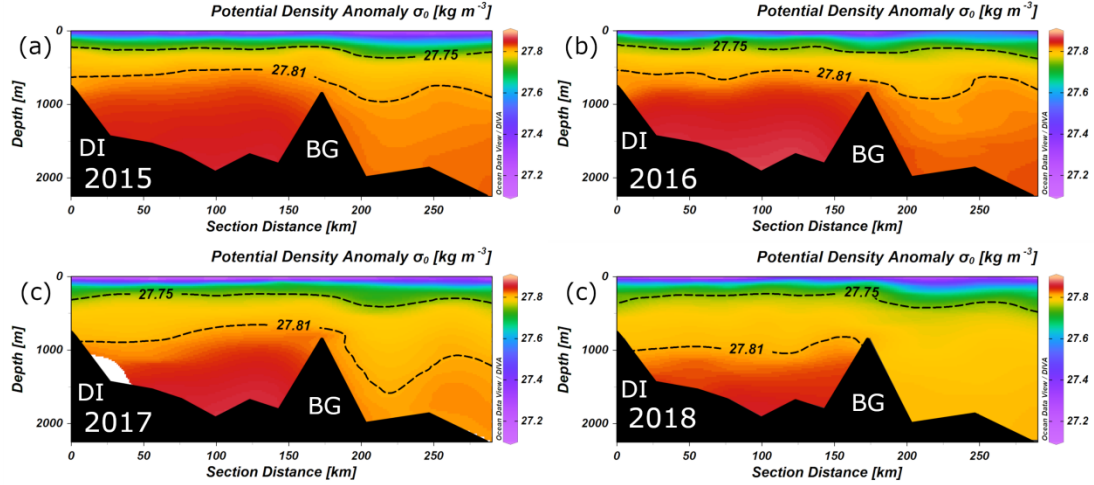


Figure 12: Vertical profiles of the potential density anomaly (in kg m^{-3}) in the Bransfield Strait across the L section in 2015 (a), 2016 (b), 2017 (c) and 2018 (d). The central basin of the Bransfield Strait is located between Deception Island (DI) and the Bridgeman Guyot (BG), while the eastern basin is located northeast of the BG (right side of the images). The black contours are the pycnoclines marked as the limits between layers ($< 27.75 \text{ kg m}^{-3}$ is considered the surface layer; between 27.75 kg m^{-3} and 27.81 kg m^{-3} is considered the intermediate layer, and $> 27.81 \text{ kg m}^{-3}$ is considered the deep layer).

We observe the highest DO concentration (Figure 13) over the years to be associated with the HSSW in the deep layer of the central basin of the Bransfield Strait (Figures S1, S4, S7 and S10 for 2015, 2016, 2017 and 2018, respectively). Although a marked interannual variability is observed in the distribution of this property, on average, 2016 and 2018 have the highest DO concentrations when considering all the water levels ($278 \mu\text{mol kg}^{-1}$; Figure 13b and 13d). This value is $4 \mu\text{mol kg}^{-1}$ lower and $2 \mu\text{mol kg}^{-1}$ higher on average for the years 2015 and 2017 (Figure 13a and 13c), respectively. No marked changes were observed for the DO concentration in the intermediate layers of the central basin of the Bransfield Strait, except for in 2015 (Table S1).

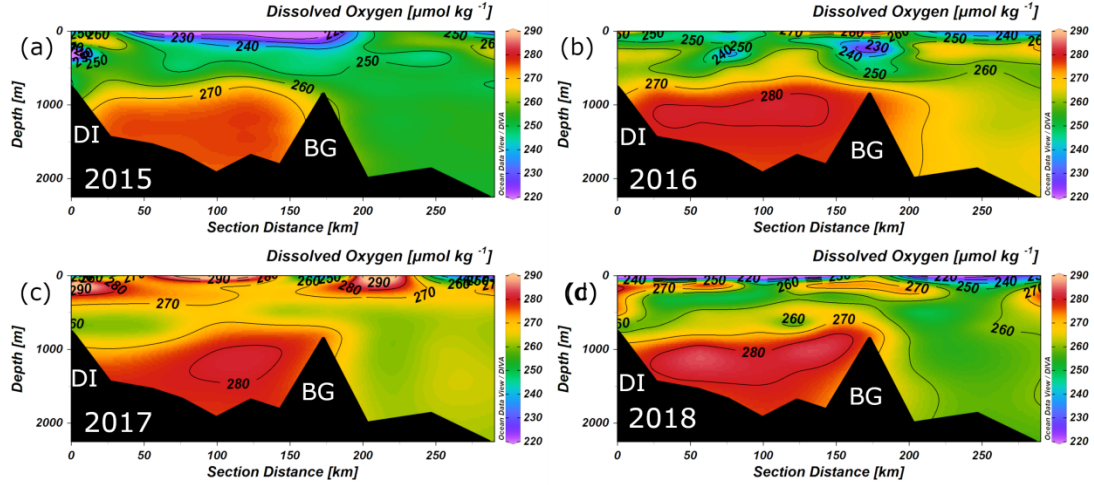


Figure 13: The same as Figure 12 but for dissolved oxygen. The black contours are the concentration isolines in $\mu\text{mol kg}^{-1}$.

Unlike oxygen, the interannual distribution in $A_T - C_T$ in the Bransfield Strait does not show any spatial trend, and its distribution across the analyzed years is highly variable (Figures S2, S5, S8 and S11 for 2015, 2016, 2017 and 2018, respectively). On average, the A_T concentration in 2015 ($2323 \mu\text{mol kg}^{-1}$) was lower than that in the other years ($2344, 2354$ and $2351 \mu\text{mol kg}^{-1}$ for 2016, 2017 and 2018, respectively). The average C_T concentrations were $2262, 2258, 2276$ and $2279 \mu\text{mol kg}^{-1}$ for 2015, 2016, 2017 and 2018, respectively (Table S2). The estimation of the average $A_T - C_T$ concentrations in each layer over the four years indicates that the A_T (Figure 14a) in the surface layer presents a concentration ($2332 \pm 22 \mu\text{mol kg}^{-1}$) that is almost $10 \mu\text{mol kg}^{-1}$ lower than that in the intermediate ($2345 \pm 20 \mu\text{mol kg}^{-1}$) and deep layers ($2342 \pm 23 \mu\text{mol kg}^{-1}$). The C_T (Figure 14b) also presents a low average concentration in the surface layer ($2257 \pm 27 \mu\text{mol kg}^{-1}$), which is almost $20 \mu\text{mol kg}^{-1}$ higher than that in the intermediate ($2277 \pm 19 \mu\text{mol kg}^{-1}$) and deep ($2268 \pm 21 \mu\text{mol kg}^{-1}$) layers. While the $A_T - C_T$ concentrations in both basins still exhibit annual variability, the differences in these parameters across the water column are between 5 and 15

$\mu\text{mol kg}^{-1}$. While the interannual variations are highly variable across layers and basins, the NA_T - NC_T diagram shows that calcification/dissolution is the major process that changes these parameters in the study region, with an $\text{NC}_T:\text{NA}_T$ averaged ratio of 0.97 (with values between 0.94 and 0.99), although water mass dilution/evaporation can also play a role in such changes, mainly for waters below 250 m (Figure 15).

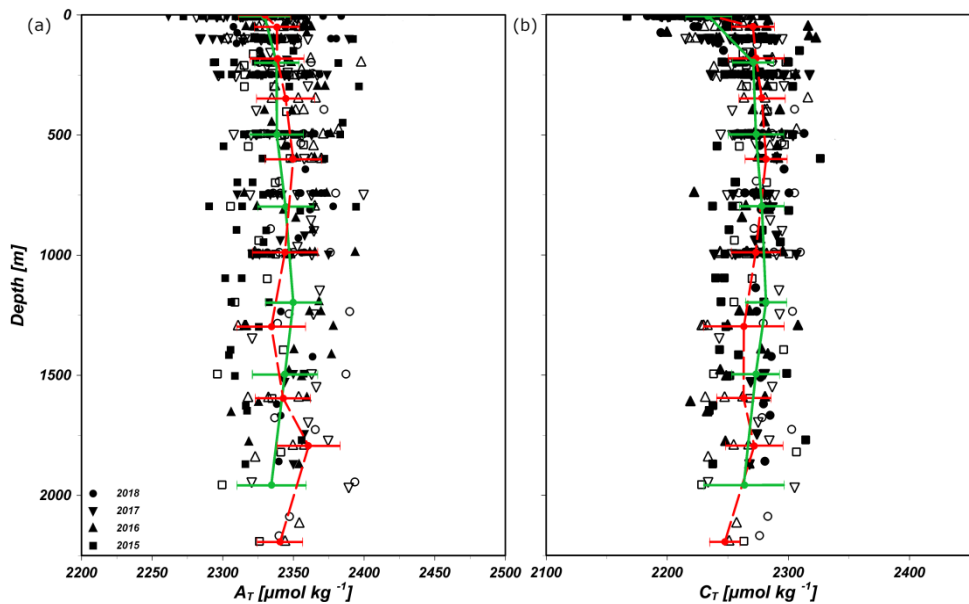


Figure 14: Vertical concentrations (in $\mu\text{mol kg}^{-1}$) of A_T (left) and C_T (right) in the Bransfield Strait. The symbols depict each year in which the samples were taken (squares, triangles, inverted triangles and dots for the years 2015, 2016, 2017 and 2018, respectively), while the symbols indicate the data per basin (solid symbols for the central basin and open for the eastern basin). The lines indicate the averaged concentration of all years with the standard deviations (green lines for the central basin and red lines for the eastern basin).

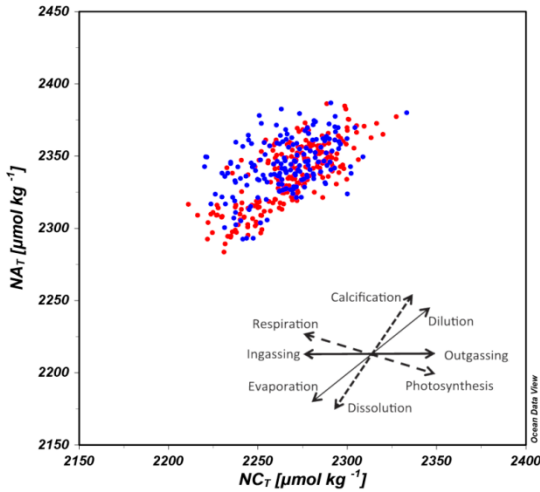


Figure 15: A_T-C_T salinity normalized (NA_T-NC_T) diagram, considering an averaged salinity of 34.469 for the region. Blue (red) dots denote samples above (below) 250 m.

5.4.2 Interannual changes in the seawater acidification state in the Bransfield Strait

Our results indicate that the deepest levels of the central and eastern basins of the Bransfield Strait are filled with dense water derived from HSSW (with a colder and more oxygenated variety filling the central basin than that in the eastern basin). This water is mainly sourced and advected into the Bransfield Strait from the continental shelf of the Weddell Sea (Figures 11 and 12). On the other hand, the surface and intermediate layers are highly influenced by intrusions of mCDW entering the region from the western basin and Drake Passage (Figures 11 and 12). Thus, changes in the proportions of the mixture of the main source waters will alter the water mass volume and the distribution of the biogeochemical parameters on a temporal scale, which can vary interannually. In this sense, we further describe the state of ocean acidification in

the study region based on the C_{ant} storage in the water masses and pH and Ω changes among the study years.

5.4.2.1 Interannual variability in the C_{ant} distribution

It is evident that the C_{ant} distribution (Figure 16) in the basins of the Bransfield Strait fairly coincides with the A_T distribution (Figures S2, S5, S8 and S11 for 2015, 2016, 2017 and 2018, respectively). In 2015 (Figure 16a), a noticeable C_{ant} input with an averaged concentration of $58 \pm 8 \mu\text{mol kg}^{-1}$ was observed near the northeastern part (stations L7 and L8) of the central basin and in the eastern basin around station L10 (Figure 16a). For this particular year, the deep layer in the central basin of the Bransfield Strait had the highest average C_{ant} concentration, which was estimated to be $66 \pm 3 \mu\text{mol kg}^{-1}$ (Table S2). In contrast, a low average C_{ant} concentration of $50 \pm 9 \mu\text{mol kg}^{-1}$ was observed in the deep layer of the eastern basin of the Bransfield Strait during 2015 (Table S2). In 2016, a strong signal of C_{ant} intrusion, with similar magnitudes, was also observed in the central basin of the Bransfield Strait through stations L7 and L8 (Figure 16b). However, a low average C_{ant} concentration of $33 \pm 4 \mu\text{mol kg}^{-1}$ was found in the deep layer of the eastern basin of the Bransfield Strait (Table S2). In 2017, the C_{ant} concentration in the central basin of the Bransfield Strait was $63 \pm 1 \mu\text{mol kg}^{-1}$ in the intermediate layer (Figure 16c, Table S2), which was the highest average C_{ant} concentration throughout the years that were analyzed. In 2018, while high C_{ant} concentrations were presented in the central basin of the Bransfield Strait (Figure 16d), the intrusion of C_{ant} around stations L7 and L8 was not clear. In addition, the deep layer in the eastern basin of the Bransfield Strait had the highest average C_{ant} concentration of $57 \pm 3 \mu\text{mol kg}^{-1}$ when compared

with the other years (Table S2); however, the biogeochemical parameters in the region were not completely sampled at all depths (Figure 16d).

In summary, the accumulation of C_{ant} in the intermediate and deep layers of the Bransfield Strait basins was, on average, higher during 2015 than in the other years (Table S2). In 2015, the averaged C_{ant} concentration was estimated to be $\sim 58 \mu\text{mol kg}^{-1}$, which is close to the value of $\sim 54 \mu\text{mol kg}^{-1}$ that was observed in both 2017 and 2018. During 2016, the low C_{ant} accumulation of $\sim 47 \mu\text{mol kg}^{-1}$ was related to the low C_{ant} concentration observed in the deep layer of the eastern basin (Table S2). On average, a difference of $\sim 10 \mu\text{mol kg}^{-1}$ in C_{ant} is found between the basins, with the central basin accumulating a higher concentration than the eastern basin, varying in only 2018, but the incomplete occupation of the eastern basin could be related to the reported accumulation.

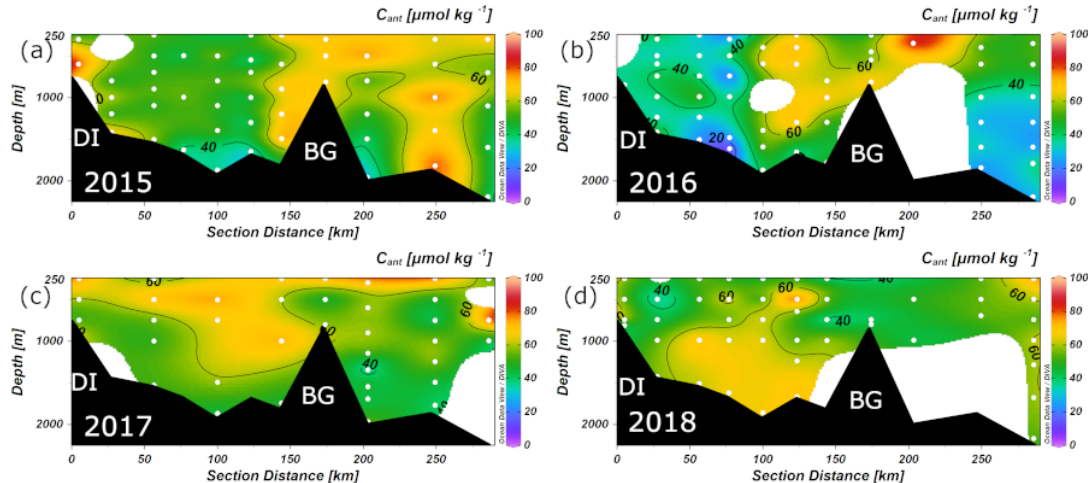


Figure 16: Vertical profiles of C_{ant} in the Bransfield Strait across the L section in the years of 2015 (a), 2016 (b), 2017 (c) and 2018 (d). The central basin of the Bransfield Strait is located between stations L1 (north of Deception Island) and L8 (over the Bridgeman Guyot). The eastern basin of the Bransfield Strait is located between stations L8 and L11 (near Elephant Island). The white dots depict the discrete sampling depths for biogeochemical analyses. The black contours are isolines of concentration in $\mu\text{mol kg}^{-1}$.

The θ -S- C_{ant} diagram did not show a clear range of C_{ant} concentration values along the isopycnal levels (Figure 17), which revealed the spatial pattern of the C_{ant} variability in the region (Figure 16). An exception was observed for the

denser water mass that was found in the eastern basin during 2016, which presented an averaged C_{ant} concentration of $\sim 15 \text{ } \mu\text{mol kg}^{-1}$ at the seabed (Figures 16b, S5). This result likely indicates that this dense water mass with a relatively small C_{ant} concentration arrived and sank directly into that basin, with reduced mixture with other upper water masses during its flow from the source area. In general, the central basin has a higher C_{ant} concentration than the eastern basin for deep levels below $\sim 500 \text{ m}$ (Figure 17). Thus, on average, the standard deviation ranges between 3 and $16 \text{ } \mu\text{mol kg}^{-1}$ of C_{ant} at the different depths, with a higher concentration occurring in the central basin than in the eastern basin (Table S2). The exception is the year 2018 (Figure 16), but the incomplete occupation of the eastern basin at the deepest level did not allow for such comparison.

The four-year averaged C_{ant} concentration (Figure 17) in the intermediate layer ($54 \pm 12 \text{ } \mu\text{mol kg}^{-1}$) is slightly higher than that in the deep layer ($49 \pm 14 \text{ } \mu\text{mol kg}^{-1}$), with higher values in the central basin ($54 \pm 14 \text{ } \mu\text{mol kg}^{-1}$ and $51 \pm 14 \text{ } \mu\text{mol kg}^{-1}$ in the intermediate and deep layers, respectively) than in the eastern basin ($46 \pm 14 \text{ } \mu\text{mol kg}^{-1}$ and $53 \pm 12 \text{ } \mu\text{mol kg}^{-1}$ in the intermediate and deep layers, respectively).

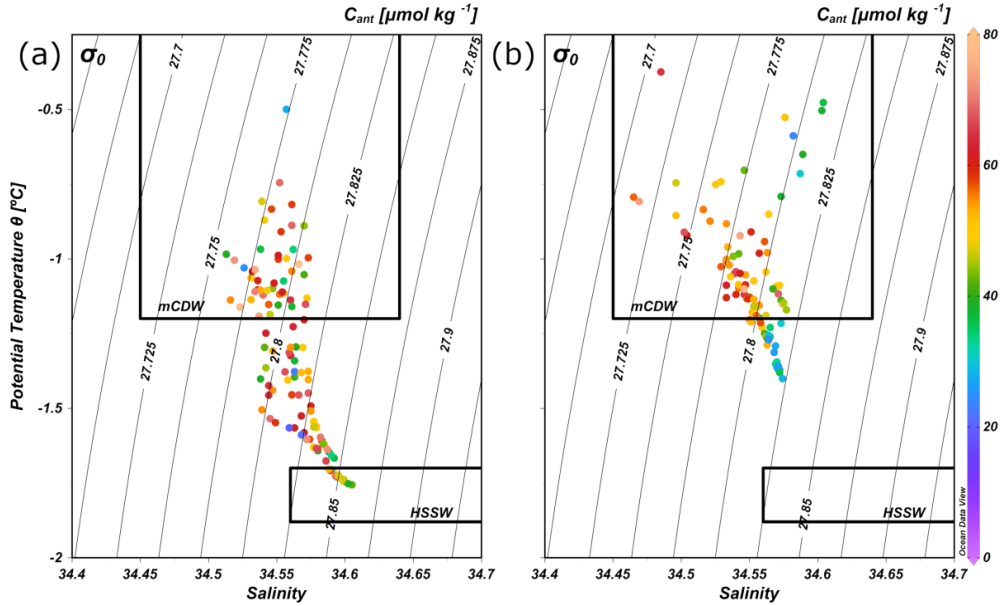


Figure 17: θ -S-C_{ant} diagram for the central (a) and eastern (b) basins of the Bransfield Strait. High Salinity Shelf Water (HSSW) and modified Circumpolar Deep Water (mCDW) indices followed the definitions proposed by Carmack [1974] and Robertson et al. [2002]. The gray lines mark the potential density (kg m^{-3}) isolines in relation to the surface.

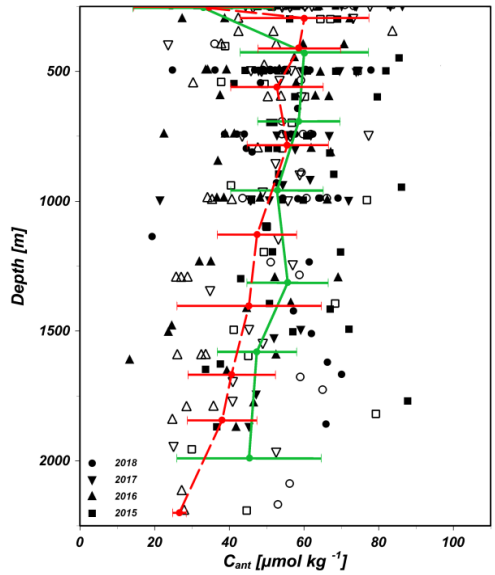


Figure 18: Vertical concentration (in $\mu\text{mol kg}^{-1}$) of C_{ant} in the Bransfield Strait. The symbols depict each year in which the samples were collected (squares, triangles, inverted triangles and dots for the years 2015, 2016, 2017 and 2018, respectively), while the symbols indicate the data per basin (solid symbols for the central basin and open for the eastern basin). The lines indicate the averaged concentration of all years with standard deviations (green lines for the central basin and red lines for the eastern basin).

5.4.2.2 Interannual variability in pH and saturation state distribution

Across the analyzed years, the pH distribution in the Bransfield Strait responds to the strength of the inputs of shelf water from the Weddell Sea or the western basin of the Bransfield Strait, which have high mCDW percentages and are also more (less) acidic due to the cold (warm) water. When the HSSW input drives the Bransfield Strait hydrography, the pH_{total} distribution is more constant at the surface and intermediate layers, as observed in 2015 (Figures 19a, S3) and 2017 (Figures 19c, S9). In these years, the pH_{total} variations are less marked than those in 2016 (Figures 19b, S6) and 2018 (Figures 19d, S12), where less acidic water inputs are notorious over the Deception Island side and over the surface layer, indicating an important input from the western basin of the Bransfield Strait (Figure S12).

As the surface layer had high mCDW inputs from the western basin of the Bransfield Strait, the warm temperature slightly increased the $\Omega_{\text{Aragonite}}$. However, in general, $\Omega_{\text{Aragonite}}$ is undersaturated at shallow depths (~60 m in 2015 and 2017; and variable in 2016 and 2018). The deepening of the aragonite saturation horizon in 2018 is interesting (Figure 19d), which likely indicates a possible increased input of mCDW from the western basin of the Bransfield Strait to the southern extreme of the strait, which is surrounded by water with low pH and $\Omega_{\text{Aragonite}}$. In the middle of the strait, another decrease in the aragonite saturation horizon is observed, which can indicate an incoming flux passing through the South Shetland Islands passages (Figure S12). In the intermediate and deep layers of the Bransfield Strait, the pH distributions fairly coincide with the C_{ant} distributions in 2015 (Figure 20a), 2016 (Figure 20b) and 2018 (Figure 20d). The pathway in which the HSSW with high C_{ant} enters the Bransfield Strait varies

interannually, and the pH decreases when the C_{ant} concentration increases (Figure 20a, 20d). As the mCDW had low C_{ant} values and high pH, its input from the southwestern side decreased the C_{ant} concentration and increased the pH inside the Bransfield Strait. As the aragonite saturation horizon occurred at the surface, the depth of the $\Omega_{\text{Calcite}} = 1.2$ isoline varied according to the strength of the inputs, and it was on average near 1500 m, reaching 700 m in 2015 (Figure 20a).

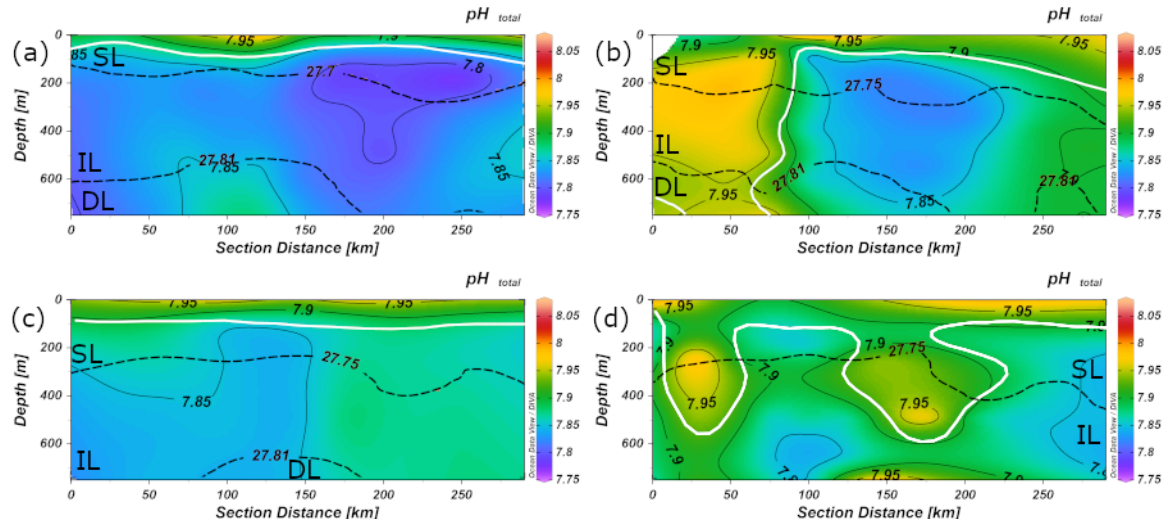


Figure 19: Vertical profiles of pH_{total} in the Bransfield Strait across the L section in the years of 2015 (a), 2016 (b), 2017 (c) and 2018 (d) over the surface and intermediate layers (up to 750 m). The left sides of the images are oriented near Deception Island, and the right sides coincide with Elephant Island. The thin black contours represent the pH_{total} isolines; the dashed black contours represent the limits of the layers, with the surface (SL) and intermediate (IL) layers separated by the 27.75 kg m^{-3} isopycnal and intermediate and deep (DL) layers separated by the 27.81 kg m^{-3} isopycnal. The white lines indicate the saturation horizon for aragonite ($\Omega_{\text{Aragonite}} = 1$).

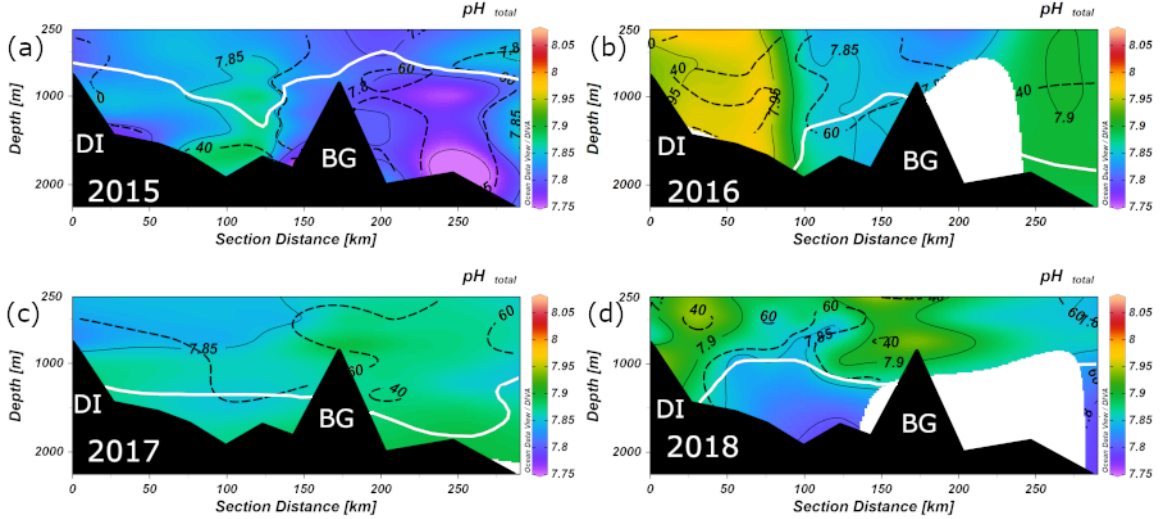


Figure 20: Vertical profiles of pH_{total} across the L section in the Bransfield Strait in the years of 2015 (a), 2016 (b), 2017 (c) and 2018 (d) over the deep layer (from 750 m to bottom). The central basin of the Bransfield Strait is located between Deception Island (DI) and the Bridgeman Guyot (BG), while the eastern basin is located northeast of the BG (right side of the images). The thin black contours are the pH_{total} isolines; the thick black contours are the isolines of $C_{\text{ant}} = 60 \mu\text{mol kg}^{-1}$, and the white lines are the isolines of $\Omega_{\text{Calcite}} = 1.2$.

The highest pH values (Figure 21) are observed in the surface layer (7.91 ± 0.07 in the central basin and 7.9 ± 0.05 in the eastern basin), decreasing to the intermediate layer and maintaining an averaged value in both basins (7.87 ± 0.03). In the deep layers of the Bransfield Strait, a lower pH is observed in the eastern basin (7.86 ± 0.05) than in the central basin (7.87 ± 0.06), but similar to the C_{ant} samples, some stations were not considered in the eastern basin, which can mask the results. Despite the variability across the layers, the differences in pH across the layers are in the range of 0.01 to 0.07 pH units.

The saturation state is linked with the pH and presents the highest values at the surface (Figure 22) and decrease with depth. Ω_{Calcite} is oversaturated throughout the water columns, having values of 1.72 ± 0.36 , 1.41 ± 0.17 and 1.23 ± 0.18 in the central basin and 1.69 ± 0.24 , 1.4 ± 0.09 and 1.18 ± 0.14 in the eastern basin for the surface, intermediate and deep layers, respectively.

Conversely, $\Omega_{\text{Aragonite}}$ is saturated only in the surface layer, with a minimum depth in 2015-2017 (~60 m), and a variable depth influenced by the mCDW inputs in 2016-2018 (~800 m). Across the layers, the averaged values are 1.08 ± 0.22 , 0.89 ± 0.1 and 10.78 ± 0.06 in the central basin of the Bransfield Strait and 1.07 ± 0.2 , 0.88 ± 0.09 and 0.77 ± 0.1 in the eastern basin. The average depth of the aragonite saturation horizon is ~60 m in the central basin and ~270 m in the eastern basin of the Bransfield Strait.

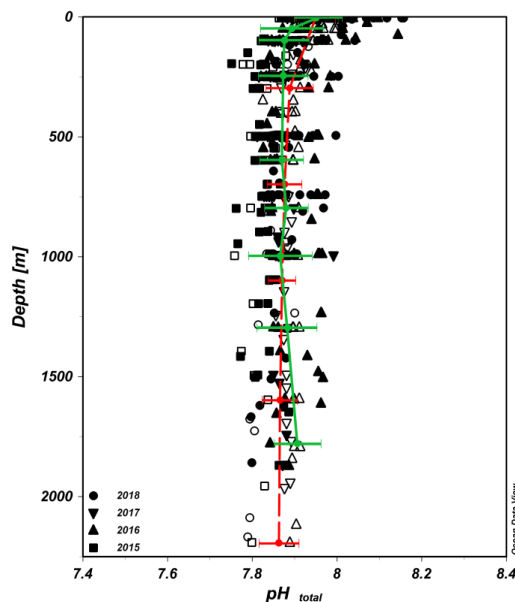


Figure 21: Vertical distribution of pH_{total} in the Bransfield Strait. The symbols depict each year in which the samples were taken (squares, triangles, inverted triangles and dots for the years 2015, 2016, 2017 and 2018, respectively), while the symbols indicate the data per basin (solid symbols for the central basin and open for the eastern basin). The lines indicate the averaged concentration of all years with standard deviations (green lines for the central basin and red lines for the eastern basin).

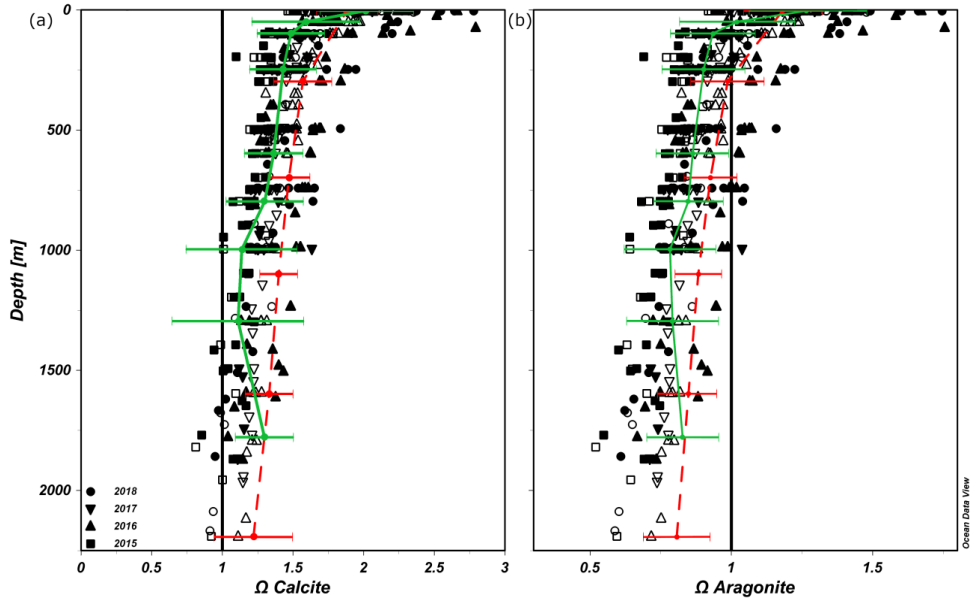


Figure 22: Vertical distribution of Ω_{Calcite} (a) and $\Omega_{\text{Aragonite}}$ (b) in the Bransfield Strait. The symbols depict each year in which the samples were taken (squares, triangles, inverted triangles and dots for the years 2015, 2016, 2017 and 2018, respectively), while the symbols indicate the data per basin (solid symbols for the central basin and open for the eastern basin). The lines indicate the averaged concentration of all years with standard deviations (green lines for the central basin and red lines for the eastern basin). The black lines indicate the calcium carbonate saturation horizon for each mineral phase ($\Omega = 1$).

5.5 Discussion

In this work, we describe the acidification state along the Bransfield Strait based on the distribution of C_{ant} , pH_{total} , Ω_{Calcite} and $\Omega_{\text{Aragonite}}$ in the summer periods of 2015-2018. According to our results, the different origins of the water masses control the acidification state, with less dense and cold water in the surface coming from the western basin of the Bransfield Strait and a colder water mass associated with the Weddell Sea. According to [Dotto et al. \[2016\]](#), the interannual variation in the climatic modes controls and modifies the strength of the inputs of water masses from the Weddell Sea continental shelves. This author also reported an important decrease in the LSSW input between 2010 and 2014, which is consistent with our observations (Figure 20a), which indicated that this input increased in only 2018.

5.5.1 Controls of the acidification state in the surface layer

The surface layer of the Bransfield Strait is associated with water from the Bellingshausen Sea, which mixed with CDW before entering the western basin of the Bransfield Strait. This process generated a type of mCDW with a higher C_T increased in this newly formed water mass [Gordon & Nowlin 1978]. The percentage of CDW that is mixed interannually varies according to the ENSO phase, as a deep mixed layer can increase the volume of this water to be mixed with the water from the Bellingshausen Sea [Conrad & Lovenduski 2015]. After mixing, this water is maintained at the top of the water column while advecting to the central and eastern basins of the Bransfield Strait along the South Shetland Islands shelf [Sangrà et al. 2011; Ruiz Barlett et al. 2018]. This situation governs the interaction with the atmosphere and controls the saturation states, which are also influenced by changes in temperature, gas solubility and possibly biological activity [Shadwick et al. 2013; Waugh, 2014; Lovenduski et al. 2018]. The variations in the aragonite saturation horizon (Figure 22b) can be generated by both variations in the biogeochemical properties of the waters advected to this area and the dynamic pumping from anticyclonic eddies, which have been recognized in the Bransfield Strait and have been determined to influence the water column to a depth of at least 300 m [Sangrà et al. 2011]. Several studies have shown that anticyclonic eddies can rapidly modify the acidification state due to the pumping of CO_2 from the surface to deeper waters [Ito et al. 2010; Moreau et al. 2017; Orselli et al. 2019]. As the surface water has less C_T than the deeper and colder water associated with the Weddell Sea, instabilities in this surface layer with high pH and saturation states (Figure 19b, 19d) can influence the carbon system below.

5.5.2 Controls on acidification state in the intermediate and deep layers

The high dissolved oxygen (Figure 13) and high salinity (Figures S1, S4, S7, S10) of the water in the deep layer of the central basin of the Bransfield Strait indicates that this basin is influenced by the HSSW from the Larsen Ice Shelf that was recently ventilated. Conversely, the eastern basin is more influenced by the LSSW associated with the farthest and old Filchner-Ronne Ice Shelf water, which is less salty and less oxygenated as it is more exposed to external water masses [Frölicher *et al.* 2015; Hellmer *et al.* 2017]. This Weddell Sea Shelf Water (both HSSW and LSSW) can accumulate a high amount of CO₂ (C_{ant}) depending on the weather settings, glaciers, and ice shelves [Tanhua *et al.* 2017]. According to the distance between the Filchner-Ronne Ice Shelf, Larsen Ice Shelf and the Bransfield Strait, a high C_{ant} is expected in the LSSW due to increased ventilation time. However, the restriction of most of the internal HSSW allows for the preservation of high C_{ant} concentrations in the central basin of the Bransfield Strait due to reduced mixing with external water masses (Figure 16c, 16d). In addition, the low temperatures of the water in the central basin induce decreases in both pH and saturation states (Figure 20b, 20d). As the eastern basin of the Bransfield Strait is influenced by water that advects at the edge of the Eastern Antarctic Peninsula to the north at a deep level, it is highly exposed to mixing with external water [Thompson & Heywood 2008; Thompson *et al.* 2009]. Due to this mixture, the differences between the C_{ant} concentrations in the intermediate and deep layers are less marked, which reduced the effect of C_{ant} on acidification in the eastern basin of the Bransfield Strait and increases pH via temperature increases.

Changes in the SAM and the westerly winds that control the Weddell Gyre [Naveira Garabato *et al.* 2016] can modify the biogeochemical parameters, carbon transport and advection routes [Lenton & Matear 2007; Lovenduski *et al.* 2007; Hauck *et al.* 2013], which are also able to greatly limit the advection of water to the Bransfield Strait [Wilson *et al.* 1999; Gordon *et al.* 2000; Dotto *et al.* 2016]. Thus, in the intermediate layer of the Bransfield Strait, the acidification state responds to the strength of the inputs from the western basin and the mixture between mCDW and Weddell Sea Shelf Water. The deep layer, which is more restricted, is predominantly controlled by (i) the interannual variations in the absorbed CO₂ (C_{ant}) concentration over the Weddell Sea continental shelves and (ii) changes in the mixture percentage. When the inputs from the Western Antarctic Peninsula domain are represented in the Bransfield Strait hydrography, the pH distribution is more constant and lower in the surface and intermediate layers than in the deep layer, and the calcite saturation horizon is shallower (Figure 20a), while increased input of mCDW results in a lower saturation horizon (Figure 20b, 20c).

5.5.3 C_{ant} in the Southern Ocean

When comparing our results with the results of studies on the anthropogenic CO₂ and acidification state in the Southern Ocean, we find that the Bransfield Strait is understudied, and this region must be compared with other regions near the Bransfield Strait, such as the Weddell Sea. Earlier works in the Weddell Sea, such as that by Anderson *et al.* [1991], estimated an averaged C_{ant} concentration of 36 µmol kg⁻¹ in the ice shelf water. Moreover, Hauck *et al.* [2010] calculated a decadal increase of between 5 and 8 µmol kg⁻¹ C_{ant} in the period from 1992 – 2008, and this study also reported a C_{ant} increase of 2 µmol kg⁻¹ in

the mCDW that enters the Weddell Sea on the northeastern side of the Weddell Gyre and is mixed with the HSSW. Over the mCDW, van Heuven *et al.* [2014] estimated an annual C_{ant} increase of $0.12 \pm 0.05 \mu\text{mol kg}^{-1}$ in the mCDW that entered the Weddell Gyre. In the Ross Sea [e.g., Sandrini *et al.* 2007] applied the TrOCA approach to estimate a C_{ant} concentration of $30 \pm 4 \mu\text{mol kg}^{-1}$ in the HSSW, which is considerably lower than our results (on average $51 \pm 13 \mu\text{mol kg}^{-1}$). As expected, the highest C_{ant} values indicate a long ventilation period in the cold shelf waters of the Weddell Sea. Our C_{ant} results are in line with those reported by Kerr *et al.* [2017a], who indicated the influence of the HSSW to the north of the Gerlache Strait and calculated an average C_{ant} concentration of $29 \pm 16 \mu\text{mol kg}^{-1}$, with values between $3 \mu\text{mol kg}^{-1}$ and $62 \mu\text{mol kg}^{-1}$ in this water mass.

5.5.4 Acidification state in the Southern Ocean

As for the C_{ant} , the comparison of the acidification state of the Bransfield Strait with the results of recent works is complicated by the lack of data in the region and because most data are from the surface. In general, our pH and carbonate saturation states in the surface layer are lower than those reported in the surface of the Ross Sea. The study by Kapsenberg *et al.* [2015] in the Ross Sea reported the highest pH and $\Omega_{\text{Aragonite}}$ values at the surface in summer, with values of 8.15 ± 0.08 pH units and $\Omega_{\text{Aragonite}} 1.68 \pm 0.3$. These saturation state values are slightly lower than those reported by DeJong *et al.* [2015] of 2.24 for Ω_{Calcite} and 1.4 for $\Omega_{\text{Aragonite}}$. Additionally, on the surface of the Ross Sea, Mattsdotter Björk *et al.* [2014] report lower pH, Ω_{Calcite} and $\Omega_{\text{Aragonite}}$ values of 7.93,

1.64 and 1.03, respectively. It is evident that those studies present higher values than those reported here.

The acidification in polar regions directly affects the food web, especially at lower levels (i.e., microbes and primary producers). As changes in the acidification state modify microbial behavior, an increase in C_{ant} can be associated with variations in primary productivity due to the role of the microbial loop in the ocean biogeochemical cycle [[Hancock et al. 2018](#)]. The rapid effect of acidification on zooplanktonic pteropods has been recognized as an important food source in the Southern Ocean. [Manno et al. \[2017\]](#) recognized the importance of these organisms due to their place in the food web, high population density and importance of carbon export to the deep ocean. Thus, ocean acidification can modify the biogeochemical cycle by influencing the microbial loop, decreasing primary production due to a lack of recycled nutrients, restricting the distribution of calcareous organisms due to a decrease in the saturation state and dissolving buried carbonates in the ocean due to the shallow carbonate compensation depth.

5.6 Summary and conclusions

We present new evidence of the processes that control the acidification state in the Bransfield Strait and the amount of C_{ant} that is being absorbed by the Weddell Sea. The acidification state of the central and eastern basins of the Bransfield Strait are described based on consecutive summer cruises from 2015 to 2018 as part of the activities executed by the NAUTILUS project. To achieve this goal, we use hydrographical and biogeochemical measurements to assess the behavior and distribution of anthropogenic CO_2 , pH_{total} and calcium carbonate saturation states. The distribution of these variables indicates that inside the

Bransfield Strait, the acidification state is controlled by the input of water with different biogeochemical and hydrographical parameters. These parameters are associated with the water from the surface layer to the western basin of the Bransfield Strait, where warmer temperatures and C_T control the pH distribution, which is also modified by the interaction with the atmosphere. In the intermediate and deep layers, the acidification state is mainly controlled by the CO_2 solubility in the cold Weddell Sea Shelf Waters; thus, the capacity to absorb C_{ant} , the ventilation time and advection route to the strait vary interannually.

Based on the TrOCA approach, we estimated an average concentration of C_{ant} in the Bransfield Strait of $51 \pm 13 \mu\text{mol kg}^{-1}$, with a higher concentration in the central basin ($53 \pm 14 \mu\text{mol kg}^{-1}$) than in the eastern basin ($49 \pm 13 \mu\text{mol kg}^{-1}$). The averaged pH was 7.89 ± 0.06 , with higher values in the surface layer (7.9 ± 0.06) than in the intermediate and deep layers (7.87 ± 0.04) without differences between basins. While Ω_{Calcite} is considered oversaturated across the analyzed years (1.71 ± 0.28 , 1.41 ± 0.14 and 1.22 ± 0.17 in surface, intermediate and deep layers, respectively), $\Omega_{\text{Aragonite}}$ is saturated in only the surface layer (1.08 ± 0.18 , 0.89 ± 0.09 and 0.78 ± 0.11 for surface, intermediate and deep layers, respectively), being undersaturated below ~ 60 m in the central basin of the Bransfield Strait and below ~ 270 m in the eastern basin.

Acknowledgments

This study contributes to the activities of the Brazilian Ocean Acidification Network (BrOA; www.broa.furg.br) and the Brazilian High Latitude Oceanography Group (GOAL). The NAUTILUS project was sponsored by the Brazilian Antarctic Program (PROANTAR). GOAL has been funded by and/or has received logistical support from the Brazilian National Council on Research and Development

(CNPq grant nos. 405869/2013-4 and 407889/2013-2), the CAPES Foundation (grant no. 23038.001421/2014-30), the Brazilian Ministry of the Environment (MMA), the Brazilian Ministry of Science, Technology, Innovation and Communication (MCTIC), and the Brazilian National Institute of Science and Technology of Cryosphere (INCT-CRIOSFERA; CNPq grant nos. 573720/2008-8 and 465680/2014-3). J. C. Torres-Lasso acknowledges CAPES grant no. 8882.158644/2017-01. R. Kerr acknowledges CNPq researcher grant nos. 302604/2015-4 and 304937/2018-5 and CAPES grant no. 88881.195000/2018-01. I. B. M. Orselli acknowledges CAPES/CMAR2 for her Ph.D. funding (CAPES process nos. 23038.001421/2014-30 and BEX 0077/17-8). J. M. Lencina-Avila acknowledges the CAPES grant nos. 88887.283965/2018-00 and 88887.362782/2019-00. The GOAL and BrOA dataset is provided by request. We also thank the Brazilian Navy, especially the officers, crew, and all researchers onboard the RV *Almirante Maximiano*, for providing logistical and sampling support during the NAUTILUS cruises.

Supplementary materials for

**INTERANNUAL VARIABILITY OF THE OCEAN ACIDIFICATION STATE AND ANTHROPOGENIC CO₂ IN THE BRANSFIELD STRAIT, NORTHERN
ANTARCTICA PENINSULA**

Juan Camilo Torres-Lasso^{1,2,*}, Rodrigo Kerr^{1,2,*}, Jannine Marquez Lencina-Avila^{1,2}, Iole Beatriz Marques Orsell^{1,2,3,4},
Mariah de Carvalho-Borges^{1,2}, Catherine Goyet^{3,4}, Mauricio M. Mata¹

¹ Laboratório de Estudos dos Oceanos e Clima, Instituto de Oceanografia, Universidade Federal do Rio Grande (FURG),
Av. Itália km 8, s/n, Rio Grande, 96203-900, RS, Brazil.

² Brazilian Ocean Acidification Network (BrOA), Av. Itália km 8, Rio Grande, 96203-900, RS, Brazil.

³ IMAGES_ESPACE-DEV, Université de Perpignan Via Domitia (UPVD), 52 ave. Paul Alduy, 66860, Perpignan, France.

⁴ ESPACE-DEV UMR UG UA UM IRD, Maison de la télédétection, 500 rue Jean-François Breton, 34093, Montpellier Cedex 5, France.

* Corresponding author:

Address: Centro de Estudos dos Oceanos e Clima (CEOCEAN), Instituto de Oceanografia – FURG, Avenida Itália km 8, s/n, Campus Carreiros, Rio Grande, RS, Brazil, 96203–900

E-mail: jucatola@gmail.com; rodrigokerr@furg.br

Phone number: +55 53 3233-6858

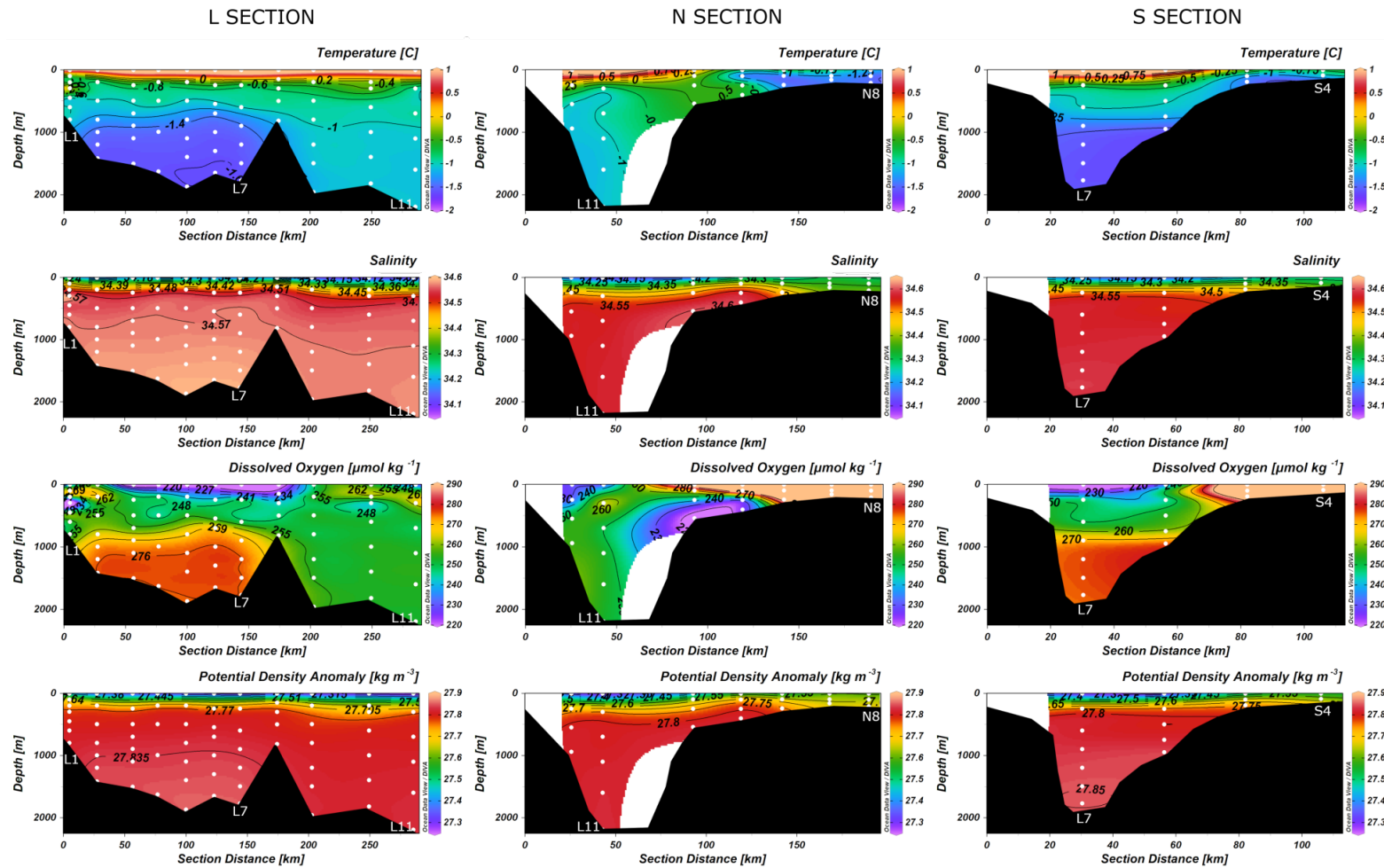


Figure S1: Profiles of hydrographical properties in 2015 across the L, N and S sections in left, center and right panels, respectively. The white dots are the places where the biogeochemical data were collected. T: temperature in $^{\circ}\text{C}$; Salinity; DO: dissolved oxygen in $\mu\text{mol kg}^{-1}$ and σ_0 : potential density anomaly in kg m^{-3} .

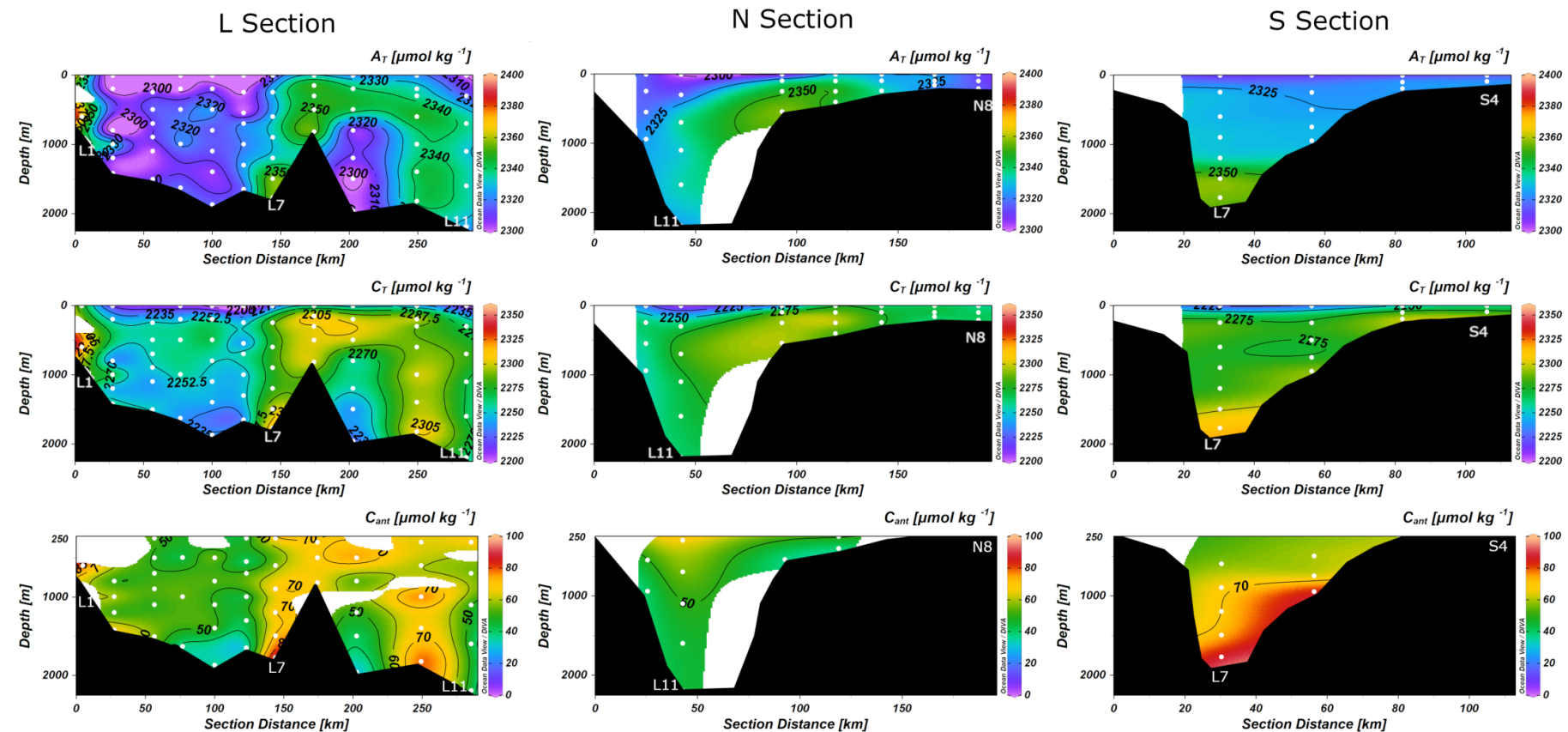


Figure S2: Profiles of carbonate system properties in 2015 across the L, N and S sections in the left, center and right panels, respectively. The white dots are the places where the biogeochemical data were collected. A_T : total alkalinity in $\mu\text{mol kg}^{-1}$; C_T : total carbon in $\mu\text{mol kg}^{-1}$ C_{ant} : anthropogenic carbon in $\mu\text{mol kg}^{-1}$.

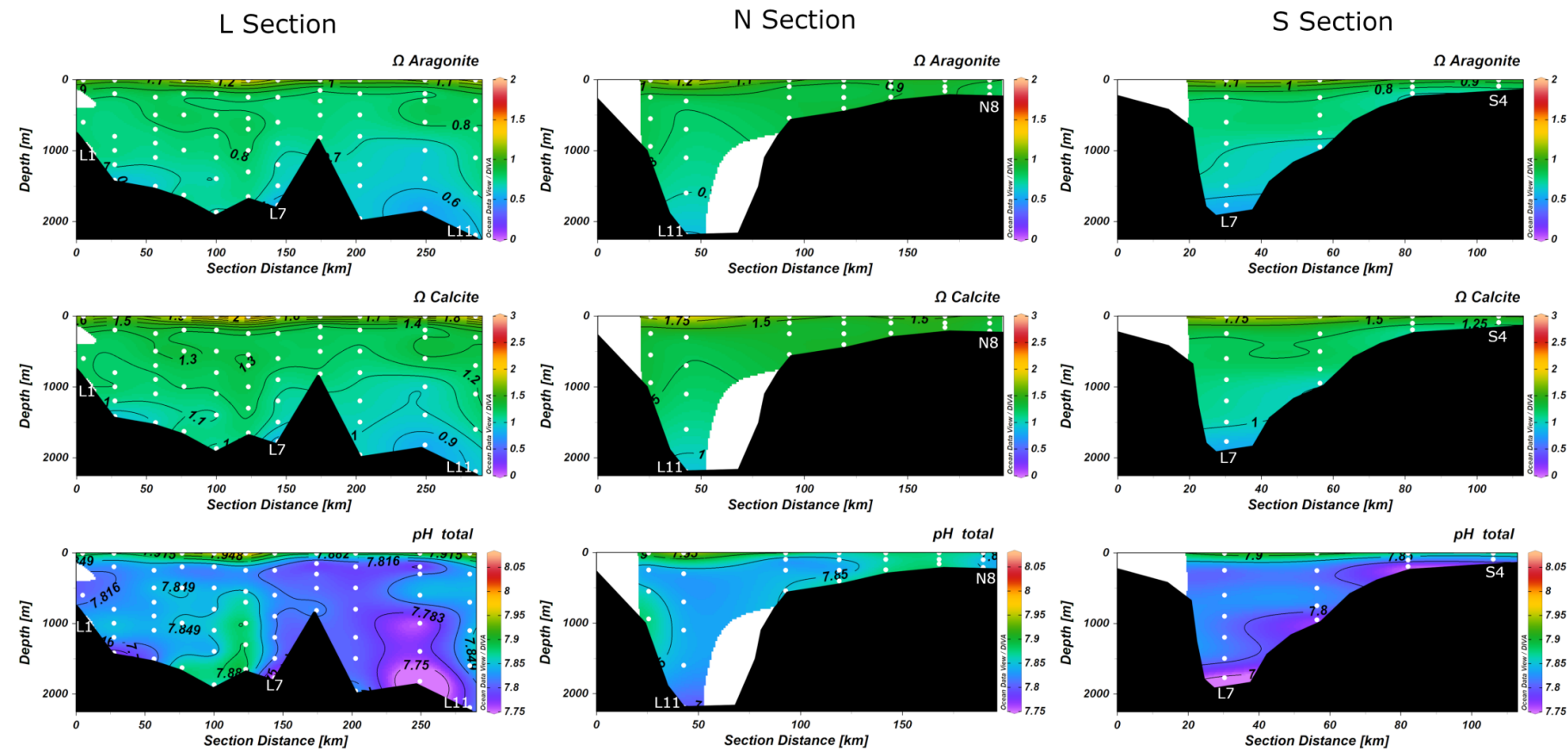


Figure S3: Profiles of carbonate system properties in 2015 across the L, N and S sections in the left, center and right panels, respectively. The white dots are the places where the biogeochemical data were collected. $\Omega_{\text{Aragonite}}$ and Ω_{Calcite} : calcite and aragonite saturation states (dimensionless); pH: in total scale.

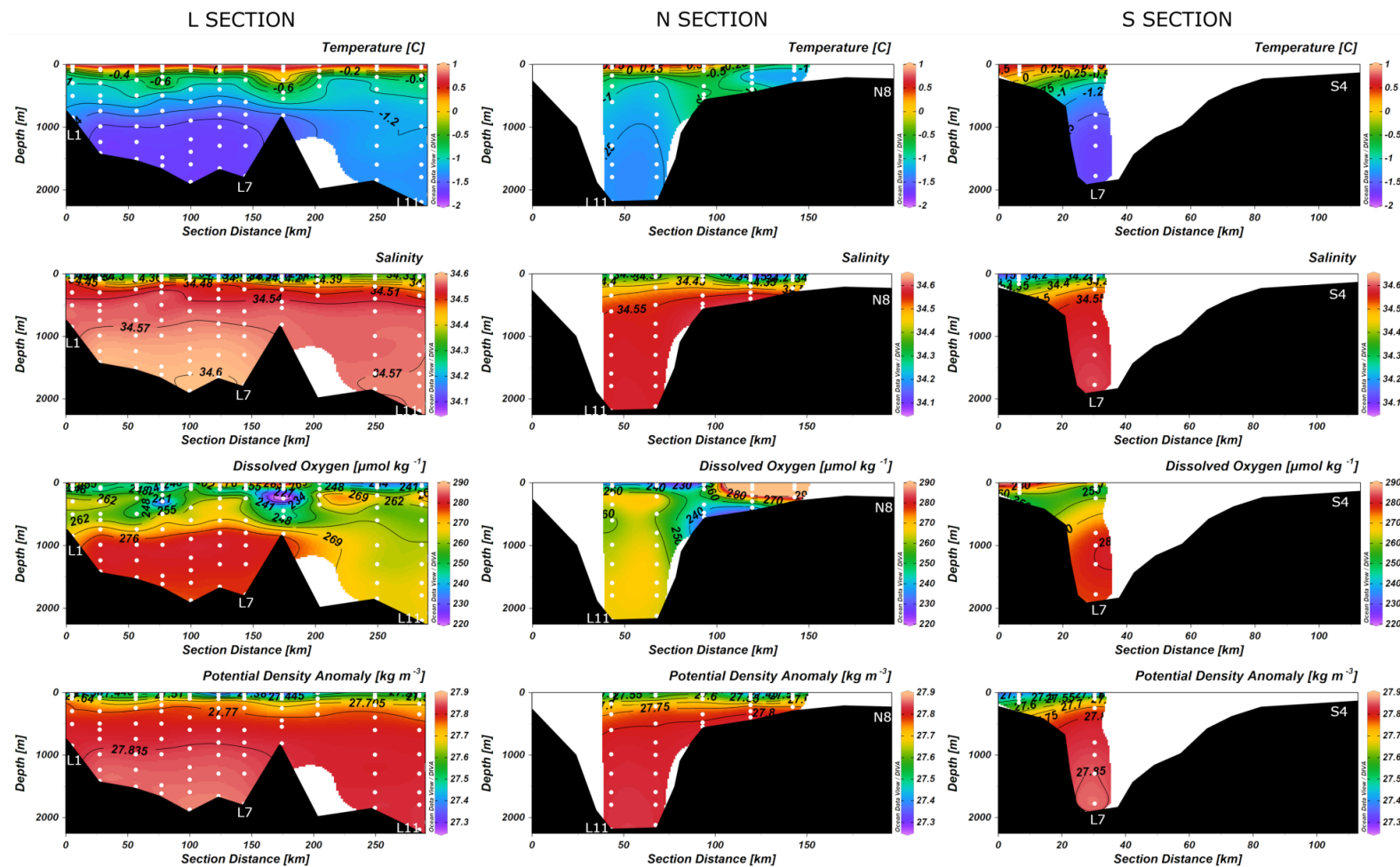


Figure S4: Profiles of hydrographical properties in 2016 across the L, N and S sections in the left, center and right panels, respectively. The white dots are the places where the biogeochemical data were collected. T: temperature in $^{\circ}\text{C}$; Salinity; DO: dissolved oxygen in $\mu\text{mol kg}^{-1}$ and σ_0 : potential density anomaly in kg m^{-3} .

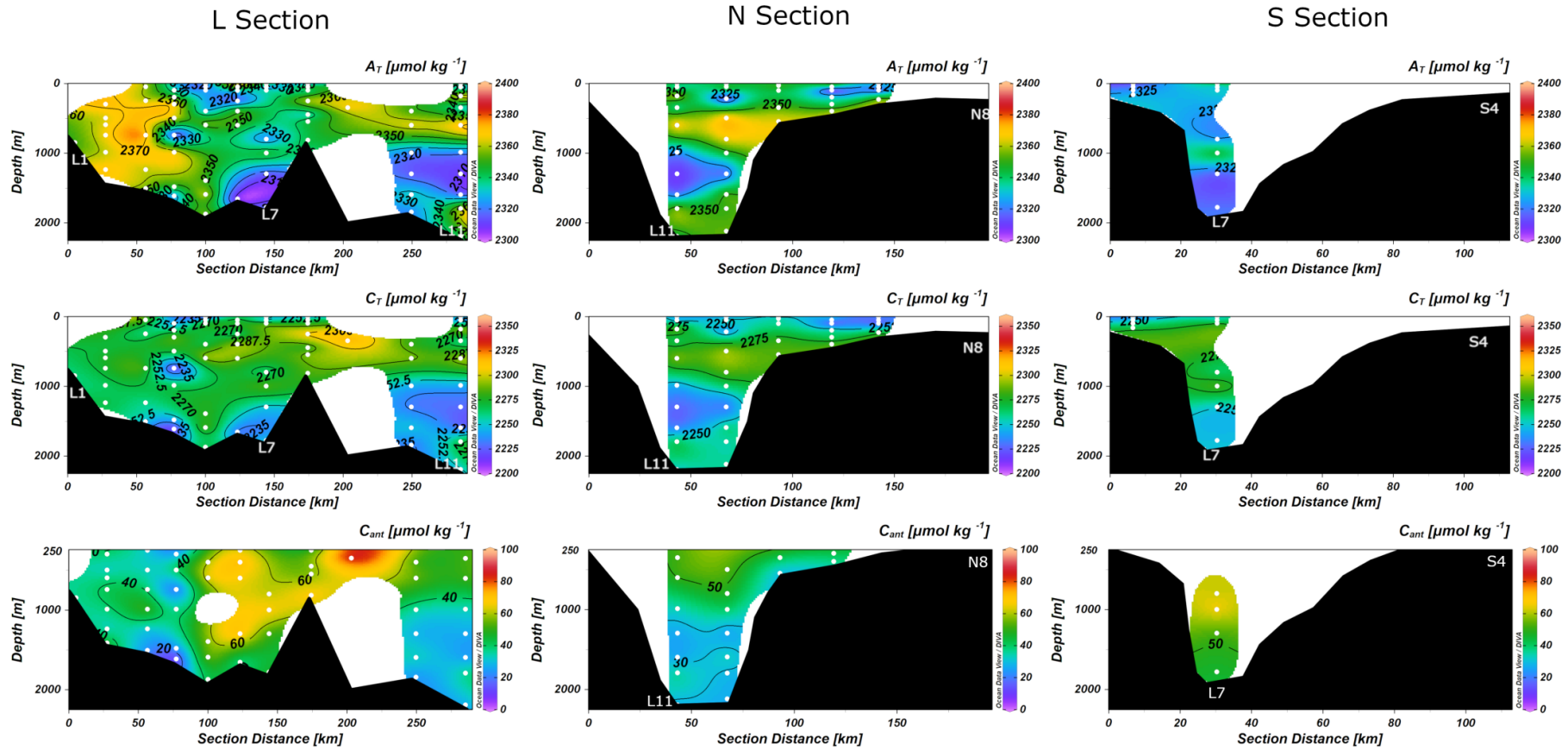


Figure S5: Profiles of carbonate system properties in 2016 across the L, N and S sections in the left, center and right panels, respectively. The white dots are the places where the biogeochemical data were collected. A_T: total alkalinity in $\mu\text{mol kg}^{-1}$; C_T: total carbon in $\mu\text{mol kg}^{-1}$ C_{ant}: anthropogenic carbon in $\mu\text{mol kg}^{-1}$.

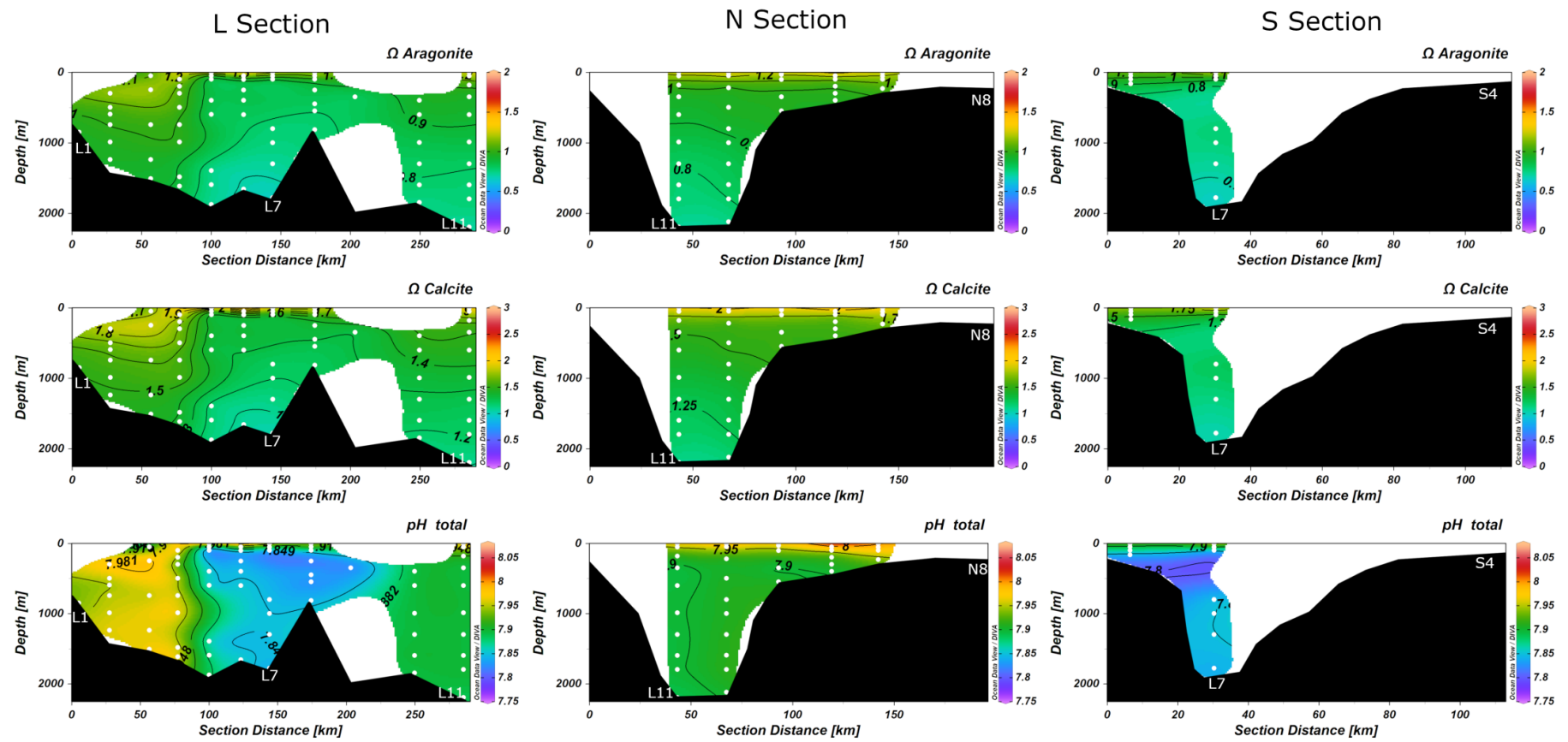


Figure S6: Profiles of carbonate system properties in 2016 across the L, N and S sections in the left, center and right panels, respectively. The white dots are the places where the biogeochemical data were collected. $\Omega_{\text{Aragonite}}$ and Ω_{Calcite} : calcite and aragonite saturation states (dimensionless); pH: in total scale.

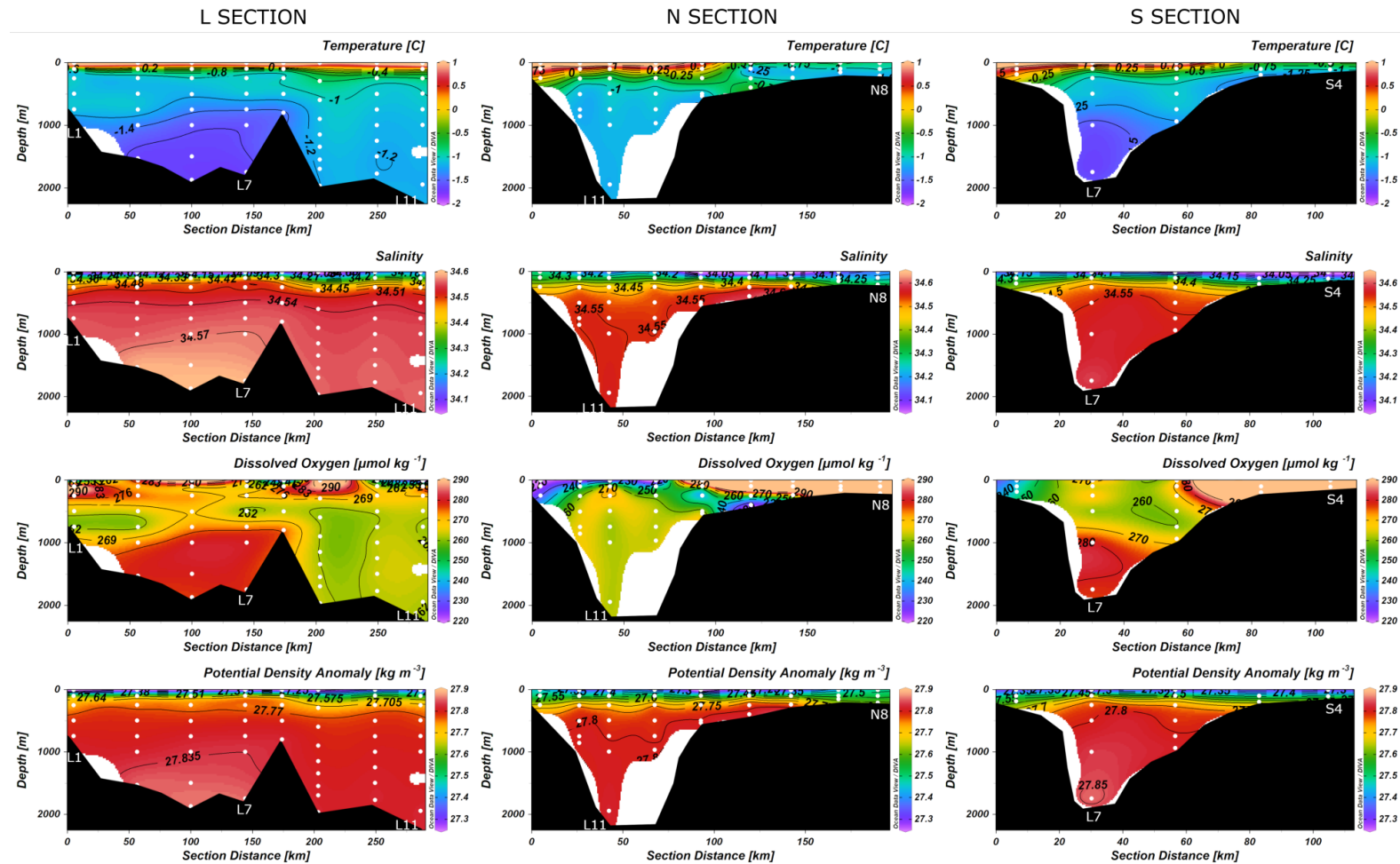


Figure S7: Profiles of hydrographical properties in 2017 across the L, N and S sections in the left, center and right panels, respectively. The white dots are the places where the biogeochemical data were collected. T: temperature in °C; Salinity; DO: dissolved oxygen in $\mu\text{mol kg}^{-1}$ and σ_0 : potential density anomaly in kg m^{-3} .

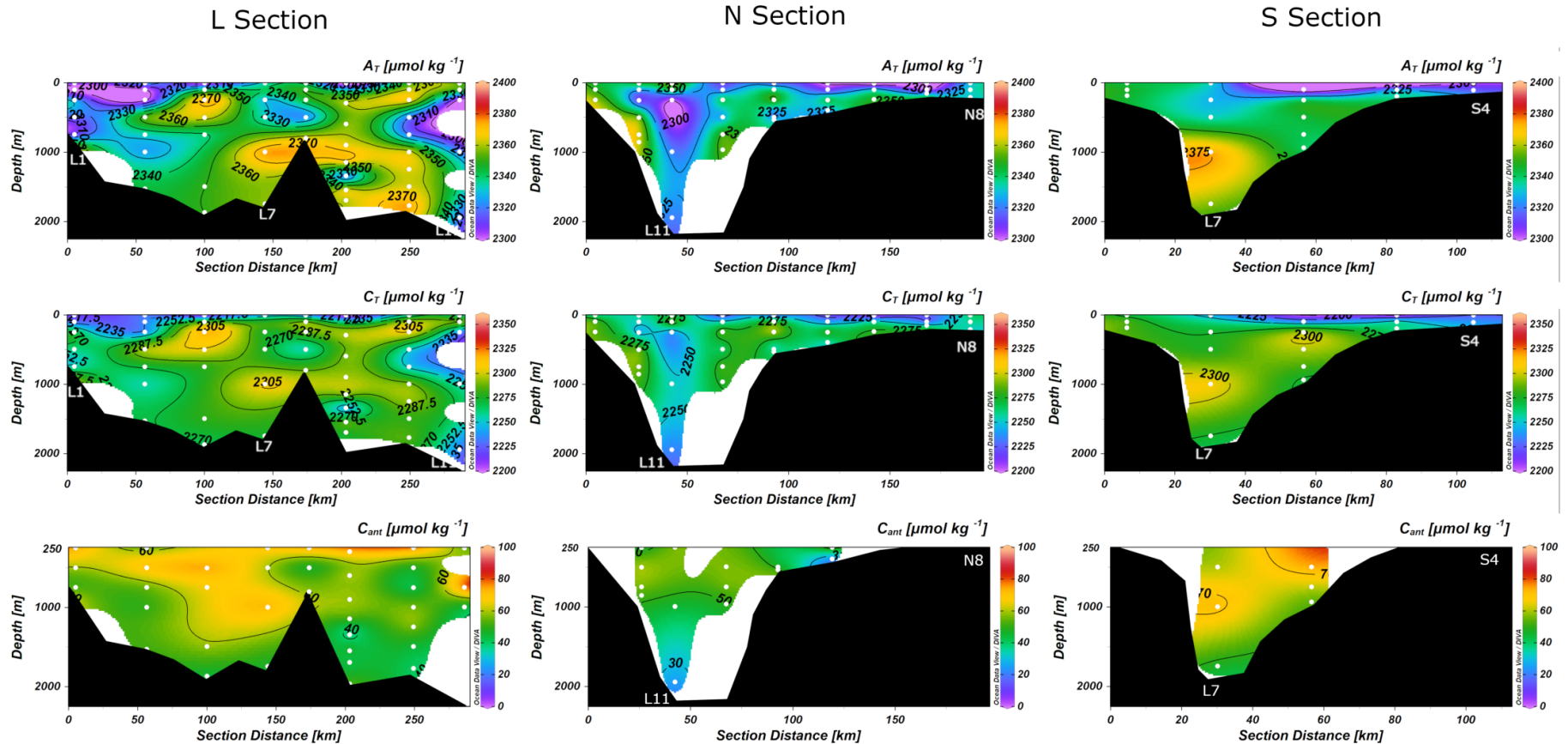


Figure S8: Profiles of carbonate system properties in 2017 across the L, N and S sections in the left, center and right panels, respectively. The white dots are the places where the biogeochemical data were collected. A_T : total alkalinity in $\mu\text{mol kg}^{-1}$; C_T : total carbon in $\mu\text{mol kg}^{-1}$ C_{ant} : anthropogenic carbon in $\mu\text{mol kg}^{-1}$.

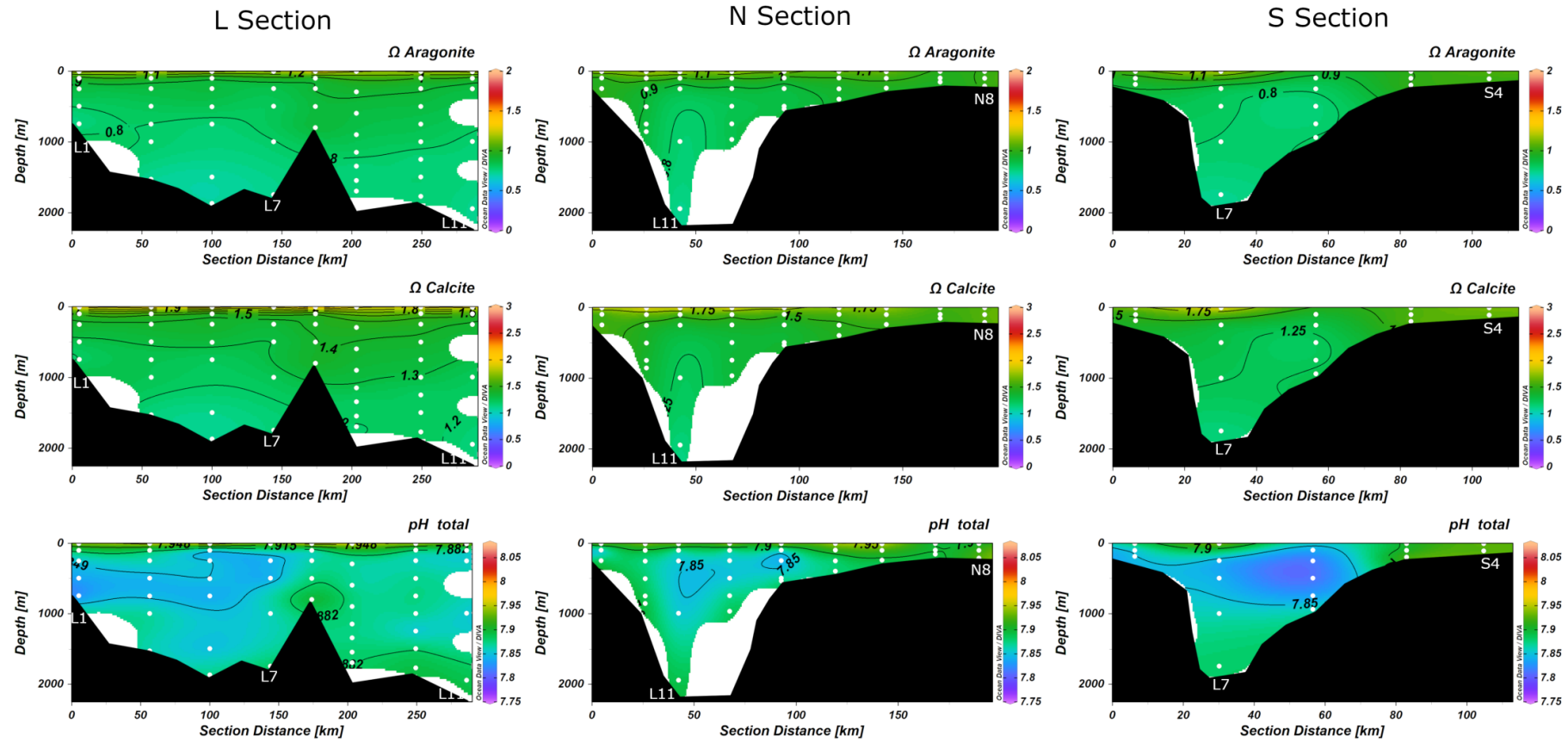


Figure S9: Profiles of carbonate system properties in 2017 across the L, N and S sections in the left, center and right panels, respectively. The white dots are the places where the biogeochemical data were collected. $\Omega_{\text{Aragonite}}$ and Ω_{Calcite} : calcite and aragonite saturation states (dimensionless); pH: in total scale.

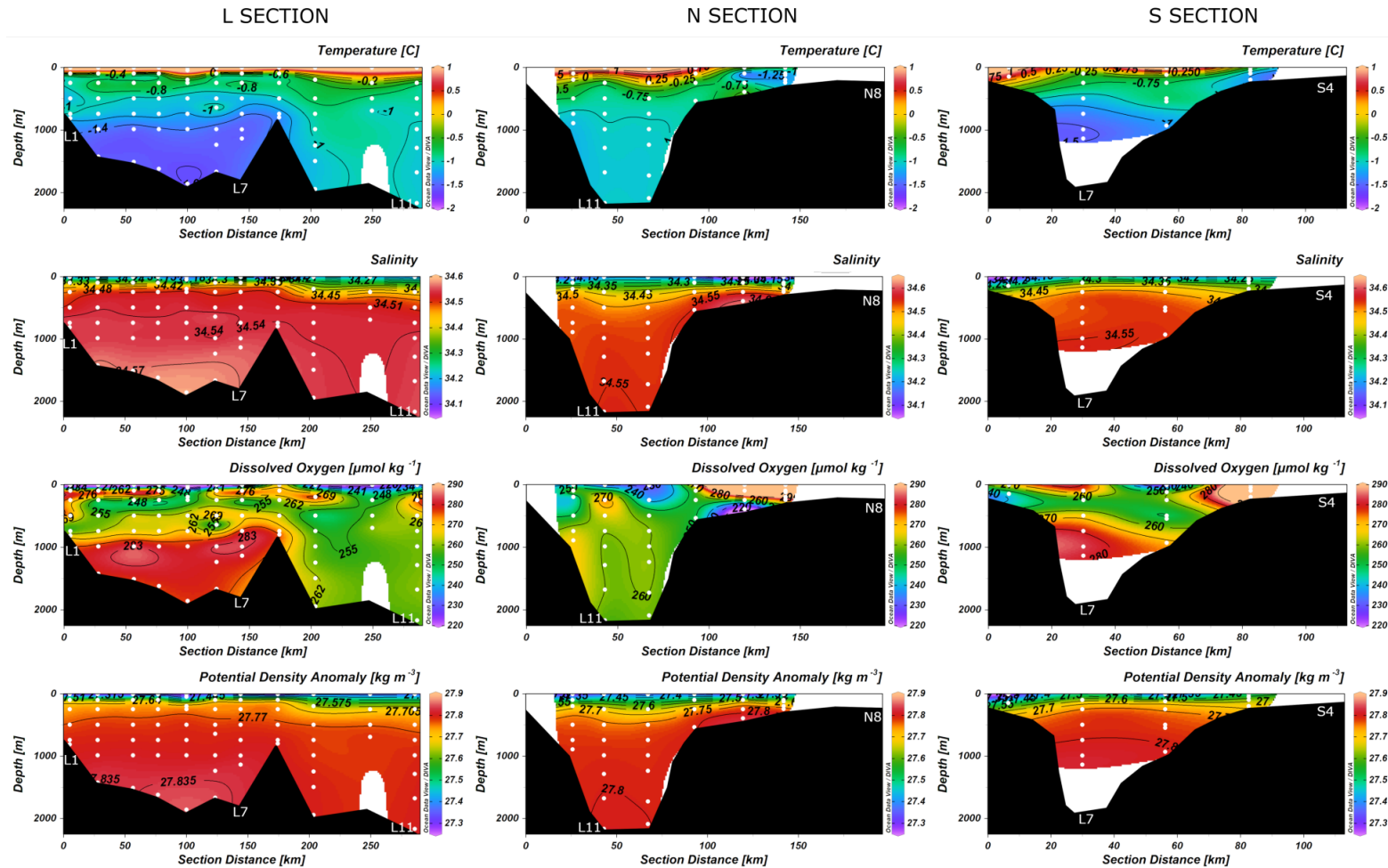


Figure S10: Profiles of hydrographical properties in 2018 across the L, N and S sections in the left, center and right panels, respectively. The white dots are the places where the biogeochemical data were collected. T: temperature in $^{\circ}\text{C}$; Salinity; DO: dissolved oxygen in $\mu\text{mol kg}^{-1}$ and σ_0 : potential density anomaly in kg m^{-3} .

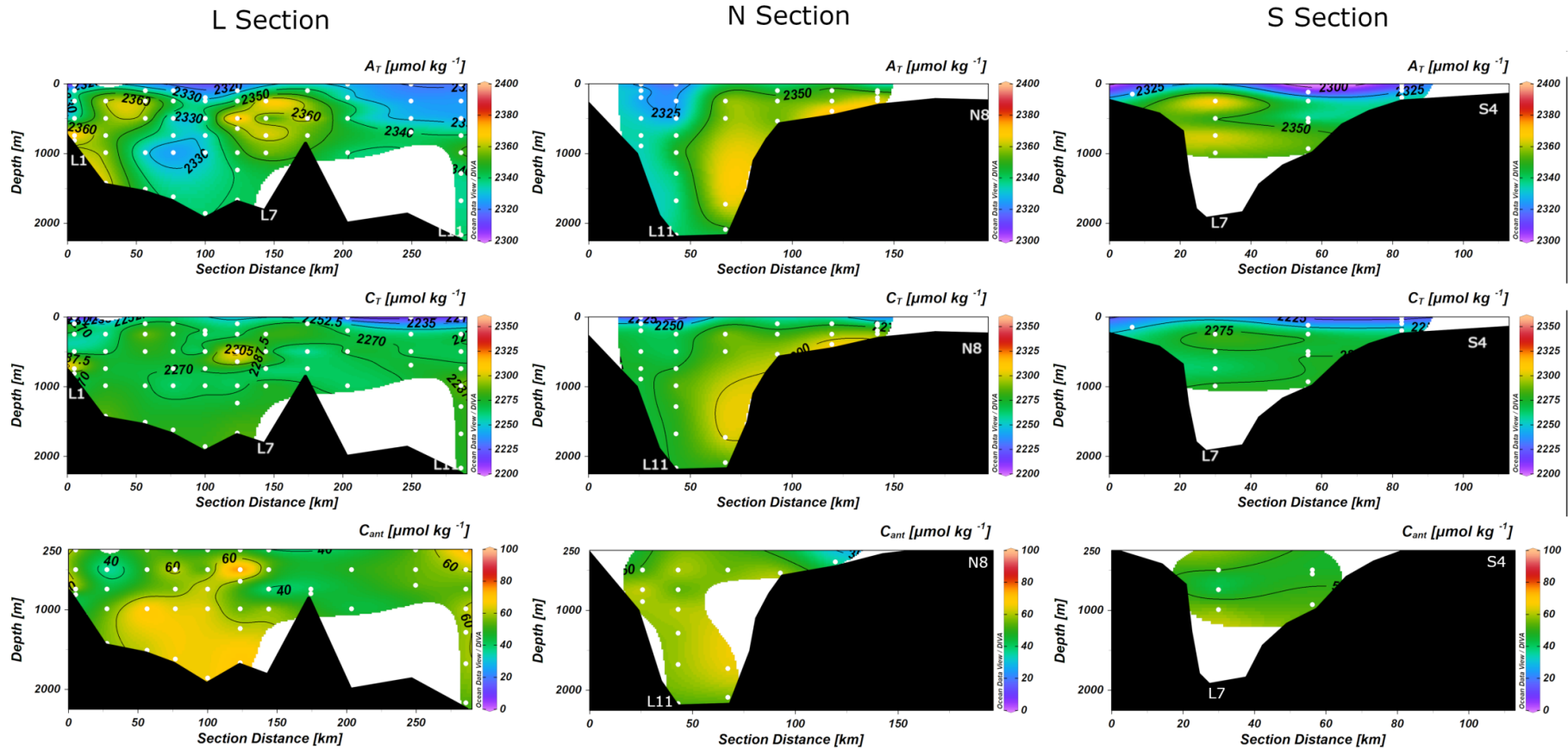


Figure S11: Profiles of carbonate system properties in 2018 across the L, N and S sections in the left, center and right panels, respectively. The white dots are the places where the biogeochemical data were collected. A_T : total alkalinity in $\mu\text{mol kg}^{-1}$; C_T : total carbon in $\mu\text{mol kg}^{-1}$ C_{ant} : anthropogenic carbon in $\mu\text{mol kg}^{-1}$.

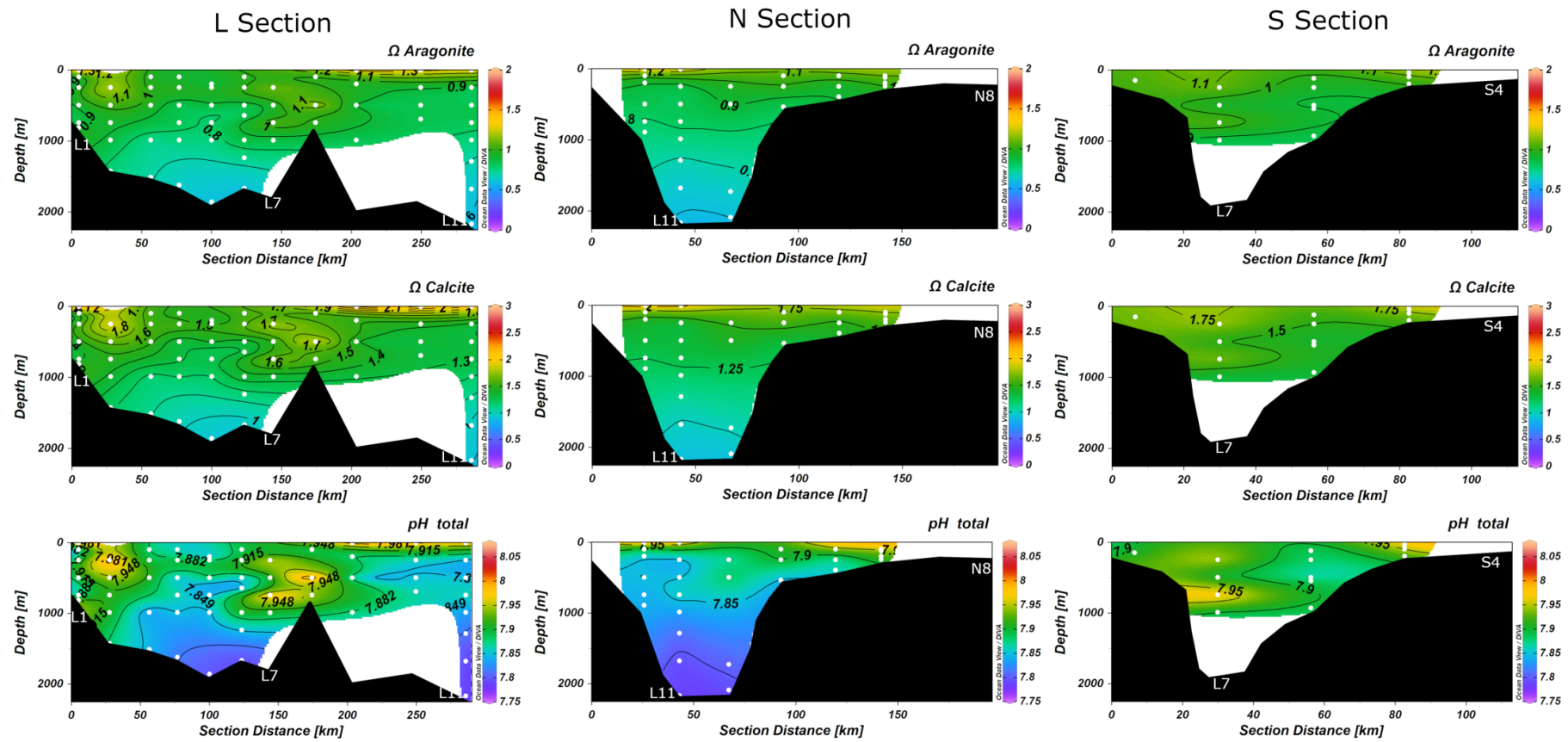


Figure S12: Profiles of carbonate system properties in 2018 across the L, N and S sections in the left, center and right panels, respectively. The white dots are the places where the biogeochemical data were collected. $\Omega_{\text{Aragonite}}$ and Ω_{Calcite} : calcite and aragonite saturation states (dimensionless); pH: in total scale.

Table S1: Averages of the hydrographical properties in the Bransfield Strait separated by basins (central and eastern) and layers (surface between 0 and 250 m; intermediate between 250 and 750 m and deep above 750 m). The number of oceanographic stations occupied and discrete samples analyzed in this work were 20, 16, 26, and 19 stations and 93, 112, 114, 111 discrete samples for the years 2015, 2016, 2017 and 2018, respectively. T: temperature in °C; Salinity; DO: dissolved oxygen in $\mu\text{mol kg}^{-1}$ and σ_0 : potential density anomaly in kg m^{-3} .

		Central basin			Eastern basin		
		Surface	Intermediate	Deep	Surface	Intermediate	Deep
2015	T	0.15 ± 0.06	-0.98 ± 0.13	-1.51 ± 0.06	0.15 ± 0.02	-0.78 ± 0.02	-1.07 ± 0.03
	S	34.34 ± 0.01	34.56 ± 0.01	34.58 ± 0.01	34.29 ± 0.04	34.55 ± 0.03	34.57 ± 0.01
	DO	256 ± 2	252 ± 8	274.0 ± 3	269 ± 1	245 ± 8	254 ± 1
	σ_0	27.6 ± 0.02	27.8 ± 0.01	27.8 ± 0.02	27.5 ± 0.05	27.8 ± 0.01	27.8 ± 0.01
2016	T	0.25 ± 0.01	-1.13 ± 0.17	-1.616 ± 0.01	-0.07 ± 0.07	-0.9 ± 0.02	-1.27 ± 0.02
	S	34.31 ± 0.02	34.54 ± 0.02	34.58 ± 0.01	34.33 ± 0.09	34.54 ± 0.01	34.57 ± 0.01
	DO	261 ± 1	265 ± 1	278.7 ± 1	267 ± 2	253 ± 3	265 ± 2
	σ_0	27.5 ± 0.01	27.8 ± 0.02	27.9 ± 0.01	27.6 ± 0.01	27.8 ± 0.01	27.8 ± 0.01
2017	T	0.07 ± 0.17	-1.11 ± 0.07	-1.52 ± 0.05	0.28 ± 0.01	-0.98 ± 0.05	-1.16 ± 0.01
	S	34.26 ± 0.03	34.54 ± 0.01	34.58 ± 0.01	34.23 ± 0.01	34.53 ± 0.01	34.56 ± 0.01
	DO	281 ± 2	263 ± 3	276 ± 2	278 ± 3	262 ± 5	263 ± 1
	σ_0	27.5 ± 0.05	27.8 ± 0.01	27.8 ± 0.01	27.5 ± 0.02	27.8 ± 0.01	27.8 ± 0.01
2018	T	0.09 ± 0.22	-1.07 ± 0.12	-1.46 ± 0.02	0.11 ± 0.08	-0.91 ± 0.02	-1.06 ± 0.06
	S	34.33 ± 0.01	34.54 ± 0.01	34.55 ± 0.01	34.30 ± 0.02	34.53 ± 0.01	34.54 ± 0.01
	DO	261 ± 4	264 ± 5	279 ± 2	268 ± 20	256 ± 7	261 ± 3
	σ_0	27.7 ± 0.01	27.8 ± 0.01	27.8 ± 0.01	27.5 ± 0.01	27.8 ± 0.01	27.8 ± 0.02

Table S2: Averages of the carbonate system properties in the Bransfield Strait separated by basins (central and eastern) and layers (surface between 0–250 m; intermediate between 250 and 750 m and deep above 750 m). A_T : total alkalinity in $\mu\text{mol kg}^{-1}$; C_T : total carbon in $\mu\text{mol kg}^{-1}$; pH: in total scale; Ω_{Calcite} and $\Omega_{\text{Aragonite}}$: calcite and aragonite saturation states (dimensionless); C_{ant} : anthropogenic carbon in $\mu\text{mol kg}^{-1}$.

		Central basin			Eastern basin		
		Surface	Intermediate	Deep	Surface	Intermediate	Deep
2015	A_T	2314 ± 1	2328 ± 1	2331 ± 3	2325 ± 2	2338 ± 4	2327 ± 1
	C_T	2253 ± 8	2275 ± 2	2276 ± 6	2263 ± 1	2286 ± 2	2268 ± 1
	pH	7.86 ± 0.01	7.83 ± 0.01	7.81 ± 0.01	7.87 ± 0.03	7.83 ± 0.01	7.82 ± 0.01
	Ω_{Calcite}	1.51 ± 0.04	1.25 ± 0.01	1.08 ± 0.01	1.54 ± 0.10	1.30 ± 0.01	1.08 ± 0.04
	$\Omega_{\text{Aragonite}}$	0.95 ± 0.02	0.79 ± 0.01	0.68 ± 0.01	0.97 ± 0.07	0.82 ± 0.01	0.69 ± 0.02
	C_{ant}	58 ± 8		66 ± 3	58 ± 4		50 ± 9
2016	A_T	2333 ± 2	2339 ± 1	2335 ± 4	2340 ± 2	2354 ± 1	2335 ± 3
	C_T	2261 ± 2	2270 ± 1	2261 ± 2	2257 ± 5	2284 ± 2	2249 ± 1
	pH	7.90 ± 0.01	7.88 ± 0.04	7.88 ± 0.03	7.94 ± 0.02	7.88 ± 0.02	7.9 ± 0.01
	Ω_{Calcite}	1.66 ± 0.03	1.37 ± 0.13	1.23 ± 0.07	1.78 ± 0.04	1.46 ± 0.05	1.26 ± 0.02
	$\Omega_{\text{Aragonite}}$	1.04 ± 0.02	0.87 ± 0.08	0.79 ± 0.04	1.12 ± 0.03	0.92 ± 0.03	0.81 ± 0.01
	C_{ant}	54 ± 11		50 ± 5	51 ± 3		33 ± 4
2017	A_T	2324 ± 2	2337 ± 8	2355 ± 2	2337 ± 4	2331 ± 3	2346 ± 1
	C_T	2254 ± 3	2280 ± 6	2279 ± 1	2261 ± 1	2266 ± 5	2269 ± 1
	pH	7.89 ± 0.01	7.84 ± 0.01	7.88 ± 0.02	7.91 ± 0.01	7.88 ± 0.01	7.88 ± 0.01
	Ω_{Calcite}	1.60 ± 0.07	1.27 ± 0.02	1.24 ± 0.08	1.69 ± 0.05	1.39 ± 0.01	1.25 ± 0.04
	$\Omega_{\text{Aragonite}}$	1.00 ± 0.04	0.80 ± 0.01	0.79 ± 0.05	1.06 ± 0.03	0.88 ± 0.01	0.80 ± 0.03
	C_{ant}	63 ± 1		55 ± 1	53 ± 1		45 ± 2
2018	A_T	2334 ± 3	2349 ± 2	2349 ± 8	2335 ± 6	2344 ± 2	2343 ± 4
	C_T	2256 ± 1	2273 ± 7	2276 ± 4	2255 ± 2	2275 ± 6	2280 ± 2
	pH	7.92 ± 0.01	7.95 ± 0.01	7.88 ± 0.03	7.92 ± 0.01	7.88 ± 0.03	7.83 ± 0.01
	Ω_{Calcite}	1.65 ± 0.05	1.48 ± 0.03	1.27 ± 0.19	1.71 ± 0.08	1.39 ± 0.09	1.08 ± 0.03
	$\Omega_{\text{Aragonite}}$	1.04 ± 0.03	0.94 ± 0.02	0.81 ± 0.07	1.07 ± 0.05	0.88 ± 0.05	0.67 ± 0.02
	C_{ant}	49 ± 5		58 ± 2	51 ± 2		57 ± 3

Capítulo VI: Síntese da Discussão e Conclusões

Neste trabalho foi descrito o estado de acidificação ao longo das bacias central e leste do estreito de Bransfield com base na distribuição de C_{ant} , pH_{total} , $\Omega_{Calcita}$ e $\Omega_{Aragonita}$ nos períodos de verão de 2015-2018, apresentando novas evidências dos processos que controlam o estado de acidificação, junto à concentração interanual de carbono antropogênico (C_{ant}) que está sendo absorvido pelas massas de água do mar de Weddell e advectadas para o estreito de Bransfield. Nele, as massas de água de diferentes origens controlam o estado de acidificação da água do mar. Na superfície, este controle é regulado pelas águas que possuem, relativamente, maior temperatura provenientes de modificações na bacia oeste do estreito de Bransfield. Por outro lado, as águas de menor temperatura, associadas ao mar de Weddell, controlam as modificações nas camadas intermediária e profunda.

A camada superficial do estreito de Bransfield está associada com à água do mar de Bellingshausen que foi misturada com Água Circumpolar Profunda antes de entrar na bacia oeste do estreito [Sangrà *et al.* 2011, Ruiz Barlett *et al.* 2018], gerando uma água com maior C_T e temperatura do que as águas do mar de Bellingshausen [Gordon & Nowlin 1978]. A porcentagem de Água Circumpolar Profunda que é misturada muda interanualmente de acordo com a fase ENSO, onde uma camada de mistura mais profunda pode aumentar o volume a ser misturado com as águas do mar de Bellingshausen [Conrad & Lovenduski 2015], controlando o estado de acidificação e a interação oceano atmosfera devido a sua temperatura e o efeito dela na solubilidade do CO₂, modificando o gradiente da interação e gerando o aumento no pH e no estado de saturação [Shadwick *et al.* 2015, Lovenduski *et al.* 2018]. Nesta camada superficial são observados os maiores valores de pH ($7,91 \pm 0,07$ na bacia central e $7,9 \pm 0,05$ na bacia leste), diminuindo para a camada intermediária e mantendo um valor médio nas duas bacias ($7,87 \pm 0,03$). O estado de saturação Ω_{Calcita} é supersaturada em toda a coluna de água, porém, $\Omega_{\text{Aragonita}}$ somente é saturada na camada superficial, com uma profundidade mínima em 2015 e 2017 (~ 60 m). De acordo com as entradas da Água Circumpolar Profunda modificada, a profundidade do horizonte de saturação varia nos anos de 2016 e 2018 (~ 800 m), tendo uma profundidade média do horizonte de saturação da aragonita de ~ 60 m na bacia central e ~ 270 m na bacia leste do estreito de Bransfield.

Nas camadas intermediária e profunda do estreito de Bransfield, as variações no estado de acidificação estão influenciadas pelas mudanças do SAM e nos ventos de oeste que controlam o giro de Weddell [Naveira Garabato *et al.* 2016]. Como as massas de água da plataforma continental do mar de Weddell

podem acumular uma alta quantidade de CO₂ dependendo das condições climáticas, formação e derretimento de gelo [Tanhua *et al.* 2017], o SAM pode influenciar a absorção de CO₂, seu transporte e rotas de advecção [Lenton & Matear 2007, Lovenduski *et al.* 2007, Hauck *et al.* 2013]. Além disso, variações interanuais no modo climático influenciam a percentagem de mistura das massas de água da plataforma continental do mar de Weddell que são advectadas para o estreito de Bransfield [Dotto *et al.* 2016, Naveira Garabato *et al.* 2016, van Caspel *et al.* 2018].

Na camada intermediaria, é considerado que o estado de acidificação é controlado pelos processos advectivos e a mistura das massas de água da plataforma do mar de Weddell com as massas de águas entrando desde a bacia oeste e apresentando menor pH quando a contribuição desde o mar de Weddell é maior, tendo horizontes de saturação mais rasos. Como a Água Circumpolar Profunda modificada tem valores de pH mais altos, a maior entrada desta desde a bacia oeste aumenta o pH e afunda os horizontes de saturação.

Ao incrementar a densidade ao descer para a camada profunda, considera-se que a bacia central está sob a influência da Água de Plataforma de Alta Salinidade, recentemente ventilada na Plataforma de gelo Larsen, com uma menor temperatura na água que induz a diminuição dos estados de saturação e pH. Além disso, a restrição geográfica da bacia central permite a preservação de maiores concentrações de C_{ant}, devido à menor mistura com massas de água externas. Como a bacia leste é mais influenciada pela Água de Plataforma de Baixa Salinidade associada à Plataforma de gelo Filchner-Ronne, a maior mistura na adveção destas águas desde o sul do mar de Weddell diminui a

concentração final de C_{ant} medida no estreito e aumenta ligeiramente a temperatura e tendo pH e estados de saturação maiores.

Nas camadas intermediária e profunda, o C_{ant} foi, em média, maior durante 2015 em comparação com os outros anos, tendo uma concentração média estimada em 58 µmol kg⁻¹ C_{ant}, ligeiramente maior que os valores de ~ 54 µmol kg⁻¹ C_{ant} observados para 2017 e 2018. Durante 2016, a menor concentração de 47 µmol kg⁻¹ C_{ant} pode estar influenciada pela menor quantidade de amostras obtidas na camada profunda da bacia oriental. Em geral, a bacia central tem uma maior concentração de C_{ant} que a bacia leste sob os 500 m, apresentando em média um desvio padrão que muda entre 3 - 16 µmol kg⁻¹ C_{ant}. Na camada intermediaria, as distribuições de pH coincidem com as distribuições C_{ant} em 2015, 2016 e 2018, enquanto na camada profunda, observa-se um pH mais baixo na bacia oriental ($7,86 \pm 0,05$) do que na bacia central ($7,87 \pm 0,06$). Apesar da variabilidade entre as camadas, as diferenças de pH entre as camadas estão na faixa de 0,01 a 0,07 unidades de pH.

A acidificação oceânica é acelerada pelas contribuições antropogênicas de CO₂ para a atmosfera, sendo maior a absorção desde o oceano nas regiões polares, onde são ventiladas as águas abissais do oceano global. Na medida em que o estado de acidificação altere o ecossistema pelo aumento na absorção do CO₂ nestas regiões, a diminuição no pH terá impacto nas cadeias alimentares, especialmente nos níveis mais baixos, modificando (i) o comportamento microbiano e a sua importância na reciclagem dos nutrientes inorgânicos dissolvidos ao longo da coluna de água, (ii) a especiação do Fe e a sua disponibilidade numa região de altas concentrações de nutrientes e baixas de clorofila, influenciando a produção primária e (iii) estressando o ecossistema ao

serem expostos as novas condições do ambiente. Estudar o comportamento dos oceanos polares e as rápidas variações que estão associadas à acidificação oceânica, permite entender o seu efeito nos organismos e prever os limites que o ecossistema pode suportar num ambiente cada vez mais ácido.

Capítulo VII: Referências Bibliográficas

- Anderson JB, Wellner JS, (2011) Tectonic, Climatic, and Cryospheric Evolution of the Antarctic Peninsula. American Geophysical Union.
<https://doi.org/10.1029/SP063>
- Anderson LG, Holby O, Lindegren R, Ohlson M, (1991) The transport of anthropogenic carbon dioxide into the Weddell Sea. *J. Geophys. Res.* 96, 16679. <https://doi.org/10.1029/91JC01785>
- Brown PJ, Jullion L, Landschützer P, Bakker DCE, (2015) Carbon dynamics of the Weddell Gyre, Southern Ocean. *Global Biogeochem. Cycles* 29, 288–306. <https://doi.org/10.1002/2014GB005006>. Received
- Carmack EC, (1974) A quantitative characterization of water masses in the Weddell sea during summer. *Deep Sea Res. Oceanogr. Abstr.* 21, 431–443. [https://doi.org/10.1016/0011-7471\(74\)90092-8](https://doi.org/10.1016/0011-7471(74)90092-8)
- Carvalho-Borges M de, Orselli IBM, Ferreira ML de C, Kerr R, (2018) Seawater acidification and anthropogenic carbon distribution on the continental shelf and slope of the western South Atlantic Ocean. *J. Mar. Syst.* 187, 62–81. <https://doi.org/10.1016/j.jmarsys.2018.06.008>
- Conrad CJ, Lovenduski NS, (2015) Climate-driven variability in the Southern Ocean carbonate system. *J. Clim.* 28, 5335–5350. <https://doi.org/10.1175/JCLI-D-14-00481.1>
- Cooley SR, Doney SC, Feely RA, Doney SC, Cooley SR, National Oceanic and Atmospheric Administration, (2013) Ocean acidification. U.S. Dep. Commer. 22, 36–47. <https://doi.org/10.1002/9780470057339.vnn124>

- Deacon G, (1937) The Hydrology of the Southern Ocean. London
- DeJong HB, Dunbar RB, Mucciarone D, Kowek DA, (2015) Carbonate saturation state of surface waters in the Ross Sea and Southern Ocean: controls and implications for the onset of aragonite undersaturation. *Biogeosciences* 12, 6881–6896. <https://doi.org/10.5194/bg-12-6881-2015>
- Dickson AG, (1990) Thermodynamics of the dissociation of boric acid in synthetic seawater from 273 . 15 to 318 . 15 K 37, 755–766
- Dickson AG, Afghan JD, Anderson GC, (2003) Reference materials for oceanic CO₂ analysis: a method for the certification of total alkalinity. *Mar. Chem.* 80, 185–197. [https://doi.org/10.1016/S0304-4203\(02\)00133-0](https://doi.org/10.1016/S0304-4203(02)00133-0)
- DOE, (1994) Handbook of methods for the analysis of the various parameters of the carbon dioxide system in sea water. Version 2, Department of Energy. Oak Ridge, TN. <https://doi.org/10.2172/10107773>
- Doney SC, Fabry VJ, Feely RA, Kleypas JA, (2009) Ocean Acidification: The Other CO₂ Problem. *Ann. Rev. Mar. Sci.* 1, 169–192. <https://doi.org/10.1146/annurev.marine.010908.163834>
- Dotto TS, Kerr R, Mata MM, Eiras Garcia CA, (2016) Multidecadal freshening and lightening in the deep waters of the Bransfield Strait, Antarctica. *J. Geophys. Res. Ocean.* 3741–3756. <https://doi.org/10.1002/2015JC011228>. Received
- Dziak RP, Park M, Lee WS, Matsumoto H, Bohnenstiel DR, Haxel JH, (2010) Tectonomagmatic activity and ice dynamics in the Bransfield Strait back-arc basin, Antarctica. *J. Geophys. Res.* 115, B01102. <https://doi.org/10.1029/2009JB006295>
- Fabry VJ, McClintock JB, Mathis JT, Grebmeier JM, (2009) Ocean Acidification at High Latitudes: The Bellwether. *Oceanography* 22, 160–171. <https://doi.org/10.5670/oceanog.2009.105>
- Fahrbach E, Rohardt G, Krause G, (1992) The Antarctic coastal current in the southeastern Weddell Sea. *Polar Biol.* 12, 171–182. <https://doi.org/10.1007/BF00238257>
- Fassbender AJ, Sabine CL, Palevsky HI, (2017) Nonuniform ocean acidification and attenuation of the ocean carbon sink. *Geophys. Res. Lett.* 44, 8404–8413. <https://doi.org/10.1002/2017GL074389>
- Fretzdorff S, (2004) Magmatism in the Bransfield Basin: Rifting of the South Shetland Arc? *J. Geophys. Res.* 109, B12208. <https://doi.org/10.1029/2004JB003046>
- Frölicher TL, Sarmiento JL, Paynter DJ, Dunne JP, Krasting JP, Winton M, (2015) Dominance of the Southern Ocean in Anthropogenic Carbon and Heat Uptake in CMIP5 Models. *J. Clim.* 28, 862–886. <https://doi.org/10.1175/JCLI-D-14-00117.1>
- Funaki M, Higashino S-I, Sakanaka S, Iwata N, Nakamura N, Hirasawa N, Obara N, Kuwabara M, (2014) Small unmanned aerial vehicles for aeromagnetic surveys and their flights in the South Shetland Islands, Antarctica. *Polar Sci.* 8, 342–356. <https://doi.org/10.1016/j.polar.2014.07.001>

- Galindo-Zaldívar J, Gamboa L, Maldonado A, Nakao S, Bochu Y, (2004) Tectonic development of the Bransfield Basin and its prolongation to the South Scotia Ridge, northern Antarctic Peninsula. *Mar. Geol.* 206, 267–282. <https://doi.org/10.1016/j.margeo.2004.02.007>
- García M, Ercilla G, Alonso B, (2009) Morphology and sedimentary systems in the Central Bransfield Basin, Antarctic Peninsula: sedimentary dynamics from shelf to basin. *Basin Res.* 21, 295–314. <https://doi.org/10.1111/j.1365-2117.2008.00386.x>
- Gieskes JM, (1969) Effect of temperature on the pH Seawater. *Limnol. Oceanogr.* 14, 679–685. <https://doi.org/10.4319/lo.1969.14.5.0679>
- Gonçalves-Araujo R, de Souza MS, Tavano VM, Eiras Garcia CA, (2015) Influence of oceanographic features on spatial and interannual variability of phytoplankton in the Bransfield Strait, Antarctica. *J. Mar. Syst.* 142, 1–15. <https://doi.org/10.1016/j.jmarsys.2014.09.007>
- Gordon AL, (1998) Western Weddell Sea thermohaline stratification, in: *Ocean, Ice, and Atmosphere: Interactions at the Antarctic Continental Margin.* pp. 215–240. <https://doi.org/10.1029/AR075p0215>
- Gordon AL, Mensch M, Zhaoqian D, Smethie WM, de Bettencourt J, (2000) Deep and bottom water of the Bransfield Strait eastern and central basins. *J. Geophys. Res. Ocean.* 105, 11337–11346. <https://doi.org/10.1029/2000JC900030>
- Gordon AL, Nowlin WD, (1978) The Basin Waters of the Bransfield Strait. *J. Phys. Oceanogr.* 8, 258–264. [https://doi.org/10.1175/1520-0485\(1978\)008<0258:TBWOTB>2.0.CO;2](https://doi.org/10.1175/1520-0485(1978)008<0258:TBWOTB>2.0.CO;2)
- Gordon AL, Visbeck M, Huber B, (2001) Export of Weddell Sea deep and bottom water. *J. Geophys. Res. Ocean.* 106, 9005–9017. <https://doi.org/10.1029/2000JC000281>
- Goyet C, Gonçalves Ito R, Touratier F, (2009) Anthropogenic carbon in the eastern South Pacific Ocean. *Biogeosciences* 6, 149–156. <https://doi.org/10.5194/bgd-4-1815-2007>
- Goyet C, Poisson A, (1989) New determination of carbonic acid dissociation constants in seawater as a function of temperature and salinity. *Deep. Res.* 30, 1635–1654
- Grad M, Shiobara H, Janik T, Guterch A, Shimamura H, (1997) Crustal model of the Bransfield Rift, West Antarctica, from detailed OBS refraction experiments. *Geophys. J. Int.* 130, 506–518
- Gregor L, Kok S, Monteiro PMS, (2018) Interannual drivers of the seasonal cycle of CO₂ in the Southern Ocean. *Biogeosciences* 15, 2361–2378. <https://doi.org/10.5194/bg-15-2361-2018>
- Guallart EF, Schuster U, Fajar NM, Legge OJ, Brown PJ, Pelejero C, Messias M-J, Calvo E, Watson AJ, Ríos AF, Pérez FF, (2015) Trends in anthropogenic CO₂ in water masses of the Subtropical North Atlantic Ocean. *Prog. Oceanogr.* 131, 21–32. <https://doi.org/10.1016/j.pocean.2014.11.006>

- Hancock AM, Davidson AT, McKinlay J, McMinn A, Schulz KG, van den Enden RL, (2018) Ocean acidification changes the structure of an Antarctic coastal protistan community. *Biogeosciences* 15, 2393–2410. <https://doi.org/10.5194/bg-15-2393-2018>
- Hassoun AER, Gemayel E, Krasakopoulou E, Goyet C, Abboud-Abi Saab M, Guglielmi V, Touratier F, Falco C, (2015) Acidification of the Mediterranean Sea from anthropogenic carbon penetration. *Deep Sea Res. Part I Oceanogr. Res. Pap.* 102, 1–15. <https://doi.org/10.1016/j.dsr.2015.04.005>
- Hauck J, Hoppema M, Bellerby RGJ, Völker C, Wolf-Gladrow D, (2010) Data-based estimation of anthropogenic carbon and acidification in the Weddell Sea on a decadal timescale. *J. Geophys. Res.* 115, C03004. <https://doi.org/10.1029/2009JC005479>
- Hauck J, Völker C, Wang T, Hoppema M, Losch M, Wolf-Gladrow DA, (2013) Seasonally different carbon flux changes in the Southern Ocean in response to the southern annular mode. *Global Biogeochem. Cycles* 27, 1236–1245. <https://doi.org/10.1002/2013GB004600>
- Hellmer HH, Kauker F, Timmermann R, Hattermann T, (2017) The Fate of the Southern Weddell Sea Continental Shelf in a Warming Climate. *J. Clim.* 30, 4337–4350. <https://doi.org/10.1175/JCLI-D-16-0420.1>
- Hofmann EE, Klinck JM, Lascara CM, Smith DA, (1996) Water mass distribution and circulation west of the Antarctic Peninsula and including Bransfield Strait. pp. 61–80. <https://doi.org/10.1029/AR070p0061>
- Humphreys MP, Daniels CJ, Wolf-Gladrow DA, Tyrrell T, Achterberg EP, (2018) On the influence of marine biogeochemical processes over CO₂ exchange between the atmosphere and ocean. *Mar. Chem.* 199, 1–11. <https://doi.org/10.1016/j.marchem.2017.12.006>
- Ingrosso G, Bensi M, Cardin V, Giani M, (2017) Anthropogenic CO₂ in a dense water formation area of the Mediterranean Sea. *Deep Sea Res. Part I Oceanogr. Res. Pap.* 123, 118–128. <https://doi.org/10.1016/j.dsr.2017.04.004>
- Ito T, Follows MJ, (2013) Air-sea disequilibrium of carbon dioxide enhances the biological carbon sequestration in the Southern Ocean. *Global Biogeochem. Cycles* 27, 1129–1138. <https://doi.org/10.1002/2013GB004682>
- Ito T, Woloszyn M, Mazloff M, (2010) Anthropogenic carbon dioxide transport in the Southern Ocean driven by Ekman flow. *Nature* 463, 80–83. <https://doi.org/10.1038/nature08687>
- Jones DC, Ito T, Takano Y, Hsu W-C, (2014) Spatial and seasonal variability of the air-sea equilibration timescale of carbon dioxide. *Global Biogeochem. Cycles* 28, 1163–1178. <https://doi.org/10.1002/2014GB004813>
- Kapsenberg L, Kelley AL, Shaw EC, Martz TR, Hofmann GE, (2015) Implications for the design of ocean acidification experiments 9638. <https://doi.org/10.1038/srep09638>

- Kerr R, Goyet C, da Cunha LC, Orselli IBM, Lencina-Avila JM, Borges Mendes CR, Carvalho-Borges M, Mata MM, Tavano VM, Eidt RT, (2017a) Carbonate system properties in the Gerlache Strait, Northern Antarctic Peninsula (February 2015): II. Anthropogenic CO₂ and seawater acidification. *Deep. Res. Part II Top. Stud. Oceanogr.* 149, 1–11. <https://doi.org/10.1016/j.dsr2.2017.07.007>
- Kerr R, Mata MM, Borges Mendes CR, Secchi ER, (2018) Northern Antarctic Peninsula: a marine climate hotspot of rapid changes on ecosystems and ocean dynamics. *Deep Sea Res. Part II Top. Stud. Oceanogr.* 149, 4–9. <https://doi.org/10.1016/j.dsr2.2018.05.006>
- Kerr R, Orselli IBM, Lencina-Avila JM, Eidt RT, Borges Mendes CR, da Cunha LC, Goyet C, Mata MM, Tavano VM, (2017b) Carbonate system properties in the Gerlache Strait, Northern Antarctic Peninsula (February 2015): I. Sea - Air CO₂ Fluxes. *Deep. Res. Part II Top. Stud. Oceanogr.* 1–11. <https://doi.org/10.1016/j.dsr2.2017.07.007>
- Krasakopoulou E, Souvermezoglou E, Goyet C, (2011) Anthropogenic CO₂ fluxes in the Otranto Strait (E. Mediterranean) in February 1995. *Deep Sea Res. Part I Oceanogr. Res. Pap.* 58, 1103–1114. <https://doi.org/10.1016/j.dsr.2011.08.008>
- Le Quéré C, Andrew RM, Friedlingstein P, Sitch S, Hauck J, Pongratz J, Pickers PA, Korsbakken JI, Peters GP, Canadell JG, Arneth A, Arora VK, Barbero L, Bastos A, Bopp L, Chevallier F, Chini LP, Ciais P, Doney SC, Gkritzalis T, Goll DS, Harris I, Haverd V, Hoffman FM, Hoppema M, Houghton RA, Hurt G, Illyina T, Jain AK, Johannessen T, Jones CD, Kato E, Keeling RF, Goldewijk KK, Landschützer P, Lefèvre N, Lienert S, Liu Z, Lombardozzi D, Metzl N, Munro DR, Nabel JEMS, Nakaoka S-I, Neill C, Olsen A, Ono T, Patra P, Peregon A, Peters W, Peylin P, Pfeil B, Pierrot D, Poulter B, Rehder G, Resplandy L, Robertson E, Rocher M, Rödenbeck C, Schuster U, Schwinger J, Séférian R, Skjelvan I, Steinhoff T, Sutton AJ, Tans PP, Tian H, Tilbrook B, Tubiello FN, van der Laan-Luijkx IT, van der Werf GR, Viovy N, Walker AP, Wiltshire AJ, Wright R, Zaehle S, Zheng B, (2018) Global Carbon Budget 2018. *Earth Syst. Sci. Data* 10, 2141–2194. <https://doi.org/10.5194/essd-10-2141-2018>
- Le Quéré C, Andrew RM, Friedlingstein P, Sitch S, Pongratz J, Manning AC, Korsbakken JI, Peters GP, Canadell JG, Jackson RB, Boden TA, Tans PP, Andrews OD, Arora VK, Bakker DCE, Barbero L, Becker M, Betts RA, Bopp L, Chevallier F, Chini LP, Ciais P, Cosca C, Cross J, Currie KI, Gasser T, Harris I, Hauck J, Haverd V, Houghton RA, Hunt CW, Hurt G, Illyina T, Jain AK, Kato E, Kautz M, Keeling RF, Klein Goldewijk K, Körtzinger A, Landschützer P, Lefèvre N, Lenton A, Lienert S, Lima ID, Lombardozzi D, Metzl N, Millero FJ, Monteiro PMS, Munro DR, Nabel JEMS, Nakaoka S-I, Nojiri Y, Padín XA, Peregon A, Pfeil B, Pierrot D, Poulter B, Rehder G, Reimer JJ, Rödenbeck C, Schwinger J, Séférian R, Skjelvan I, Stocker BD, Tian H, Tilbrook B, van der Laan-Luijkx IT, van der Werf GR, van Heuven SMAC, Viovy N, Vuichard N, Walker AP, Watson AJ, Wiltshire AJ, Zaehle S, Zhu D, (2017) Global carbon budget 2017. *Earth Syst. Sci. Data*. <https://doi.org/https://doi.org/10.5194/essd-2017-123>

- Lee K, Choi S-D, Park G-H, Wanninkhof R, Peng T-H, Key RM, Sabine CL, Feely RA, Bullister JL, Millero FJ, Kozyr A, (2003) An updated anthropogenic CO₂ inventory in the Atlantic Ocean. *Global Biogeochem. Cycles* 17, n/a-n/a. <https://doi.org/10.1029/2003GB002067>
- Legge OJ, Bakker DCE, Meredith MP, Venables HJ, Brown PJ, Jones EM, Johnson MT, (2017) The seasonal cycle of carbonate system processes in Ryder Bay, West Antarctic Peninsula. *Deep Sea Res. Part II Top. Stud. Oceanogr.* 139, 167–180. <https://doi.org/10.1016/j.dsr2.2016.11.006>
- Lencina-Avila JM, Goyet C, Kerr R, Orselli IBM, Mata MM, Touratier F, (2018) Past and future evolution of the carbonate system in a coastal zone of the Northern Antarctic Peninsula. *Deep Sea Res. Part II Top. Stud. Oceanogr.* 149, 193–205. <https://doi.org/10.1016/j.dsr2.2017.10.018>
- Lenton A, Matear RJ, (2007) Role of the Southern Annular Mode (SAM) in Southern Ocean CO₂ uptake. *Global Biogeochem. Cycles* 21, n/a-n/a. <https://doi.org/10.1029/2006GB002714>
- Lewis E, Wallace DWR, (1998) Program developed for CO₂ system calculations. *Ornl/Cdiac-105*. <https://doi.org/4735>
- Lo Monaco C, (2005) Anthropogenic CO₂ in the Southern Ocean: Distribution and inventory at the Indian-Atlantic boundary (World Ocean Circulation Experiment line I6). *J. Geophys. Res.* 110, C06010. <https://doi.org/10.1029/2004JC002643>
- López-Martínez J, Schmid T, Serrano E, Mink S, Nieto A, Guillaso S, (2016) Geomorphology and landforms distribution in selected ice-free areas in the South Shetland Islands, Antarctic Northern Peninsula region. *Cuad. Investig. Geográfica* 42, 435. <https://doi.org/10.18172/cig.2965>
- Lovenduski NS, Gruber N, Doney SC, Lima ID, (2007) Enhanced CO₂ outgassing in the Southern Ocean from a positive phase of the Southern Annular Mode. *Global Biogeochem. Cycles* 21, n/a-n/a. <https://doi.org/10.1029/2006GB002900>
- Lovenduski NS, Yeager SG, Lindsay K, Long MC, (2018) Predicting near-term changes in ocean carbon uptake. *Earth Syst. Dyn. Discuss.* 1–25. <https://doi.org/10.5194/esd-2018-73>
- Manno C, Bednaršek N, Tarling GA, Peck VL, Comeau S, Adhikari D, Bakker DCE, Bauerfeind E, Bergan AJ, Berning MI, Buitenhuis E, Burridge AK, Chierici M, Flöter S, Fransson A, Gardner J, Howes EL, Keul N, Kimoto K, Kohnert P, Lawson GL, Lischka S, Maas A, Mekkes L, Oakes RL, Pebody C, Peijnenburg KTCA, Seifert M, Skinner J, Thibodeau PS, Wall-Palmer D, Ziveri P, (2017) Shelled pteropods in peril: Assessing vulnerability in a high CO₂ ocean. *Earth-Science Rev.* 169, 132–145. <https://doi.org/10.1016/j.earscirev.2017.04.005>
- Mata MM, Tavano VM, Eiras Garcia CA, 2018 15 years sailing with the Brazilian High Latitude Oceanography Group (GOAL). *Deep Sea Res. Part II Top. Stud. Oceanogr.* 149, 1–3. <https://doi.org/10.1016/j.dsr2.2018.05.007>
- Matear RJ, Lenton A, (2008) Impact of Historical Climate Change on the Southern Ocean Carbon Cycle. *J. Clim.* 21, 5820–5834. <https://doi.org/10.1175/2008JCLI2194.1>

- Mattsdotter Björk M, Fransson A, Torstensson A, Chierici M, (2014) Ocean acidification state in western Antarctic surface waters: controls and interannual variability. *Biogeosciences* 11, 57–73.
<https://doi.org/10.5194/bg-11-57-2014>
- McNeil BI, Tilbrook B, Matear RJ, (2001) Accumulation and uptake of anthropogenic CO₂ in the Southern Ocean, south of Australia between 1968 and 1996. *J. Geophys. Res. Ocean.* 106, 31431–31445.
<https://doi.org/10.1029/2000JC000331>
- Mensch M, Simon A, Bayer R, (1998) Tritium and CFC input functions for the Weddell Sea. *J. Geophys. Res. Ocean.* 103, 15923–15937.
<https://doi.org/10.1029/98JC00145>
- Millero FJ, (2007) The Marine Inorganic Carbon Cycle. *Chem. Rev.* 107, 308–341. <https://doi.org/10.1021/cr0503557>
- Moreau S, Penna A Della, Llort J, Patel R, Langlais C, Boyd PW, Matear RJ, Phillips HE, Trull TW, Tilbrook B, Lenton A, Strutton PG, (2017) Eddy-induced carbon transport across the Antarctic Circumpolar Current. *Global Biogeochem. Cycles* 31, 1368–1386.
<https://doi.org/10.1002/2017GB005669>
- Murata A, Kumamoto Y, Sasaki K, (2019) Decadal-Scale Increases of Anthropogenic CO₂ in Antarctic Bottom Water in the Indian and Western Pacific Sectors of the Southern Ocean. *Geophys. Res. Lett.* 46, 833–841.
<https://doi.org/10.1029/2018GL080604>
- Naveira Garabato AC, Zika JD, Jullion L, Brown PJ, Holland PR, Meredith MP, Bacon S, (2016) The thermodynamic balance of the Weddell Gyre. *Geophys. Res. Lett.* 43, 317–325. <https://doi.org/10.1002/2015GL066658>
- Nelsen MP, DiMichele WA, Peters SE, Boyce CK, (2016) Delayed fungal evolution did not cause the Paleozoic peak in coal production. *Proc. Natl. Acad. Sci.* 113, 2442–2447. <https://doi.org/10.1073/pnas.1517943113>
- Nicholls KW, Østerhus S, Makinson K, Gammelsrød T, Fahrbach E, (2009) Ice-ocean processes over the continental shelf of the southern Weddell Sea, Antarctica: A review. *Rev. Geophys.* 47, RG3003.
<https://doi.org/10.1029/2007RG000250>
- Orr JC, Fabry VJ, Aumont O, Bopp L, Doney SC, Feely RA, Gnanadesikan A, Gruber N, Ishida A, Joos F, Key RM, Lindsay K, Maier-Reimer E, Matear RJ, Monfray P, Mouchet A, Najjar RG, Plattner G-K, Rodgers KB, Sabine CL, Sarmiento JL, Schlitzer R, Slater RD, Totterdell IJ, Weirig M-F, Yamanaka Y, Yool A, (2005) Anthropogenic ocean acidification over the twenty-first century and its impact on calcifying organisms. *Nature* 437, 681–686. <https://doi.org/10.1038/nature04095>
- Orselli IBM, Goyet C, Kerr R, Azevedo JLL de, Araujo M, Galdino F, Touratier F, Garcia CAE, (2019) The Effect of Agulhas Eddies on Absorption and Transport of Anthropogenic Carbon in the South Atlantic Ocean. *Climate* 7, 84. <https://doi.org/10.3390/cli7060084>
- Orselli IBM, Kerr R, Ito RG, Tavano VM, Borges Mendes CR, Garcia CAE, (2018) How fast is the Patagonian shelf-break acidifying? *J. Mar. Syst.* 178, 1–14. <https://doi.org/10.1016/j.jmarsys.2017.10.007>

- Pardo PC, Pérez FF, Khatiwala S, Ríos AF, (2014) Anthropogenic CO₂ estimates in the Southern Ocean: Storage partitioning in the different water masses. *Prog. Oceanogr.* 120, 230–242.
<https://doi.org/10.1016/j.pocean.2013.09.005>
- Pardo PC, Tilbrook B, Langlais C, Trull TW, Rintoul SR, (2017) Carbon uptake and biogeochemical change in the Southern Ocean, south of Tasmania. *Biogeosciences Discuss.* 1–43. <https://doi.org/10.5194/bg-2017-213>
- Pelejero C, Calvo E, Hoegh-Guldberg O, (2010) Paleo-perspectives on ocean acidification. *Trends Ecol. Evol.* 25, 332–344.
<https://doi.org/10.1016/j.tree.2010.02.002>
- Redfield AC, Ketchum BH, Richards FA, (1963) The Influence of Organisms on the Composition of Sea Water. *sea ideas Obs. Prog. study seas*
- Renner AHH, Heywood KJ, Thorpe SE, (2009) Validation of three global ocean models in the Weddell Sea. *Ocean Model.* 30, 1–15.
<https://doi.org/10.1016/j.ocemod.2009.05.007>
- Ridgwell A, Zeebe RE, (2005) The role of the global carbonate cycle in the regulation and evolution of the Earth system. *Earth Planet. Sci. Lett.*
<https://doi.org/10.1016/j.epsl.2005.03.006>
- Robertson R, Visbeck M, Gordon AL, Fahrbach E, (2002) Long-term temperature trends in the deep waters of the Weddell Sea. *Deep Sea Res. Part II Top. Stud. Oceanogr.* 49, 4791–4806.
[https://doi.org/10.1016/S0967-0645\(02\)00159-5](https://doi.org/10.1016/S0967-0645(02)00159-5)
- Ruiz Barlett EM, Tosonotto G V., Piola AR, Sierra ME, Mata MM, (2018) On the temporal variability of intermediate and deep waters in the Western Basin of the Bransfield Strait. *Deep Sea Res. Part II Top. Stud. Oceanogr.* 149, 31–46. <https://doi.org/10.1016/j.dsr2.2017.12.010>
- Sabine CL, (2004) The Oceanic Sink for Anthropogenic CO₂. *Science* (80-.). 305, 367–371. <https://doi.org/10.1126/science.1097403>
- Sandrini S, Ait-Ameur N, Rivaro P, Massolo S, Touratier F, Tositti L, Goyet C, (2007) Anthropogenic carbon distribution in the Ross Sea, Antarctica. *Antarct. Sci.* 19, 395. <https://doi.org/10.1017/S0954102007000405>
- Sangrà P, Gordo C, Hernández-Arencibia M, Marrero-Díaz Á, Rodríguez-Santana A, Stegner A, Martínez-Marrero A, Pelegrí JL, Pichon T, (2011) The Bransfield current system. *Deep Sea Res. Part I Oceanogr. Res. Pap.* 58, 390–402. <https://doi.org/10.1016/j.dsr.2011.01.011>
- Sangrà P, Stegner A, Hernández-Arencibia M, Marrero-Díaz Á, Salinas C, Aguiar-González B, Henríquez-Pastene C, Mouríño-Carballido B, (2017) The Bransfield Gravity Current. *Deep Sea Res. Part I Oceanogr. Res. Pap.* 119, 1–15. <https://doi.org/10.1016/j.dsr.2016.11.003>
- Schlosser P, Bullister JL, Bayer R, (1991) Studies of deep water formation and circulation in the Weddell Sea using natural and anthropogenic tracers. *Mar. Chem.* [https://doi.org/10.1016/S0304-4203\(09\)90011-1](https://doi.org/10.1016/S0304-4203(09)90011-1)
- Shadwick E, Trull TW, Thomas H, Gibson JAE, (2013) Vulnerability of Polar Oceans to Anthropogenic Acidification: Comparison of Arctic and Antarctic Seasonal Cycles. *Sci. Rep.* 3, 2339. <https://doi.org/10.1038/srep02339>

- Takahashi T, Sutherland SC, Sweeney C, Poisson A, Metzl N, Tilbrook B, Bates N, Wanninkhof R, Feely RA, Sabine CL, Olafsson J, Nojiri Y, (2002) Global sea-air CO₂ flux based on climatological surface ocean pCO₂, and seasonal biological and temperature effects. Deep Sea Res. Part II Top. Stud. Oceanogr. 49, 1601–1622. [https://doi.org/10.1016/S0967-0645\(02\)00003-6](https://doi.org/10.1016/S0967-0645(02)00003-6)
- Tanhua T, Hoppema M, Jones EM, Stöven T, Hauck J, Dávila MG, Santana-Casiano JM, Álvarez M, Strass VH, (2017) Temporal changes in ventilation and the carbonate system in the Atlantic sector of the Southern Ocean. Deep Sea Res. Part II Top. Stud. Oceanogr. 138, 26–38. <https://doi.org/10.1016/j.dsr2.2016.10.004>
- Thompson AF, Heywood KJ, (2008) Frontal structure and transport in the northwestern Weddell Sea. Deep Sea Res. Part I Oceanogr. Res. Pap. 55, 1229–1251. <https://doi.org/10.1016/j.dsr.2008.06.001>
- Thompson AF, Heywood KJ, Thorpe SE, Renner AHH, Trasviña A, (2009) Surface Circulation at the Tip of the Antarctic Peninsula from Drifters. J. Phys. Oceanogr. 39, 3–26. <https://doi.org/10.1175/2008JPO3995.1>
- Touratier F, Azouzi L, Goyet C, (2007) CFC-11, ¹⁴C and ³H tracers as a means to assess anthropogenic CO₂ concentrations in the ocean. Tellus B 59, 318–325. <https://doi.org/10.1111/j.1600-0889.2006.00247.x>
- Touratier F, Goyet C, (2011) Impact of the Eastern Mediterranean Transient on the distribution of anthropogenic CO₂ and first estimate of acidification for the Mediterranean Sea. Deep Sea Res. Part I Oceanogr. Res. Pap. 58, 1–15. <https://doi.org/10.1016/j.dsr.2010.10.002>
- Touratier F, Goyet C, (2004a) Definition, properties, and Atlantic Ocean distribution of the new tracer TrOCA. J. Mar. Syst. 46, 169–179. <https://doi.org/10.1016/j.jmarsys.2003.11.016>
- Touratier F, Goyet C, (2004b) Applying the new TrOCA approach to assess the distribution of anthropogenic CO₂ in the Atlantic Ocean. J. Mar. Syst. 46, 181–197. <https://doi.org/10.1016/j.jmarsys.2003.11.020>
- Touratier F, Goyet C, Coatanoan C, Andrié C, (2005) Assessments of anthropogenic CO₂ distribution in the tropical Atlantic Ocean. Deep Sea Res. Part I Oceanogr. Res. Pap. 52, 2275–2284. <https://doi.org/10.1016/j.dsr.2005.09.001>
- Touratier F, Goyet C, Houpert L, de Madron XD, Lefèvre D, Stabholz M, Guglielmi V, (2016) Role of deep convection on anthropogenic CO₂ sequestration in the Gulf of Lions (northwestern Mediterranean Sea). Deep Sea Res. Part I Oceanogr. Res. Pap. 113, 33–48. <https://doi.org/10.1016/j.dsr.2016.04.003>
- Uppström LR, (1974) The boron/chlorinity ratio of deep-sea water from the Pacific Ocean. Deep Sea Res. Oceanogr. Abstr. 21, 161–162. [https://doi.org/10.1016/0011-7471\(74\)90074-6](https://doi.org/10.1016/0011-7471(74)90074-6)
- van Caspel M, Hellmer HH, Mata MM, (2018) On the ventilation of Bransfield Strait deep basins. Deep Sea Res. Part II Top. Stud. Oceanogr. 149, 25–30. <https://doi.org/10.1016/j.dsr2.2017.09.006>

- van Caspel M, Schröder M, Huhn O, Hellmer HH, (2015) Precursors of Antarctic Bottom Water formed on the continental shelf off Larsen Ice Shelf. Deep. Res. Part I Oceanogr. Res. Pap. 99, 1–9.
<https://doi.org/10.1016/j.dsr.2015.01.004>
- van Heuven SMAC, Hoppema M, Jones EM, de Baar HJW, (2014) Rapid invasion of anthropogenic CO₂ into the deep circulation of the Weddell Gyre. Philos. Trans. R. Soc. A Math. Phys. Eng. Sci. 372, 20130056–20130056. <https://doi.org/10.1098/rsta.2013.0056>
- Wagener T, Metzl N, Caffin M, Fin J, Helias Nunige S, Lefèvre D, Lo Monaco C, Rougier G, Moutin T, (2018) Carbonate system distribution, anthropogenic carbon and acidification in the Western Tropical South Pacific (OUTPACE 2015 transect). Biogeosciences Discuss. 1–28. <https://doi.org/10.5194/bg-2018-163>
- Waugh DW, (2014) Changes in the ventilation of the southern oceans. Philos. Trans. R. Soc. A. <https://doi.org/http://dx.doi.org/10.1098/rsta.2013.0269>
- Wilson C, Klinkhammer GP, Chin CS, (1999) Hydrography within the Central and East Basins of the Bransfield Strait, Antarctica. J. Phys. Oceanogr. 29, 465–479. [https://doi.org/10.1175/1520-0485\(1999\)029<0465:HWTCAE>2.0.CO;2](https://doi.org/10.1175/1520-0485(1999)029<0465:HWTCAE>2.0.CO;2)